

國立交通大學

光電工程研究所

博士論文

有機與氧化物薄膜電晶體於前瞻顯示器應用之研究

The Study of Organic and Metal-oxide Thin-film Transistors for
Novel Display Applications

研究生：莊喬舜

指導教授：謝漢萍 博士

陳方中 博士

中華民國九十八年一月

有機與氧化物薄膜電晶體於
前瞻顯示器應用之研究

The Study of Organic and Metal-oxide Thin-film Transistors for
Novel Display Applications

研究生：莊喬舜 Student : Chiao-Shun Chuang

指導教授：謝漢萍 Advisor : Han-Ping D. Shieh

陳方中 Fung-Chung Chen

國立交通大學

光電工程研究所

博士論文

A Dissertation

Submitted to Institute of Electro-Optical Engineering

College of Electrical and Computer Engineering

National Chiao Tung University

in partial Fulfillment of the Requirements

for the Degree of

Doctor of Philosophy

in

Electro-Optical Engineering

2009

Hsinchu, Taiwan, Republic of China

中華民國九十八年一月

有機與氧化物薄膜電晶體於前瞻顯示器 應用之研究

博士研究生：莊喬舜

指導教授：謝漢萍、陳方中 博士

國立交通大學 光電工程研究所

摘 要

本論文研究有機與氧化物薄膜電晶體。論文前半部是研究以有機半導體五環素(pentacene)為主動層的薄膜電晶體。傳統有機薄膜電晶體 (OTFTs) 存在許多缺點，如過高的操作電壓，對光敏感及可靠度不佳等等因素。本研究提出使用高介電常數有機無機複合介電層來降低因載子遷移率過低造成的高操作電壓，並利用有機無機複合介電層中的奈米粉體做為電子電洞復合中心降低有機薄膜電晶體的光敏感度。此外，本研究率先使用一些功能性的有機介電層製作出含有彩色濾光片功能的薄膜電晶體，此研究展示了有機電子的多種功能性。後半段是研究非晶銦鎵錫氧化物(amorphous In-Ga-Zn-O)薄膜電晶體 (a-IGZO TFTs)。a-IGZO 的載子遷移率快(約 $10\sim 60\text{ cm}^2/\text{Vs}$)，為一種可能取代非晶矽薄膜電晶體的新材料。本研究先對 a-IGZO 的材料特性如光學特性、導電度跟溫度的關係做探討，之後對 a-IGZO TFT 在不同波長光的照射下的電性表現做深入的研究，並在最後提出一個具有物理含意的電性參數模型，作為日後發展可透視性電路或高速電路應用的基礎。最後並成功結合 pentacene/a-IGZO 兩種半導體材料製作成雙極性薄膜電晶體(ambipolar TFTs)，製作成 CMOS-like inverter circuit 可應用並簡化顯示器上之驅動電路。

The Study of Organic and Metal-oxide Thin-film Transistors for Novel Display Applications

Doctoral Student: Chiao-Shun Chuang

Advisor: Dr. Han-Ping David Shieh and Dr. Fang-Chun Chen

**Institute of Electro-Optical Engineering
National Chiao Tung University**

Abstract

This dissertation is divided into two parts. In the first part, it focuses on the pentacene-based organic thin-film transistors (OTFTs). There are many issues of traditional OTFTs, such as high operating voltage, photosensitivity, and poor reliability. We proposed that using high organic-inorganic nanocomposite dielectric as gate insulator to reduce the operating voltage caused from low material mobility. Furthermore, we used nanoparticles of composite dielectric as recombination centers to reduce photosensitivity of pentacene-based OTFTs. In addition, we also integrated color filter into TFT array. This study demonstrated one potential example for multifunctional organic electronics.

The second part discusses the properties of amorphous In-Ga-Zn-O thin-film transistors (a-IGZO TFTs). We first studied the optical, thermal, and electrical properties of a-IGZO film. Next, the electrical properties under different wavelength illumination of a-IGZO TFTs were studied. Furthermore, the a-IGZO density of states, simulation and modeling were investigated for the visible and high-speed electronics applications. Finally, we successfully combined pentacene and a-IGZO as active layer to make ambipolar TFTs. These devices show both p-type and n-type characteristic. CMOS-like inverter circuit was made to demonstrate the possibility for display applications.

Acknowledgement

回首過去兩千個日子，在這謝幕的時刻，經歷過的喜怒哀樂都一一的浮現眼前。很欣喜當初做了這個決定，選擇了交通大學。

首先感謝謝漢萍老師及陳方中老師，給予我多方面的支持、鼓勵、包容及細心指導，讓我順利完成最重要的求學階段。也特別感謝口試委員們的許多寶貴建議，其實我很想跟你們聊久一點...。

最特別的經驗是在密西根的半年時光。感謝 Jerzy Kanicki 教授給予我盡情揮灑的空間，子青同學和實驗室伙伴在生活及研究上的幫助，讓我明白其實我對真理的探討也是有極高度的興趣。



實驗室的伙伴，實在是超捨不得你們。乙白老師、均合、裕國、芳正、柏儒、注宏、奕智及榮安，感謝你們一路相挺。碩班眾多帥哥美女們，你們可是生活樂趣的重要來源。許許多多曾經伸手援助的貴人，在這一併感謝。

我辦到了，媽媽、哥哥！！ 謝謝你們的耐心及支持，這份榮耀與喜悅是屬於你們的。

Table of Contents

摘 要	I
ABSTRACT.....	II
ACKNOWLEDGEMENT.....	III
TABLE OF CONTENTS.....	IV
FIGURE CAPTIONS	VII
LIST OF TABLES.....	XII
CHAPTER 1 INTRODUCTION.....	1
1.1 ACTIVE MATRIX FLAT PANEL ELECTRONICS.....	1
1.2 FUTURE DISPLAYS	3
1.3 THIN-FILM TRANSISTORS AND OPERATION	5
1.4 ORGANIC THIN-FILM TRANSISTORS.....	7
1.4.1 Introduction to organic semiconductor and pentacene	7
1.4.2 Issues of organic thin-film transistors	13
1.4.3 Organic TFT state-of-arts	16
1.5 AMORPHOUS IN-GA-ZN-O THIN-FILM TRANSISTORS	17
1.5.1 Introduction to metal-oxide semiconductor	17
1.5.2 a-IGZO TFT state-of-arts.....	20
1.6 AMBIPOLAR TFTs	23
1.7 CMOS INVERTER	25
1.8 MOTIVATION.....	26
1.9 ORGANIZATION OF DISSERTATION	27
CHAPTER 2 EXPERIMENTAL METHODS	29
2.1 OTFT DEVICE FABRICATION	29
2.2 ELECTRICAL MEASUREMENT OF DEVICES.....	32
2.3 SURFACE MORPHOLOGY MEASUREMENT	33
2.4 CONTACT ANGLE MEASUREMENT	34
2.5 SPUTTERING.....	35
CHAPTER 3 ORGANIC TFTS WITH POLYMERIC NANOCOMPOSITE DIELECTRICS.....	38

3.1 INTRODUCTION.....	38
3.2 EXPERIMENT	39
3.3 RESULT AND DISCUSSION	41
3.4 CONCLUSION.....	48
CHAPTER 4 ORGANIC TFTS WITH REDUCED PHOTSENSITIVITY ..	50
4.1 PART. A ORGANIC THIN-FILM TRANSISTORS WITH REDUCED PHOTSENSITIVITY .	50
4.1.1 Introduction.....	50
4.1.2 Experiment	52
4.1.3 Result and Discussion	52
4.1.4 Conclusion	61
4.2 PART. B PHOTOCURRENT SUPPRESSION OF TRANSPARENT ORGANIC THIN-FILM TRANSISTORS	62
4.2.1 Introduction.....	62
4.2.2 Experiment	63
4.2.3 Result and Discussion	65
4.2.4 Conclusion	71
CHAPTER 5 COLOR FILTERING FUNCTIONAL OTFTS.....	72
5.1 PART. A ORGANIC THIN-FILM TRANSISTORS WITH COLOR FILTERING FUNCTIONAL GATE INSULATORS	72
5.1.1 Introduction.....	72
5.1.2 Experiment	73
5.1.3 Result and discussion.....	75
5.1.4 Conclusion	79
5.2 PART. B ORGANIC THIN-FILM TRANSISTOR WITH COLORFUL PMMA GATE DIELECTRICS	80
CHAPTER 6 PHOTSENSITIVITY OF AMORPHOUS IGZO TFTS.....	86
6.1 INTRODUCTION.....	86
6.2 EXPERIMENT	87
6.3 RESULT	89
6.4 DISCUSSION	96
6.5 CONCLUSION.....	99
CHAPTER 7 2-D NUMERICAL SIMULATION OF RF SPUTTER AMORPHOUS IGZO TFTS.....	101
7.1 INTRODUCTION.....	101
7.2 SIMULATION.....	102
7.3 RESULT AND DISCUSSION	107

7.4 CONCLUSION.....	109
CHAPTER 8 AMBIPOLAR TFTS AND CMOS-LIKE INVERTER	110
8.1 INTRODUCTION.....	110
8.2 LATEST RESULTS.....	110
CHAPTER 9 CONCLUSION AND FUTURE WORK.....	115
9.1 CONCLUSION.....	115
9.1.1 <i>Organic Thin-film transistors with polymeric nanocomposite dielectrics</i>	116
9.1.2 <i>Organic thin-film transistors with reduced photosensitivity.....</i>	117
9.1.3 <i>Color filtering functional organic thin-film transistors.....</i>	118
9.1.4 <i>Photosensitivity of amorphous In-Ga-Zn-O thin-film transistors.....</i>	119
9.1.5 <i>2-D Numerical simulation of RF sputter a-InGaZnO TFTs.....</i>	120
9.1.6 <i>Ambipolar TFTs and CMOS-like inverter.....</i>	121
9.2 FUTURE WORK.....	122
9.2.1 <i>Pentacene based OTFTs.....</i>	122
9.2.1 <i>a-IGZO TFTs.....</i>	123
REFERENCES.....	125
PUBLICATION LIST	132
VITA.....	134



Figure Captions

Fig. 1-1 AMLCD applications	2
Fig. 1-2 Prototypes of AMOLED.....	3
Fig. 1-3 Future displays	4
Fig. 1-4 TFT requirements for future large scale displays (Samsung SID08).....	4
Fig. 1-5 A bottom-gate TFT structure and several energy band diagrams. (a) TFT structure. Energy band diagram when (b) biased in equilibrium. When (c) a negative voltage and (d) a positive voltage is applied to the gate.	7
Fig. 1-6 Applications of organic transistors.....	8
Fig. 1-7 Doping mechanisms and related applications.	9
Fig. 1-8 Pentacene molecule structure.....	13
Fig. 1-9 Typical operating range of OTFT.....	13
Fig. 1-10 Transfer characteristics under illumination for an OTFT.....	14
Fig. 1-11 (a) Cross-sectional view of a conventional OTFT. (b) Transfer curves of non-modified, HMDS treated, and PaMS treated pentacene TFTs. (c) Normalized output current under bias stress of these devices.	15
Fig. 1-12 Flexible AMOLED driven by OTFTs and specification.	16
Fig. 1-13 Schematic orbital drawing of electron pathway (conduction band bottom) in conventional silicon-base semiconductor and ionic oxide semiconductors.	17
Fig. 1-14 The amorphous formation region (right) and the electron mobilities and concentrations evaluated from the Hall effects for the amorphous thin films (left) in the $\text{In}_2\text{O}_3\text{-Ga}_2\text{O}_3\text{-ZnO}$ system. The thin films were deposited on a glass substrate by pulsed laser deposition under deposition atmosphere of $\text{PO}_2 = 1 \text{ Pa}$. Number in the parenthesis denotes carrier electron concentration ($\times 10^{18} \text{ cm}^{-3}$). [12].....	19
Fig. 1-15 The carrier concentration as a function of O_2 pressure during the deposition in a-InGaZnO_3 and $\text{a-In}_2\text{Zn}_3\text{O}_6$. [12]	19
Fig. 1-16 The cross sectional view of Samsung's a-IGZO TFT. [13].....	20
Fig. 1-17 The representative transfer curves of the a-IGZO TFTs with $W/L=25/10\mu\text{m}$ with ESL. The S value and V_{TH} were very sensitively affected by the material of ESL. [13].....	21
Fig. 1-18 The display image of Samsung's 12.1" WXGA AMOLED display	23
Fig. 1-19 (a) Illustration of the source, drain, and gate potentials with respect to each other in a field-effect transistor. (b) Channel potential in the ambipolar regime with two separate channels of holes and electrons that meet within the transistor	

channel, where opposite charge carriers recombine (inset). (c) Transfer characteristics for an ambipolar transistor (d) Output characteristics for the same transistor for positive (first quadrant) and for negative (third quadrant) V_{GS} and V_{DS} , respectively.	24
Fig. 1-20 (a) CMOS inverter circuit (b) standard symbol (c) output/input voltage diagram	26
Fig. 1-21 Organic TFTs, amorphous oxide TFTs, and ambipolar TFTs of this study for future display backplane.....	27
Fig. 2-1 Schematic structure of ITO-patterned-glass.....	29
Fig. 2-2 Schematic picture of (a) step 4 and (b) step 5	30
Fig. 2-3 The flow chart of typical OTFT device fabrication	32
Fig. 2-4 A schematic model of atomic force microscope.....	33
Fig. 2-5 The contact angle formation of liquid on solid surface.....	34
Fig. 2-6 Schematic sputtering system in NCTU	37
Fig. 3-1 Chemical structures of the pentacene and cross-linked PVP; device structure of the OTFT	40
Fig. 3-2 Calculated and experimental dielectric constants	42
Fig. 3-3 The output characteristics of OTFTs with (a) a neat PVP insulator (b) a composite insulator with 15 wt% TiO_2	43
Fig. 3-4 The transfer characteristic at constant $V_{DS} = -30V$ for OTFTs with 1wt%, 15wt% of TiO_2 nanocomposite insulators, and nanocomposite insulator with $P\alpha MS$ interfacial layer.....	45
Fig. 3-5 AFM height-mode images of pentacene deposited on the surface of (a) neat cross-linked PVP; (b) cross-linked PVP blended with 15 wt% TiO_2 nanoparticles; (c) cross-linked PVP blended with 15 wt% TiO_2 nanoparticles and further modification with $P\alpha MS$ interfacial layer.	46
Fig. 3-6 The transfer characteristics of the OTFT with a thinner gate insulator. The inset shows the corresponding output characteristic from $V_{GS} = 0 V$ to $-10 V$..	47
Fig. 3-7 (a) Device structure and bending view of flexible OTFTs. (b) Output characteristics ($I_{DS}-V_{DS}$) of the flexible OTFT.	49
Fig. 4-1 (a) The device structure of the OTFTs in this study. (b)Energy band diagram of pentacene and TiO_2	51
Fig. 4-2 (a) Water contact angle of PVP; (b) $P\alpha MS$	54
Fig. 4-3 Transfer curves for devices in the dark and under illumination (10mW) with (a) cross-linked PVP and cross-linked PVP/ $P\alpha MS$ double layers as the dielectric insulators and (b) PVP + 15 wt% TiO_2 as the gate insulator.....	55
Fig. 4-4 AFM images of pentacene on (a) cross-linked PVP, (b) $P\alpha MS$ /cross-linked PVP and (c) $P\alpha MS/TiO_2$ nanoparticles + cross-linked PVP	57

Fig. 4-5 The x-ray diffraction pattern of pentacene deposited on Si/SiO ₂ substrates modified with (a)PαMS; (b)cross-linked PVP; (c) cross-linked PVP blended with 15 wt% TiO ₂ nanoparticles and further modification with PαMS. The peaks marked with asterisks are due to the structure of TiO ₂ nanoparticles.....	57
Fig. 4-6 Transfer characteristics of the device with n-doped Si/SiO ₂ as the substrate in the dark and under illumination (10mW). The inset shows the device structure.	58
Fig. 4-7 The normalized time-dependent current of the devices (a) in the dark; and (b) under illumination (10mW). The devices with PVP and PVP/PαMS as the dielectric layers were biased at V _{GS} = -10 V and V _{DS} = -10 V; while the device with 15 wt% TiO ₂ nanoparticles was measured at V _{GS} = -5 V and V _{DS} = -4 V. .	60
Fig. 4-8 (a) Chemical structures of the organic semiconductor, pentacene, and the polymer gate insulators, cross-linked PVP and PMMA. (b) The device structure of the OTFTs in this study.....	63
Fig. 4-9 Absorption coefficient of pentacene.....	64
Fig. 4-10 The transfer characteristics of the OTFTs in the dark and under the illumination (10mW) with (a) neat cross-linked PVP as the gate dielectric layer; (b) cross-linked PVP/PαMS bilayer insulator blended with 1 wt% TiO ₂ nanoparticles as the gate dielectric. ITO modified with MoO ₂ (20 nm) was used as the source and drain electrode materials for both devices.....	66
Fig. 4-11 Energy band diagram of pentacene and PVP/TiO ₂ , and the proposed mechanism with recombination centers.....	67
Fig. 4-12 The transfer curves for devices in the dark and under the light illumination (10mW) with (a) neat PMMA as the gate insulator; (b) PMMA blended with 1wt% TiO ₂ as the gate insulator.	68
Fig. 4-13 Transmittance spectra of various OTFT layers.	70
Fig. 5-1 (a) The cross sectional illustration of the OTFT with a bi-layer colored dielectric insulator consisting of a commercial color filter and PTFMA. (b) Chemical structure of polymethylmethacrylate (PMMA) (c) Chemical structure of poly(2,2,2-trifluoroethyl methacrylate) (PTFMA). (d) Chemical structure of poly(α-methylstyrene) (PαMS).....	74
Fig. 5-2 (a) The transfer and (b) output characteristics of the color filtering functional devices.....	76
Fig. 5-3 (a) The AFM image of the surface of the red color filter. The surface morphology of the pentacene layers on (b) the red color filter; (c) the red color filter/PTFMA insulator; (d) the tri-layer red color filter/PTFMA/PαMS insulator.....	77
Fig. 5-4 Optical properties of red, green, and blue functional OTFTs: (a) The	

transmission spectra and (b) CIE 1931 coordinates.....	78
Fig. 5-5 (a) The cross sectional illustration of the OTFT with a colored dielectric insulator P6-A. (b) Chemical structure of polymethylmethacrylate (PMMA). (c) Chemical structure of P6-A, X:Y=50:1.	81
Fig. 5-6 (a) $I_{DS}-V_{DS}$ curves and (b) $I_{DS}-V_{GS}$ transfer characteristics of the PMMA and P6-A devices.	82
Fig. 5-7 The AFM image of surface morphology of the pentacene layers on PMMA and P6-A.	84
Fig. 5-8 Optical properties of colored OTFTs: (a) The transmission spectra and (b) CIE 1931 coordinates.....	85
Fig. 6-1 a-IGZO TFT processes.....	87
Fig. 6-2 Optical absorption spectrum of PLD a-IGZO thin film.	90
Fig. 6-3 Illustration of four- point measurement method	91
Fig. 6-4 Thermal conductivity of a-IGZO film.....	91
Fig. 6-5 Calculated activation energy	91
Fig. 6-6 (a) Dark $I_{DS}-V_{DS}$ and (b) $I_{DS}-V_{GS}$ characteristics of PLD a-IGZO TFT.	93
Fig. 6-7 $I_{DS}-V_{GS}$ curves for constant photo flux with the varying light wavelengths.	95
Fig. 6-8 Example of the color filter transmission spectra of the LCD (solid curves) and light emission spectra from multicolor PLED (symbol and dash curves). ..	96
Fig. 6-9 Dependence of PLD a-IGZO TFT minimum off-state drain current (I_{DS-off}), on-state drain current (I_{DS-on}), threshold voltage shift (ΔV_{TH}), subthreshold swing (S), and field-effect mobility (μ_{eff}) on incident photons energy for constant photon flux.....	97
Fig. 6-10 (a) Band diagram of a-IGZO TFT operated under illumination (b) closer look at the channel region	98
Fig. 7-1 Cross-sectional view of inverted-staggered a-IGZO TFT.....	102
Fig. 7-2 Propose density-of-states (DOS) model for a-IGZO. E_C and E_V are conduction and valence band-edge energy, respectively. Solid curves within band-gap represent the exponentially-distributed band tail states (g_{CBa} , g_{VBd}), while the dash curve near the conduction band-edge represents the Gaussian-distributed donor-like oxygen vacancy states (g_{Gd}).	103
Fig. 7-3 Oxygen vacancy in oxide semiconductor.....	105
Fig. 7-4 (a) Output and (b)(c) transfer characteristics for a-IGZO TFT ($W/L=180\mu m/30\mu m$). Both experimental (\bigcirc) and simulation data (solid line: ohmic contact; +: Schottky contact) are presented. Extracted threshold voltage (V_{th}), field-effect mobility (μ_{eff}) and sub-threshold swing (S) are also indicated. Inset of (c): TFT structure used in simulation.....	106
Fig. 7-5 Simulated $I_{DS}-V_{GS}$ curves of a-IGZO TFT in linear region (Drain to source	

voltage, $V_{DS}=0.1V$) for various (a) source / drain contact resistance ($R_{S/D}$) and (b) conduction band tail slope (E_a). (c) Example of using oxygen vacancy states (g_{Gd}) to simulate a-IGZO TFT shifting behavior at high temperature. Real experimental data (\bigcirc) are also shown as reference. 108

Fig. 8-1 Cross-sectional view of proposed ambipolar TFT 110

Fig. 8-2 $I_{DS}-V_{DS}$ curves of ambipolar TFT 111

Fig. 8-3 $I_{DS}-V_{GS}$ curves of ambipolar TFT 112

Fig. 8-4 (a) Cross-sectional view of CMOS-like inverter (b) Schematic circuit of CMOS-like inverter 113

Fig. 8-5 Voltage transfer curve and their corresponding gains of ambipolar TFTs operated in the (a) first quadrant and (b) third quadrant..... 113

Fig. 9-1 Research projects in this study 116

Fig. 9-2 Proposed self-aligned N^+ region at contact area 123



List of Tables

Table 1-1	Molecular structures of common p-type organic semiconductors	10
Table 1-2	Molecular structures of common n-type organic semiconductors	11
Table 1-3	The specification of 12.1” WXGA AMOLED display.....	22
Table 3-1	Electrical parameters of the OTFTs in this study.....	42
Table 4-1	Water contact angle of different surface.....	53
Table 4-2	Electrical parameters in this study	56
Table 7-1	Key simulation parameters used in this study.....	105
Table 9-1	Summary & comparison for high κ gate insulator in OTFTs	117
Table 9-2	Summary & comparison for color-filtering OTFTs	119
Table 9-3	Summary & comparison for photosensitivity study for a-IGZO TFTs.....	120
Table 9-4	Summary & comparison for modeling and simulation of a-IGZO TFTs..	121
Table 9-5	Summary & comparison for ambipolar TFTs and inverters	122

Chapter 1

Introduction

1.1 Active Matrix Flat Panel Electronics

Although cathode-ray tube (CRT) has been the dominant electronic display for about 75 years, flat-panel displays (FPDs) have recently edged the CRT in many applications. The active-matrix liquid-crystal display (AMLCD), the most successful FPD to date, has conquered virtually all modern portable display applications, including notebook computers, personal digital assistants, hand-held telephones, and camera viewfinders. Liquid-crystal displays (LCDs), when first used in computers, were fabricated as passive-matrix-addressed displays with diagonal sizes of less than 10 inches. Yet, they are currently available with about 17 inches sizes in computers and with about 23 inches sizes in desktop monitors, and 46 inches sizes in TVs [1].

Fig. 1-1 shows several applications of AMLCDs. These products are all around our daily life.

Generally, active matrix TFT backplane, which is used in AMLCDs and recently in AMOLEDs (Active Matrix Organic Light Emitting Diode), is an array of pixels with vertical and horizontal programming lines. Rows are connected to gates of switching TFT of the pixels, columns drive TFT sources, and drains are connected to the liquid crystal (LC). Gates and sources are scanned and programmed periodically by external CMOS driver for every pixel in a-Si:H AMLCD. Low temperature poly-silicon AMLCDs, due to better stability of poly-Si electrical characteristics, can have built-in drivers which reduces fabrication costs. Also there are some circuit

requirements for AMLCDs that have to be addressed based on signal timings. For example, for 60 Hz operation the line time is 34.7 μ sec, so the charging time of each pixel must be less than this number to maintain the 3 contrast of pictures. This number for a 852 \times 480 wide VGA (WVGA) display with a pixel pitch of 0.974 mm is about 16.9 μ sec. [1]



Fig. 1-1 AMLCD applications

Another generation of FPD which is growing very fast is AMOLED displays (Fig. 1-2). Fast response time ($< 10 \mu$ sec), large viewing angle ($\sim 170^\circ$), high contrast and brightness, light weight, lower power consumption, and high efficiency have given AMOLED displays very promising future [2]. OLED displays can potentially be used in different fields such as automotive, consumer electronics, digital video technologies, industrial, scientific medical applications, and telecommunications. Recently, Samsung electronics, the leader in TFT-LCD (Thin-film transistors-LCD)

technology announced manufacture of the largest single-panel AMOLED display with 40-inch screen and the highest resolution at 1280 pixels by 800 pixels, implemented by amorphous silicon technology.

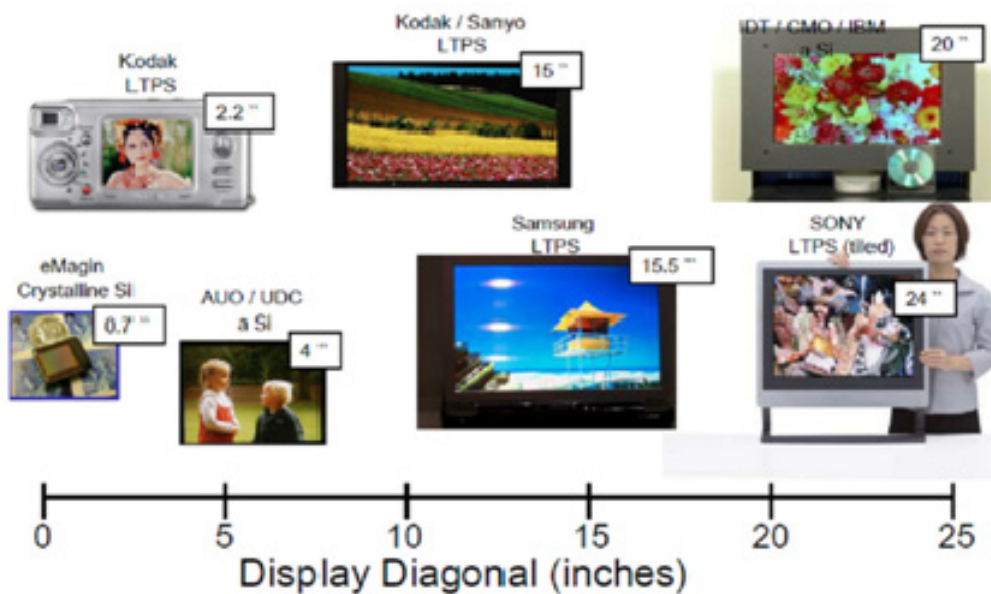


Fig. 1-2 Prototypes of AMOLED



1.2 Future displays

Today's digital displays are far from ideal. They are heavy, somewhat fragile and they lack the resolution, flexibility or portability of paper. They are also expensive. Flexible displays are expected to be comprehensively applied to paper-like displays (e-paper) and other display purposes varied by the usage of the product. In addition, displays combined with circuits (system-on-panel), wall hanging large screens, and 3D displays are also approaching our life (Fig. 1-3). As a result, traditional amorphous silicon thin-film transistors (a-Si:H TFTs) will not be suitable for bendable substrates and fast switching applications. Samsung mentioned that LCD-TVs trend to have UD resolution (3840 x 2160) and more than 120Hz scan rate in SID 2008 (Fig. 1-4). For this reason, it will increase the number of gate line

and frequency. Consequently, we have to use high-mobility devices to enhance the chargeability. Furthermore, for large scale display, TFT uniformity should be taken into consideration, so amorphous type active layer is the key material.

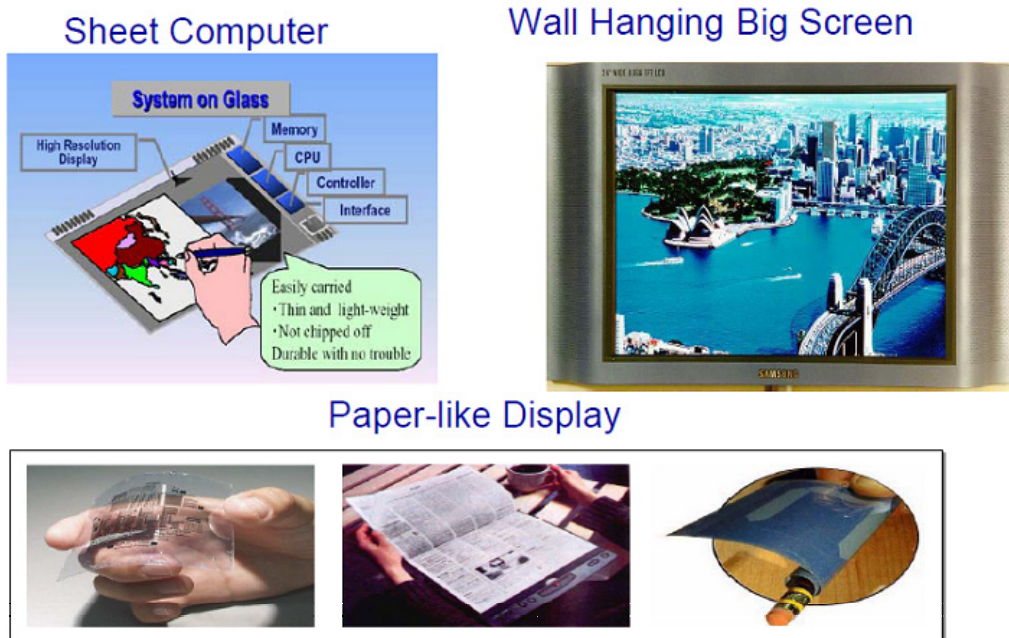


Fig. 1-3 Future displays

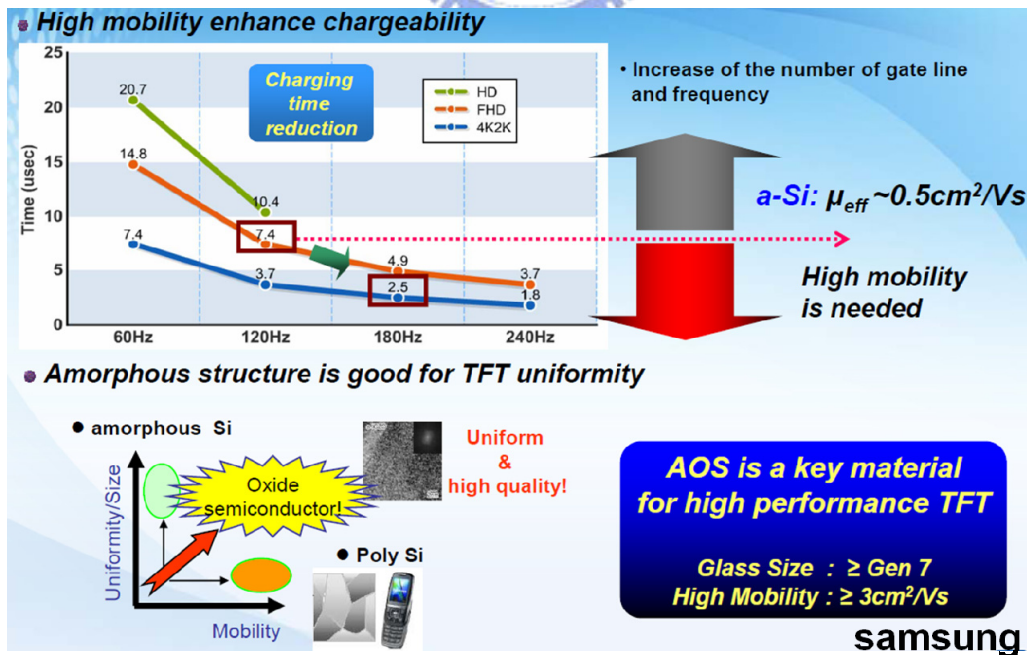


Fig. 1-4 TFT requirements for future large scale displays (Samsung SID08)

1.3 Thin-film transistors and operation

Traditional thin-film transistor composes of a semiconductor layer, a gate insulator layer, and 3 electrode terminals called gate, source, and drain. Fig. 1-5(a) shows the basic layout of a bottom-gate thin-film transistor (TFT) and energy band diagrams through the gate of an n-type accumulation-mode TFT under three modes of operation. Fig. 1-5(b) shows the equilibrium energy band diagram, i.e., no bias is applied to the gate contact. As a negative bias is applied to the gate, delocalized electrons in the channel are repelled from the semiconductor/gate interface and create a depletion region, of positive charge, as indicated by the positive curvature in the conduction and valence bands in Fig. 1-5(c) near the insulator. When a positive voltage is applied to the gate contact, delocalized electrons in the channel are attracted to the semiconductor/insulator interface, creating electron accumulation at the interface, as indicated by the negative curvature in the conduction and valence bands in Fig. 1-5(d) near the insulator. The delocalized electrons accumulated near the semiconductor/insulator interface when a positive voltage is applied to the gate contact provide a path for current conduction, which is denoted as the channel. As a positive voltage is applied to the drain contact of the TFT, these delocalized electrons in the accumulation layer are extracted from the channel, giving rise to drain current through the TFT. At small positive drain voltages, i.e., voltages significantly less than the gate voltage minus the turn-on voltage, $V_{DS} \ll V_{GS} - V_{ON}$, the drain current conduction can be modeled as a linear relationship given by

$$I_{DS} = (1/2)\mu C_{ox}(W/L)(2(V_{GS} - V_{ON})V_{DS} - V_{DS}^2) \quad \text{eq. (1-1)}$$

where the turn-on voltage (V_{ON}) is the voltage at which current conduction

begins to increase with an increase in the gate voltage, C_{ox} is the oxide capacitance, μ is the mobility of the electrons, W is the width of the channel, L is the length of the channel, V_{GS} is the gate to source voltage, and V_{DS} is the drain to source voltage. When the drain voltage reaches the pinch-off voltage, i.e., the voltage at which the channel near the drain is depleted of carriers, the drain current saturates, thus becoming independent of the drain voltage, and is given by

$$I_{DS} = (1/2)\mu C_{ox}(W/L)((V_{GS} - V_{DS})^2) \quad \text{eq. (1-2)}$$

Transistors are classified into two different types, based on whether drain current flows through the TFT when no voltage is applied to the gate. If the TFT is on, i.e., drain current flows through the TFT when no voltage is applied to the gate, the TFT is distinguished as a depletion-mode device. If the TFT is off, i.e., only leakage current flows through the TFT with no voltage applied to the gate, the TFT is classified as an enhancement-mode TFT.

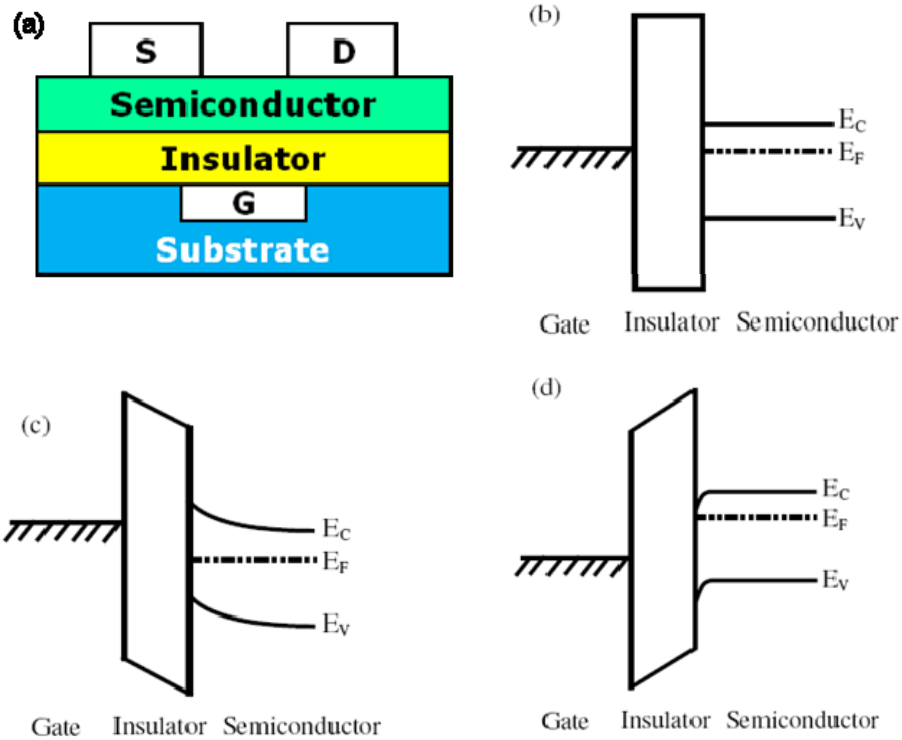


Fig. 1-5 A bottom-gate TFT structure and several energy band diagrams. (a) TFT structure. Energy band diagram when (b) biased in equilibrium. When (c) a negative voltage and (d) a positive voltage is applied to the gate.

1.4 Organic thin-film transistors

1.4.1 Introduction to organic semiconductor and pentacene

Organic materials are suitable to be made on the flexible substrates because of their unique molecular properties. Many interesting applications such as flexible displays, smart cards, radio frequency identification tags, e-skin on robots, as well as light-emitting diodes and lasers have been demonstrated (Fig. 1-6). Much progress in this field has been made to improve the material properties and the process techniques.



Fig. 1-6 Applications of organic transistors.

Since Alan Heeger, Alan MacDiarmid, and Hideki Shirakawa first began studying how to alter the level of conductivity of polymers in 1976, the interest in conducting polymers has exploded. [3,4] While investigating the chemistry of conducting polymers, Alan Heeger's group discovered the conductivity of polymers could be controlled from insulating, to semiconducting, to metallic conducting [3]. By carefully controlling chemical reactions, the level of doping in polymers can be changed several orders of magnitude. This is a typical characteristic of conventional semiconductors such as silicon.

The wide range of conductivity of these polymers is due to their unique structure. Polymers consist of small unit cells containing a hydrogen-carbon configuration, which become chemically bonded together to form a giant molecule, usually called a macromolecule. Bonding occurs as the carbon atoms are brought together to form the backbone of the molecule, but leaves one π -bonded electron weakly bonded [3]. The weakly bound π -electron can then give rise to charge carrier transport in the

presence of an electric field, which takes place along the carbon bonded backbone [3]. Controlling the conductivity is simply a process of doping the polymer to capture or release more electrons in the macromolecule.

Chemists control the conductivity through various methods as shown in Fig. 1-7 [3]. These methods include oxidation/reduction reactions, electrochemical methods, acid-base reactions and photodoping [3]. An interesting phenomenon of organic semiconducting polymers is the vast array of available materials reported [3]. Although p-type organic semiconductors were studied and developed first, n-type are now under extensive investigation. Tables 1-1 and 1-2, show the progress of MOSFET transistors based on both p and n-type organic semiconductors, respectively, and how the leading edge materials have changed over the years.

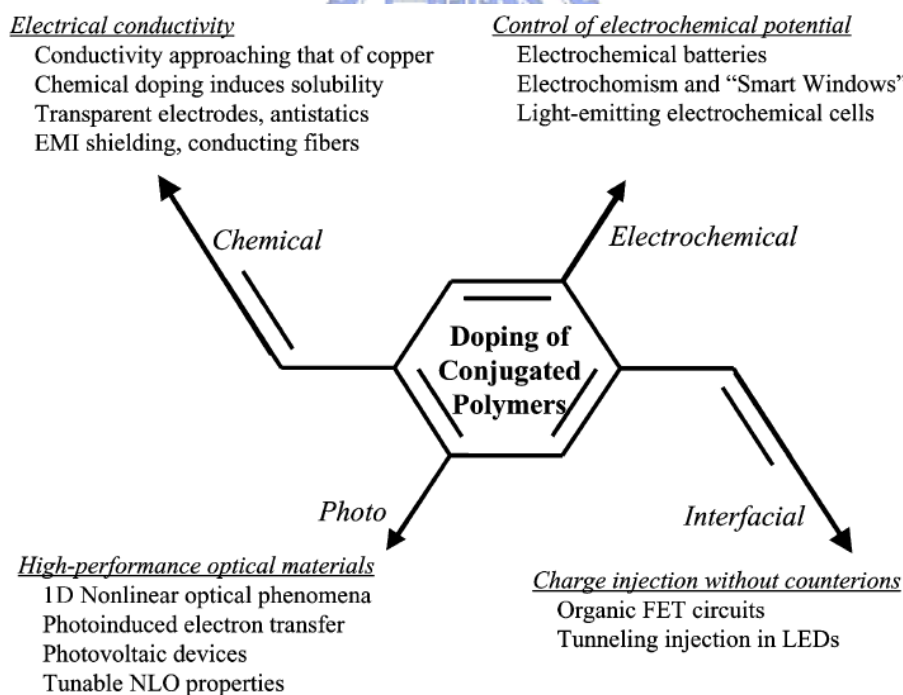


Fig. 1-7 Doping mechanisms and related applications.

Table 1-1 Molecular structures of common p-type organic semiconductors

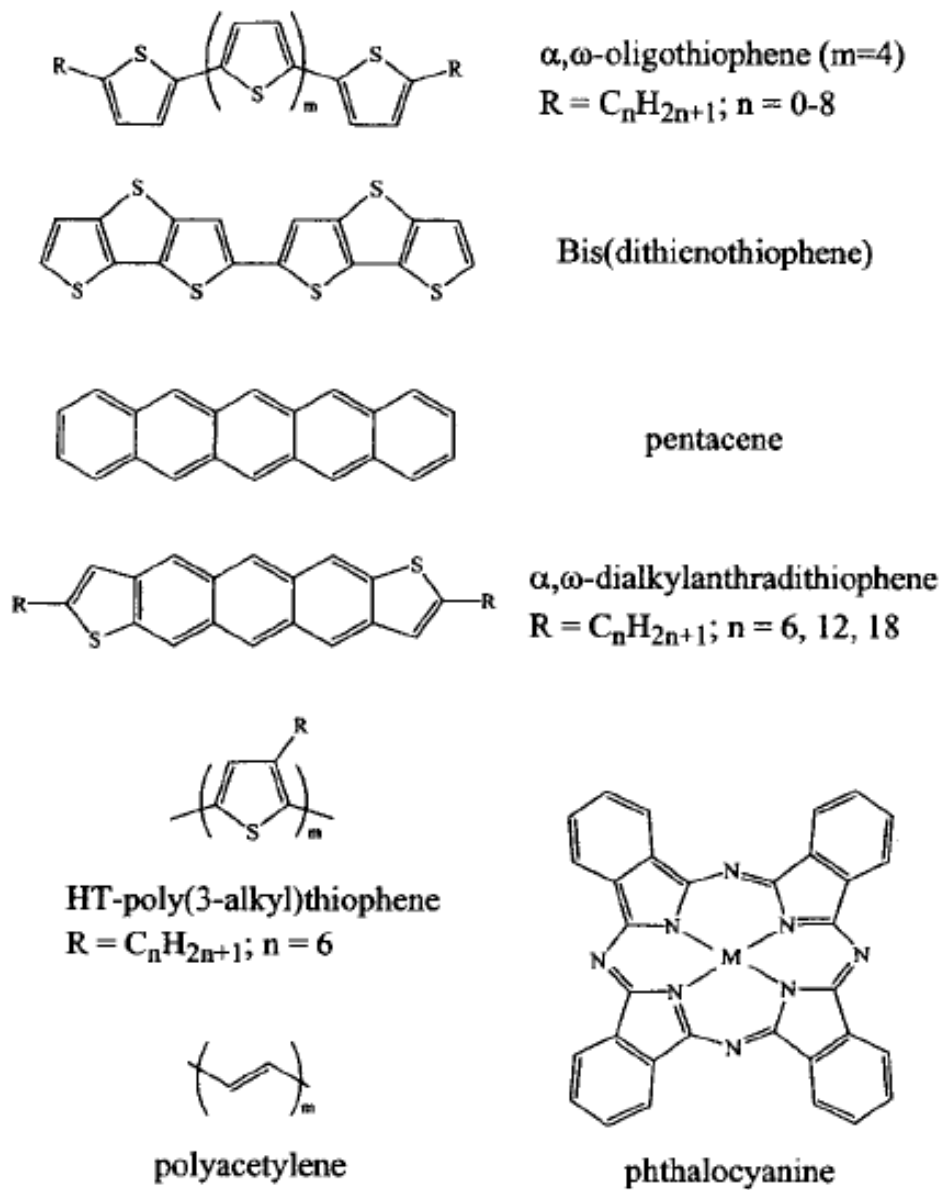
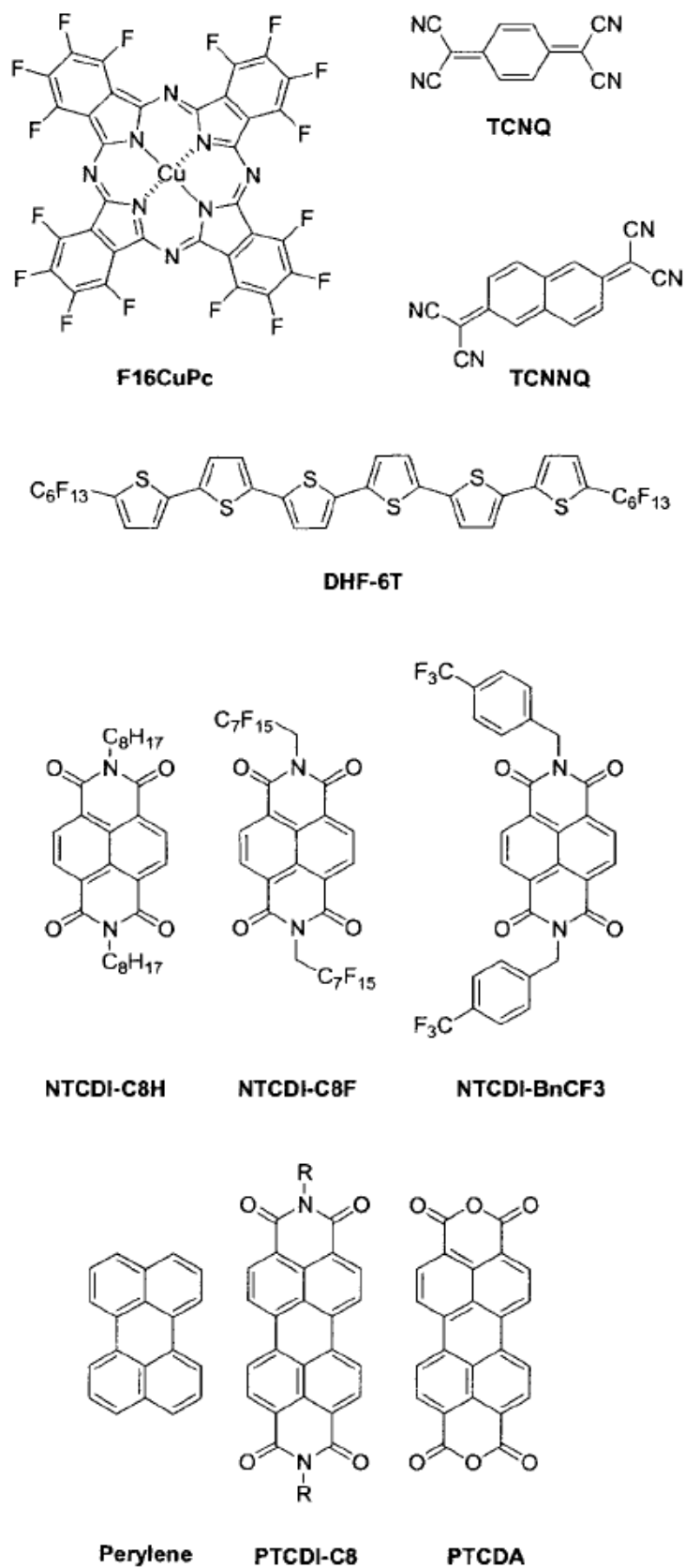


Table 1-2 Molecular structures of common n-type organic semiconductors



Organic semiconductors can be organized into two categories. The first is plastics or polymers. The backbone of these materials is based on a repeating chain of hydrogen and carbon in various configurations with other elements. Much work has been accomplished with these materials, but they have relatively poor mobilities (10^{-4} cm²/Vs [3]). The second group is based on short organic molecules called oligomers. Crystals of these materials are held together by weak van der Waal forces. Devices fabricated from these materials have been demonstrated the highest observed mobilities in organic semiconductors (2.4 cm²/Vs [4]). However, the speeds of these devices still can not be comparable to traditional transistors based on inorganic semiconductors, such as silicon MOSFETs. On the other hand, the organic transistors are not driven by an interest in replacing silicon devices, but rather in developing devices for especially low cost applications. Currently, pentacene is one of the small molecule semiconducting materials that have received a great deal of attention [4]. Recent developments have yielded the highest charge carrier mobilities of any organic semiconductor [4]. Pentacene is one of a group of materials called polyacenes. A characteristic of this group of materials is its structural formation. It begins with a carbon-carbon covalently bonded ring of six carbon atoms called benzene. As shown in Fig. 1-8, every other carbon bond in the benzene ring is a double bond. Because carbon has four available electrons for bonding in its outer shell, one is used in a single C-C bond, two in a double C-C bond, and then the final electron is bonded with a dangling hydrogen atom. Therefore, the final molecule is a ring of six carbons with a hydrogen atom attached to each carbon atom. Pentacene has five benzene rings bonded together (its structure can be seen in Fig. 1-8) and therefore, its chemical formula is C₂₂H₁₄.

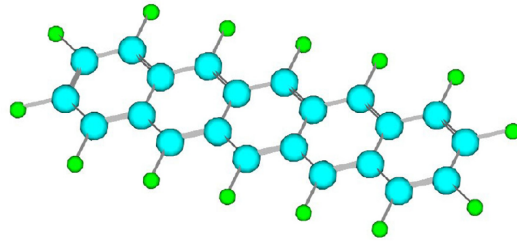


Fig. 1-8 Pentacene molecule structure

1.4.2 Issues of organic thin-film transistors

There are many remaining issues of OTFTs such as high operating voltage, photosensitivity, and reliability which need to be resolved for practical applications.

High operating voltage

There is a difference in their operating range between organic versus inorganic TFTs. Due to the very low mobilities of carriers in organic semiconductors, larger electric fields are needed to achieve the same current level. In addition, typical OTFTs have larger channel lengths (few μm versus submicron for silicon). As a result, typical organic transistors will operate with a gate and drain voltage in range of 0-100V as seen in Fig. 1-9. [5]

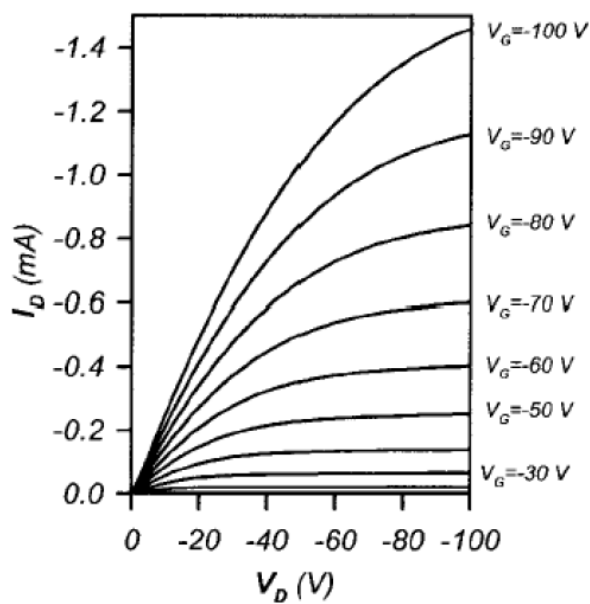


Fig. 1-9 Typical operating range of OTFT.

Photosensitivity

Photosensitivity is one of the important issues for the display applications, such as liquid-crystal display (LCD), organic light emitting diode, and image sensor. The band gap of pentacene is ~ 1.7 to 2.3 eV, so that the light absorption in the visible range is high [6]. A significant increase in the photocurrents in a polymer TFT based on regioregular poly (3-octylthiophene) and in an OTFT based on 2,5-bis(biphenyl-4-yl)-thieno[3,2-b]thiophene has been reported [7,8]. On the other hand, the photoinduced doping in pentacene TFT has been also reported [9]. Fig. 1-10 shows the transfer curves of the OTFT under dark and light illumination. Off-current increases significantly under illumination. The minimum drain current increases with increasing the intensity, and increases by five orders of magnitude at 1350 lux. Specifically, the current in the subthreshold region increases remarkably, resulting in the increase of subthreshold swing (S). The electron-hole pairs generated by light illumination increase the off-state current significantly result in threshold voltage shift (V_{TH} shift).

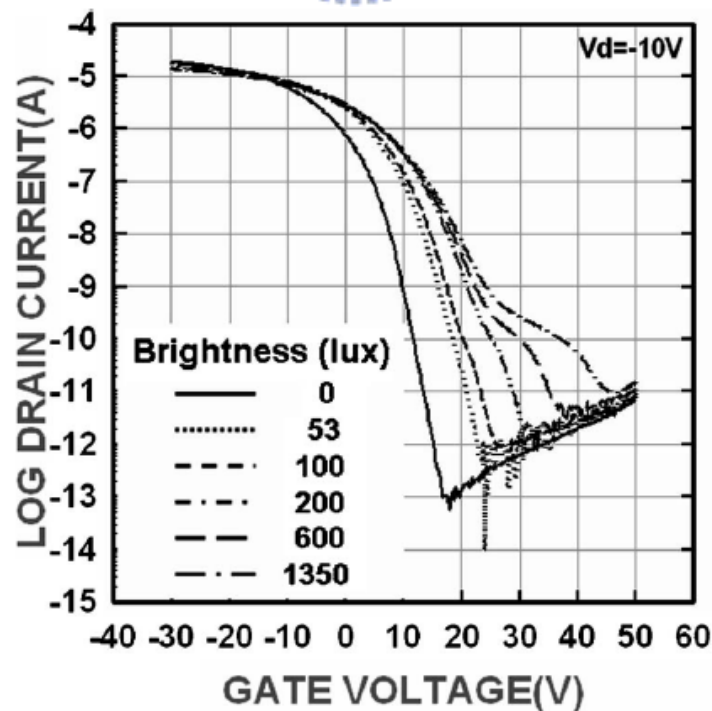


Fig. 1-10 Transfer characteristics under illumination for an OTFT.

Reliability

Most of the traditional OTFTs are made on the silicon substrate because it is easier to be processed. Fig. 1-11(a) shows the cross-sectional view of traditional pentacene TFTs where N^{++} silicon serves as the gate electrode; SiO_2 is the gate insulator; pentacene is the active layer and gold electrode as source and drain electrode. Figs. 1-11(b) and (c) show transfer curves and normalized output drain current versus stress time, respectively. The transfer performance of bare SiO_2 device shows that subthreshold swing is larger than 5 V/decade comparing to conventional TFTs. The subthreshold swing (S) is poor and turn-on voltage is positive, suggesting that pentacene can not be well deposited onto pure SiO_2 surface. After introducing HMDS (Hexmethylidisilane) between SiO_2 and pentacene, the S is much improved and the turn-on voltage becomes closed to zero, but the output current decays dramatically. In short, the device interface treated by poly(α -methylstyrene) (P α MS) shows S and output current decays slower than bare SiO_2 device and HMDS treated device.

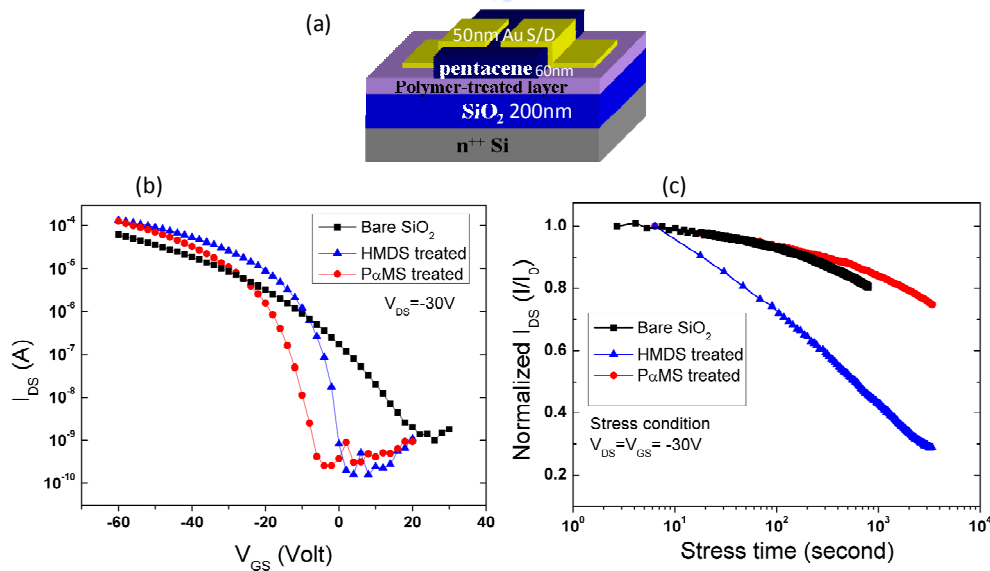


Fig. 1-11 (a) Cross-sectional view of a conventional OTFT. (b) Transfer curves of non-modified, HMDS treated, and PaMS treated pentacene TFTs. (c) Normalized output current under bias stress of these devices.

1.4.3 Organic TFT state-of-arts

SONY has reported 2.5-inch QQVGA OTFT-driven full-color and top-emission AMOLED displays on glass as well as plastic substrates with brightness > 100 cd/m^2 under a practical signal-voltage range of 12 V at SID 2007. [10] The structure and the properties of the display on the glass can be reproduced on a PES film using the same fabrication procedure. The display fabricated on the film has the advantages of being lightweight, thin and flexible. SONY suggested that a combination of OTFTs and OLEDs is a key technology for the future flexible displays. Fig. 1-12 shows a photograph of the display fabricated on the PES film while the film is being flexed. The electrical properties of the OTFTs and OLEDs on the film are comparable to those on the glass substrate, and the display device on the PES substrate reproduced the electrical and optical specifications are also shown in Fig. 1-12.



Display Size	2.5-inch diagonal
Number of Pixels	160 × RGB × 120 (QQVGA)
Pixel Size	318 μm × 318 μm
Resolution	80 ppi
Number of Colors	16,777,216
Peak Luminance	> 100 cd/m^2
Contrast Ratio	$> 1000:1$
Operation Scheme	2T-1C Voltage Programming
Scan Voltage	30 V p-p
Signal Voltage	12 V p-p
V _{cc} – V _{cath}	20 V

Fig. 1-12 Flexible AMOLED driven by OTFTs and specification.

1.5 Amorphous In-Ga-Zn-O thin-film transistors

1.5.1 Introduction to metal-oxide semiconductor

The most important feature of semiconductors is in the controllability of carrier concentration over several orders of magnitude. A unique advantage of amorphous materials over crystalline materials is capability of large-area deposition of uniform thin films at low temperatures. Research on amorphous semiconductors started in 1950s to seek materials which can have both of these advantages [11]. Recently, amorphous oxide semiconductors (AOSs) have attracted much attention because AOS thin-film transistors exhibit large mobilities with low fabrication temperature. The conduction bands of the AOSs are derived from the ns orbitals of heavy metal cations such as In^{3+} , Ga^{3+} , and Zn^{2+} .

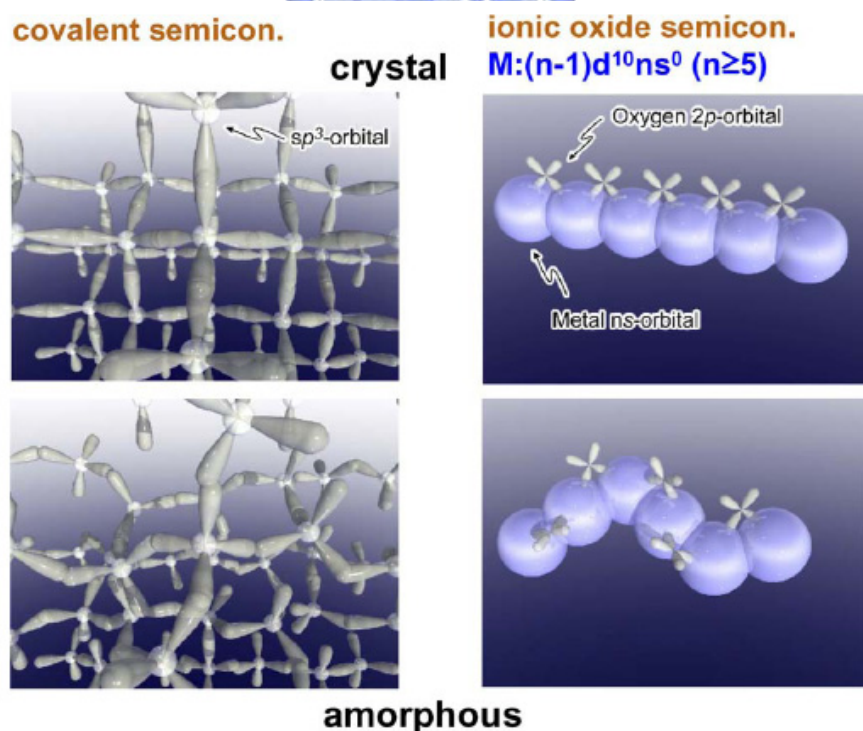


Fig. 1-13 Schematic orbital drawing of electron pathway (conduction band bottom) in conventional silicon-base semiconductor and ionic oxide semiconductors.

The spatial spread of this vacant s-orbital is so large that direct overlap between the s-orbitals of the neighboring cations is possible in heavy metal oxides, and therefore an effective mass of electron is small in these oxides. Electron transport path is also very efficient because of the large radii and large overlap between the adjacent ns orbitals of spherical symmetry, which is less sensitive to the arrangement of atoms. Oxide semiconductors have shown comparable mobilities both in crystalline and amorphous phases, while covalent semiconductors such as silicon shows at least two to three orders of magnitude smaller mobilities in the amorphous phase. (Fig. 1-13)

One of the most interesting oxide semiconductor for TFT application is In-Ga-Zn-O. Fig. 1-14 shows the electron mobilities and concentrations evaluated from the Hall effects for amorphous thin films. It is clear that the mobility is primarily determined by the fraction of In_2O_3 content and the highest value of $\sim 40 \text{ cm}^2/\text{Vs}$ is obtained around the samples containing the maximum In_2O_3 fraction. A critical issue of semiconductor materials for TFT applications is controllability of carrier concentration. This is particularly serious for AOSs because electron carriers can be easily generated. In practice, the effect of binary amorphous materials in the In_2O_3 -ZnO system is employed in commercial flexible transparent conductive films by depositing on the plastic sheet. Thus, the effect of partial oxygen pressure were studied during the deposition processes on the carrier concentration in a-InGaZnO₄ and a-In₂Zn₃O₆ and obtained the results as shown in Fig. 1-15. The carrier concentration in the a-InGaZnO₄ is distinctly reduced to below 10^{13} cm^{-3} by reducing P_{O_2} to 8 Pa, whereas it remains at 10^{18} cm^{-3} in the a-In₂Zn₃O₆ deposited under the same condition. It is thus evident that incorporation of Ga^{3+} is very effective for suppressing electron carrier generation. Ga^{3+} is supposed to attract the

oxygen ions tightly due to its high ionic potential (+3 valence and small ionic radius), and thereby suppressing electron injection which is caused by oxygen ion escaping from the thin film. The Hall mobility in the samples around the chemical composition of InGaZnO₃ is not sensitive to the variation in the composition as shown in Fig. 1-14. [12]

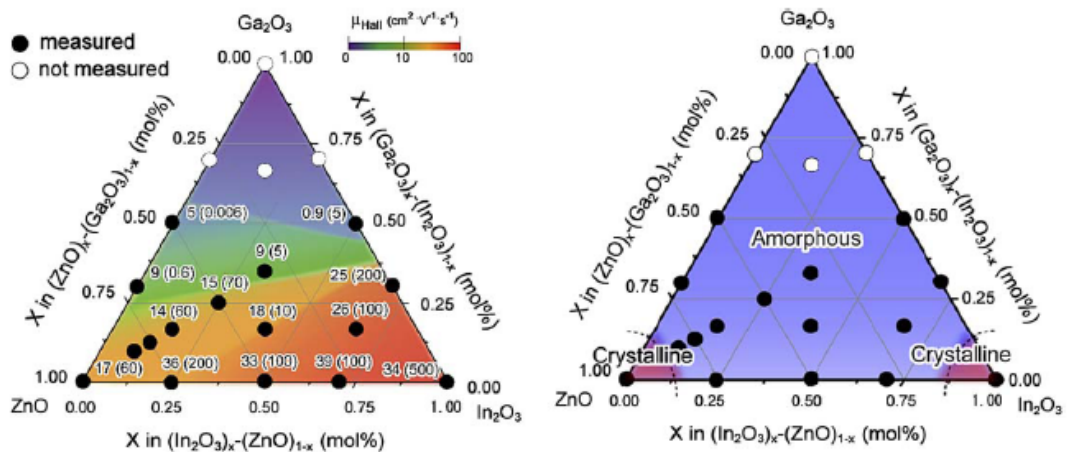


Fig. 1-14 The amorphous formation region (right) and the electron mobilities and concentrations evaluated from the Hall effects for the amorphous thin films (left) in the In₂O₃–Ga₂O₃–ZnO system. The thin films were deposited on a glass substrate by pulsed laser deposition under deposition atmosphere of PO₂ = 1 Pa. Number in the parenthesis denotes carrier electron concentration ($\times 10^{18}$ cm⁻³). [12]

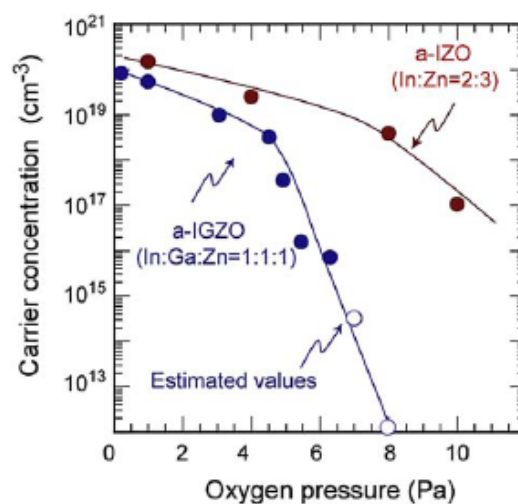


Fig. 1-15 The carrier concentration as a function of O₂ pressure during the deposition in a-InGaZnO₃ and a-In₂Zn₃O₆. [12]

1.5.2 a-IGZO TFT state-of-arts

Samsung demonstrated a full color 12.1-inch WXGA active-matrix organic light emitting diode (AMOLED) display by using a-IGZO TFTs as an active-matrix back plane at SID 2008 [13]. It was found that the fabricated AMOLED display did not suffer from the well known pixel non-uniformity of luminance, even though the simple structure consisting of 2 transistors and 1 capacitor was adopted as a unit pixel circuit, which was attributed to the amorphous nature of IGZO semiconductor. The n-channel a-IGZO TFTs exhibited the field-effect mobility of $8.2 \text{ cm}^2/\text{Vs}$, threshold voltage (V_{TH}) of 1.1 V, on/off ratio of $>10^8$, and subthreshold swing (S) of 0.58 V/decade. The AMOLED display with a-IGZO TFT array would be promising for large size applications such as HDTV because a-IGZO semiconductor can be deposited on large glass substrate ($> \text{Gen. 7}$) using conventional sputtering system. Fig. 1-16 shows the schematic cross section of the IGZO TFTs, which have an inverted staggered bottom gate architecture with an etch stopper layer (ESL). For an a-IGZO TFT without an ESL, severe degradation of the S and the uniformity of V_{TH} were observed. Consequently, we chose ESL-type structure rather than back-channel etch structure (BCE-type), which is generally adopted for liquid crystal displays.

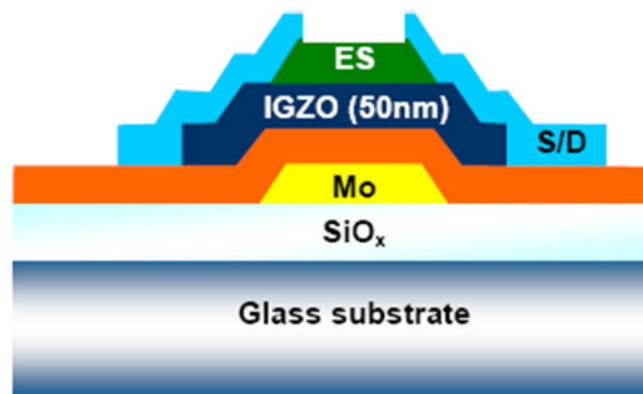


Fig. 1-16 The cross sectional view of Samsung's a-IGZO TFT. [13]

The photo-acryl as an ESL adversely affected the property of the subthreshold swing in the resulting a-IGZO TFT, as shown in Fig. 1-17. Although the reasonable mobility ($10 \text{ cm}^2/\text{Vs}$) and Ion/off ratio ($>10^7$) were obtained, the S.S. value (1.0 V/dec) was rather poor. On the other hand, the SiOx material as an ESL resulted in the improvement of the subthreshold characteristics: the a-IGZO TFT with the ESL of photo-acryl exhibited an S value of 0.58 V/dec without any loss of device properties ($\mu_{\text{FE}}=8.2 \text{ cm}^2/\text{Vs}$, a $V_{\text{TH,sat}}$ of 1.1 V , and an $I_{\text{on/off}}$ of $> 2.0 \times 10^7$), as shown in Fig. 1-17. It is evident that the S value, thus, the total trap density including the interfacial trap density and bulk trap density of channel layer itself, can be reduced by proper choice of ESL material. It should be noted that the overall device performances of amorphous oxide TFTs are better than those of microcrystalline Si and amorphous Si TFTs.

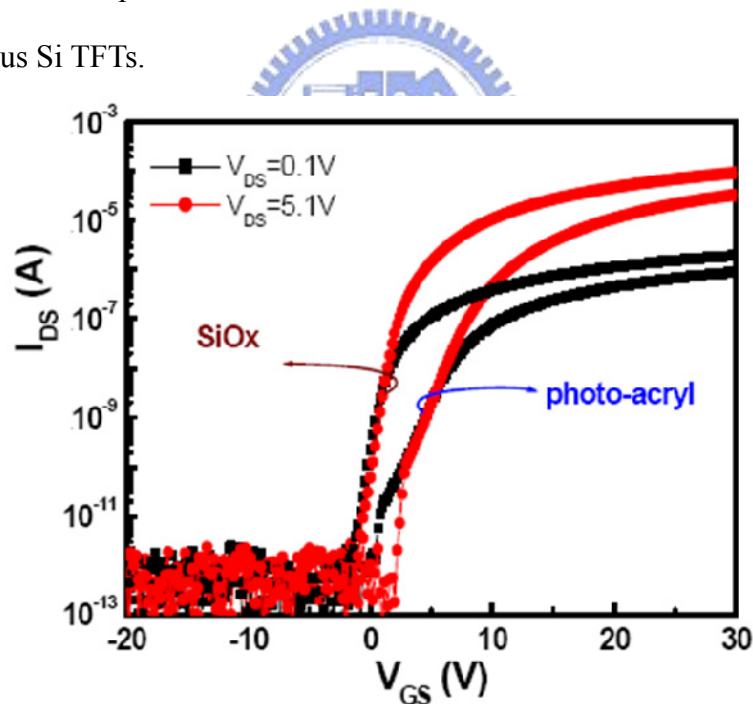


Fig. 1-17 The representative transfer curves of the a-IGZO TFTs with $W/L=25/10\mu\text{m}$ with ESL. The S value and V_{TH} were very sensitively affected by the material of ESL. [13]

The specification of 12.1-inch AMOLED display by utilizing a-IGZO TFTs as backplane is summarized in Table 1-3. The display has the pixel number of 1280×RGB×768 with the resolution of 123 ppi. Its subpixel pitch is 69× 207 μm² composed of 2 transistors and 1 capacitor. The channel length for driving transistor was designed to 10 μm, but the kink effect, which appears in poly-Si TFT with the same channel length, was not observed in output characteristics [13]. The scan driver was integrated on the panel and its functionality was successfully demonstrated. The structure has the transparent anode, organic layers, and cathode on the TFT backplane with bottom emission structure. The OLED device structure consisted of a hole injection layer (HIL), a hole transport layer (HTL), a RGB emitting layer (EML), an electron transfer layer (ETL), an electron injection layer (EIL), and a cathode. Phosphorescent red and fluorescent green and blue dyes were used as emitting materials. Fig. 1-18 shows an image of the 12.1” WXGA AMOLED display.

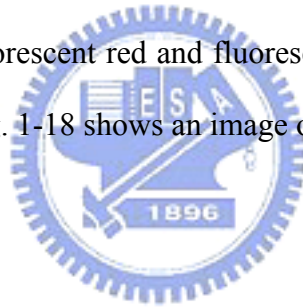


Table 1-3 The specification of 12.1” WXGA AMOLED display. [13]

Items	Specification
Diagonal size	12.1 inch
No. of pixels	1280 x RGB x 768
Sub pixel pitch	69 x 207 μm ²
Resolution	123 ppi
Panel size	283 x 181 mm ²
Pixel element	2Tr 1Cap
Gray	256 gray
Scan driver	Integration
Color coordinate	White (0.31, 0.31) Red (0.67, 0.32) Green (0.3, 0.65) Blue (0.15, 0.15)



Fig. 1-18 The display image of Samsung's 12.1" WXGA AMOLED display

1.6 Ambipolar TFTs

An ambipolar transistor is one in which both electrons and holes are accumulated depending on the applied voltages [14]. They exhibit characteristic transfer and output curves, which can be understood easily, considering the potentials applied to the source, drain, and gate electrodes relative to one another. Let us assume a transistor at a given positive drain voltage V_{DS} (the source potential is held at ground, $V_S = 0$) and start with a positive gate voltage of $V_{GS} = V_{DS}$. Just as in a unipolar transistor, the gate is more positive than the source electrode and thus electrons are injected from the source into the accumulation layer and drift toward the drain, given that $V_{GS} > V_{Th,e}$ ($V_{Th,e}$) threshold for electron accumulation). Only one polarity of charge carriers is present, and we call this the unipolar regime. On the other hand, when V_{GS} is smaller than V_{DS} , the gate potential is more negative than that of the drain electrode by $V_{GS} - V_{DS}$. While, for $V_{GS} < V_{Th,e}$, the source will not inject electrons, the drain electrode in an ambipolar transistor will inject holes into the channel if $V_{GS} - V_{DS} < V_{Th,h}$ ($V_{Th,h}$) threshold for hole accumulation).

Thus, one should actually now speak of the drain electrode as a hole source. A hole current will flow, and thus, the measured drain current will be high, not like in a unipolar, n-channel transistor, which would now be in an off-state. If the gate potential is somewhere between V_D and V_S so that it is bigger than $V_{Th,e}$ but also $V_{GS} - V_{DS} < V_{Th,h}$ (Fig. 1-19(a)), both the source and drain electrode will inject the respective charge carriers and thus both electrons and holes are present in the channel. This regime is called the ambipolar regime, in contrast to the unipolar regime, where only one polarity of charges is present in the channel for any particular biasing condition. Figs. 1-19 (c) and (d) show the I_{DS} - V_{GS} and I_{DS} - V_{DS} curves of ambipolar TFTs [14].

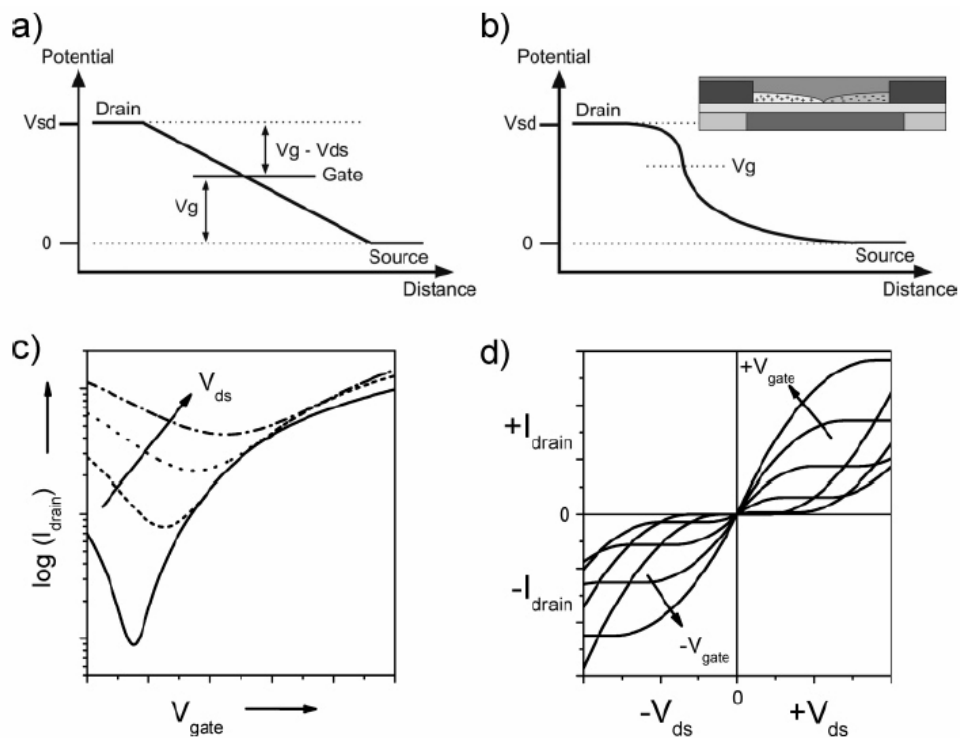



Fig. 1-19 (a) Illustration of the source, drain, and gate potentials with respect to each other in a field-effect transistor. (b) Channel potential in the ambipolar regime with two separate channels of holes and electrons that meet within the transistor channel, where opposite charge carriers recombine (inset). (c) Transfer characteristics for an ambipolar transistor (d) Output characteristics for the same transistor for positive (first quadrant) and for negative (third quadrant) V_{GS} and V_{DS} , respectively.

1.7 CMOS inverter

CMOS (complementary-metal-oxide-semiconductor) inverter is the simplest CMOS logic circuit. The inverter circuit and standard symbol are shown in Fig. 1-20(a) and (b), respectively [15]. When a low voltage (0 V) is applied at the input, the top transistor (P-type) is conducting (switch closed) while the bottom transistor behaves like an open circuit. Therefore, the supply voltage (5 V) appears at the output. Conversely, when a high voltage (5 V) is applied at the input, the bottom transistor (N-type) is conducting (switch closed) while the top transistor behaves like an open circuit. Hence, the output voltage is low (0 V) (Fig. 1-20(c)). The function of this gate can be summarized by the following table:



Input	Output
High	Low
Low	High

The output is the opposite of the input - this circuit inverts the input.

Notice that always one of the transistors will be an open circuit and no current flows from the supply voltage to ground.

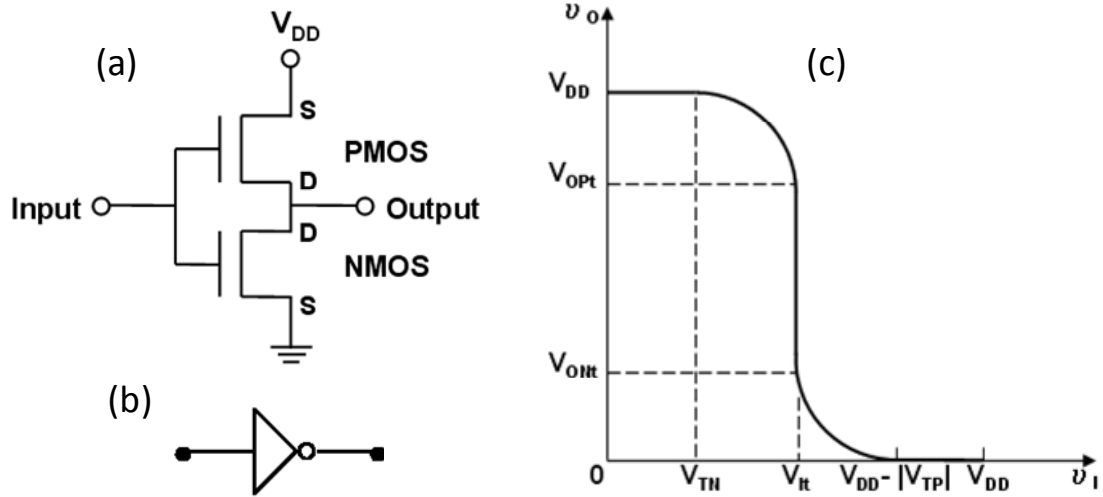


Fig. 1-20 (a) CMOS inverter circuit (b) standard symbol (c) output/input voltage diagram

1.8 Motivation

The future display backplanes are divided into two parts. One is for flexible displays (such as e-paper), the other one is for large scale and fast switching displays. In my thesis research, I would like to develop potential TFT backplanes. Pentacene TFTs are studied for flexible displays, and amorphous In-Ga-Zn-O (a-IGZO) TFTs are studied for large scale and high speed applications. In the pentacene TFT part, methods of reducing operating voltage and minimizing photosensitivity of OTFTs are proposed and realized. We also have demonstrated the color-filtering functional organic TFTs. As for a-IGZO TFTs, there are rare researches focused on the photosensitivity and simulation/modeling. We first study the intrinsic properties of a-IGZO TFTs under illumination with different wavelengths. Furthermore, oxygen vacancies are introduced into density of states for simulation, which agrees well with experimental data. This fundamental study can be a good reference for the transparent electronic applications. Finally, we try to combine pentacene/a-IGZO as active layer. These ambipolar TFTs have both n-type and p-type characteristics. A

CMOS-like inverter can be the basic circuit for display applications.

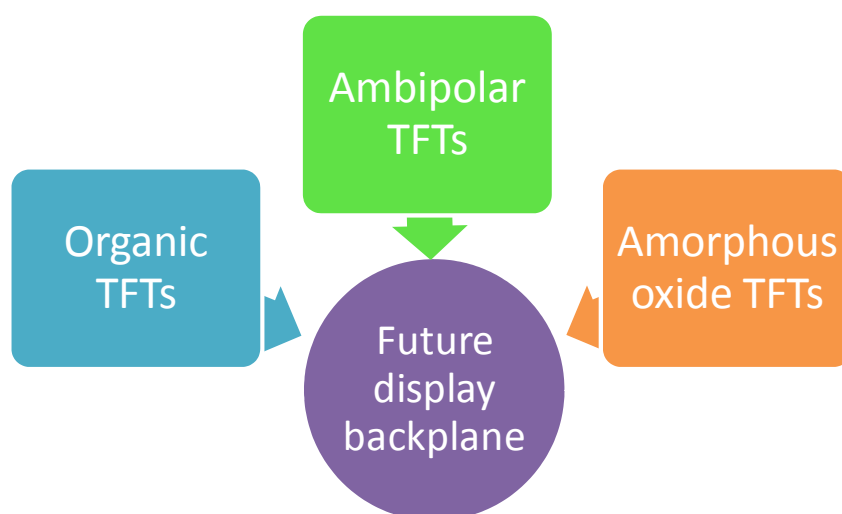
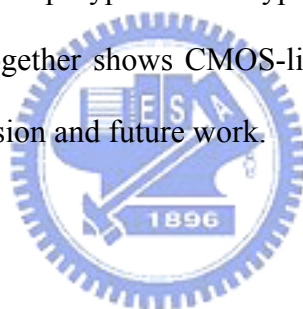


Fig. 1-21 Organic TFTs, amorphous oxide TFTs, and ambipolar TFTs of this study for future display backplane

1.9 Organization of dissertation

This dissertation is divided into eight chapters. The first chapter goes through the brief introduction of TFT applications, OTFTs, a-IGZO TFTs, and ambipolar TFTs. Besides, motivation and organization have also provided. The second chapter presents the experiments and equipments for OTFTs, a-IGZO TFTs, and ambipolar TFTs. The third chapter discusses the high-operating-voltage issue of OTFTs. We used polymer/TiO₂ high dielectric nanocomposite dielectric as gate insulator to produce more field-effect carriers. Different percentage of TiO₂ nanoparticles and surface polarity of dielectric layer have been discussed. In addition, flexible OTFTs are also demonstrated. The fourth chapter describes the photosensitivity and operating voltage can be reduced by blending TiO₂ nanoparticles as recombination centers and as high κ material. Furthermore, transparent OTFTs with low photosensitivity are also presented. The fifth chapter shows OTFTs can have color

filtering function. Color filter inks are first successfully integrated into gate dielectric layer. Moreover, colored polymethyl methacrylate (PMMA) is used to be gate insulator. This unique colored polymer minimizes the phase separation issue and opens a new way for the application of multifunctional organic electronics. The sixth chapter studies the optical and electrical properties of amorphous In-Ga-Zn-O films. Photosensitivity of a-IGZO TFT under illumination with different wavelength is also discussed. The seventh chapter represents the simulation and modeling result of a-IGZO TFTs. Oxygen vacancies are first introduced into density of states. The eighth chapter presents our latest results of ambipolar TFTs and their CMOS-like inverter circuit. We combine pentacene and a-IGZO these two active materials into one device, demonstrates both p type and n type behavior. Furthermore, two ambipolatr TFTs combined together shows CMOS-like inverter characteristic. The ninth chapter gives the conclusion and future work.



Chapter 2

Experimental Methods

2.1 OTFT device fabrication

The top-contact structure was chosen to fabricate the OTFTs in our work because the metal surface was not a suitable environment for the growth of organic materials in bottom-contact structure. In addition, OTFTs with top-contact structure have better performance comparing to bottom-contact structure.

(1) Indium tin oxide electrode patterning

The substrates we used were 100 nm ITO on 1 mm-thick glass. The ITO resistivity is $10 \Omega/\square$. We use photolithography and wet etch process to define the gate electrode pattern. The final schematic structure is shown in Fig. 2-1.

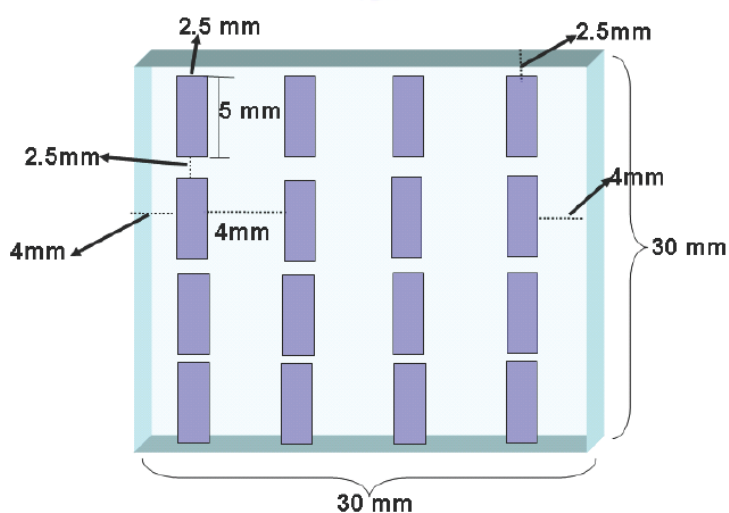


Fig. 2-1 Schematic structure of ITO-patterned-glass

(2) Substrate cleaning

The details sequence is:

Step 1: Clean glasses by detergent

Step 2: Clean glasses by DI water

Step 3: Repeat step 1 and step 2

Step 4: Place the glasses on the Teflon carrier, and put them into a container with acetone. Ultrasonic vibrates 20 minutes to remove organic contamination.

Step 5: Place the glasses into another container with isopropanol (IPA). Ultrasonic vibrate 20 minutes to remove acetone.

Step 6: Use N₂ purge to dry the ITO glasses; place them into a glass container with a cover.

Step 7: Put the glass container into an oven with 100⁰C.

Step 4 and step 5 are illustrated in Fig. 2-2.

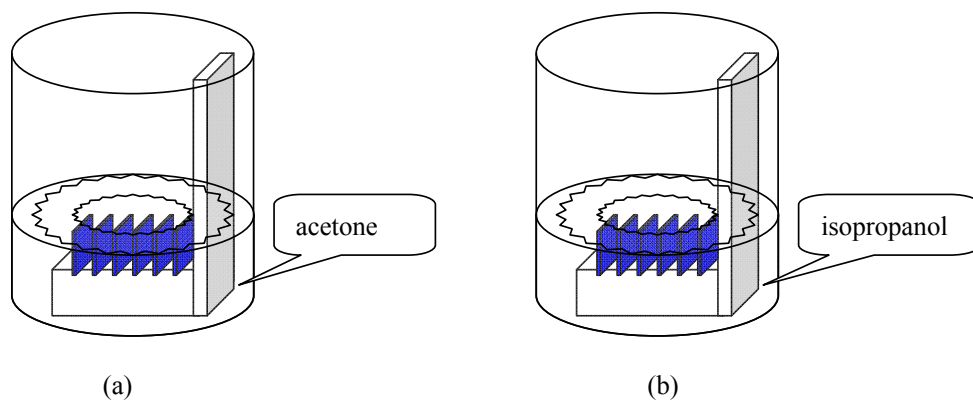


Fig. 2-2 Schematic picture of (a) step 4 and (b) step 5

(3) Gate insulator layers

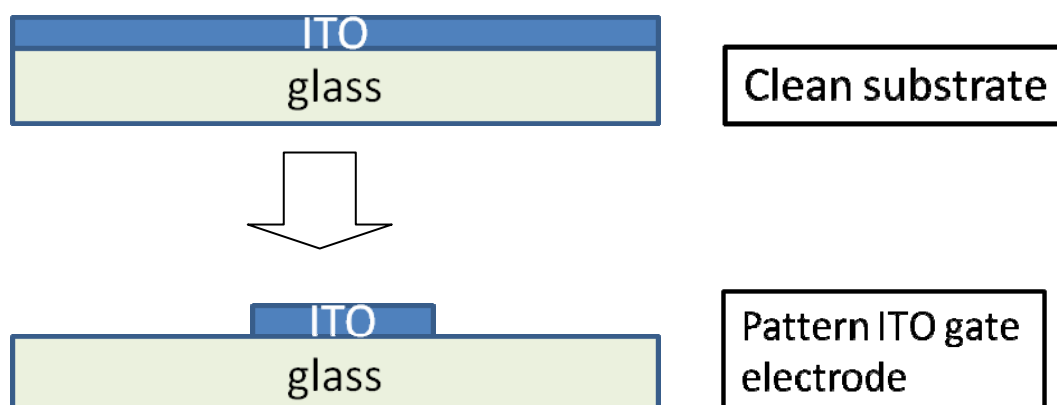
We used different gate insulators in each study. The details will be presented in each section.

(4) Growth of pentacene and electrodes

99.9% pentacene purchased from Fluka without additional purification, was employed as the active layer. It was sublimated by thermal coater under a back pressure below 1.1×10^{-6} torr. The substrate could be heated from 17°C to 90°C , and measured with an Al-Cr thermocouple. As for deposition rate, it was controlled at a rate of $0.5 \text{ \AA}/\text{sec}$ by a quartz oscillator during the thin-film formation. A shutter allowed the stable pentacene flux to pass until the total thickness approached 60 nm. Gold is appropriate for pentacene-based OTFTs as source/drain electrodes due to workfunction matched with pentacene HOMO level. Accordingly, 35-nm-thick Au, as top contacts, was deposited at a rate of $2\sim 3 \text{ \AA}/\text{sec}$ through a shadow mask under 3×10^{-6} torr. As for the transparent devices, the hole injection layer, MoO_2 was deposited at a rate of $0.5 \text{ \AA}/\text{sec}$. ITO was deposited by sputtering at 15 mins under 8×10^{-6} torr. The channel width (W) was $2000 \mu\text{m}$ for all devices in this study, and channel lengths (L) were varied as 75, 100, 130, $160 \mu\text{m}$.

(5) Device processing steps

A typical OTFT processing flow chart is shown below.



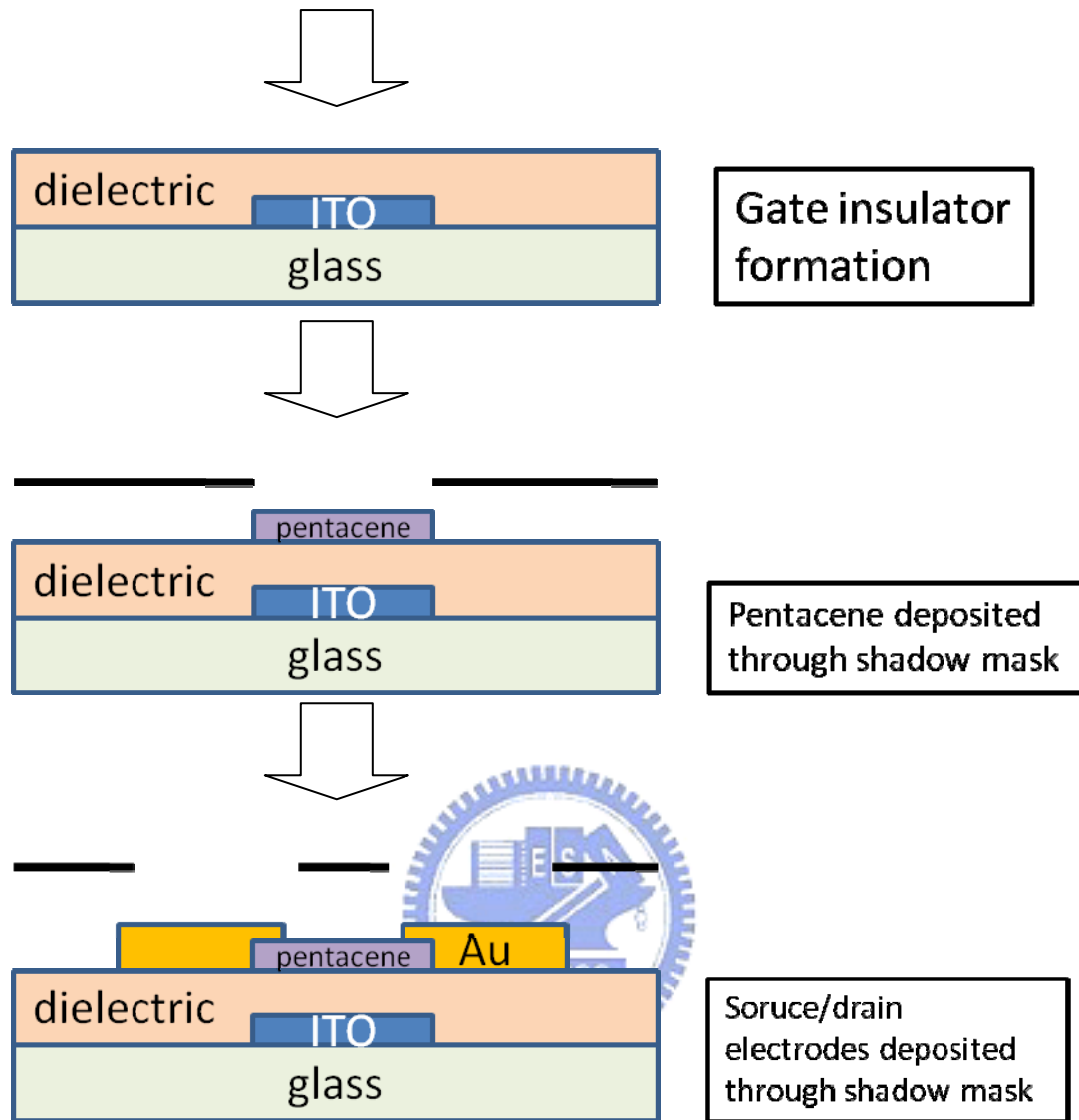


Fig. 2-3 The flow chart of typical OTFT device fabrication

2.2 Electrical Measurement of Devices

The electrical properties of the devices were measured by a Keithley 4200 IV analyzer in a light-isolated probe station at room temperature. For the devices based on pentacene, a negative bias of gate voltage was applied to accumulate holes in the p-channel active layer. In I_{DS} - V_{DS} measurement, the typical drain-to-source bias was swept from 0 to -40 Volts and the gate voltage steps were from $V_{GS} = 0$ V to $V_{GS} = -40$ V. Besides, in I_{DS} - V_{GS} measurement, the gate bias was swept from 20 to -40

Volts and the drain-to-source voltage steps were from $V_{DS} = 0$ V to $V_{DS} = -40$ V.

The capacitances of insulating layer modified with various polymer dielectric materials were measured by HP4284A using metal-insulator-metal (MIM) structure.

2.3 Surface Morphology Measurement

We used a Digital Instruments Dimension 3100 atomic force microscope (AFM) to obtain the surface morphology of the organic semiconducting layers. By the interaction of the van der Waals force between the tip of the cantilever and the surface topology of the sample, the cantilever vibrates at various frequencies depending on the magnitude of the interaction. Detecting a laser beam reflected by the cantilever can sense the tiny vibration of the cantilever.

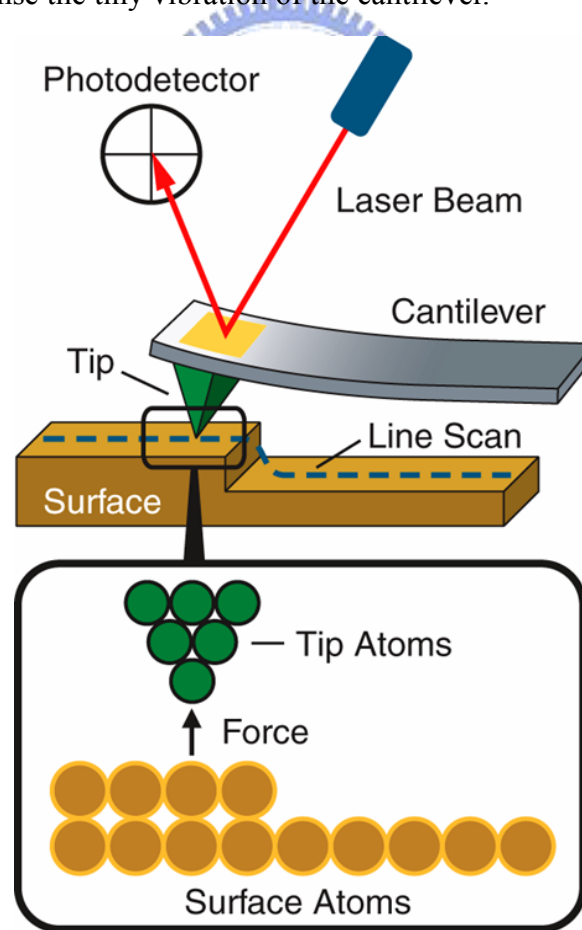


Fig. 2-4 A schematic model of atomic force microscope

The computer record these detected signals and construct the surface morphology of samples. Fig. 2-4 illustrates the configuration of AFM. From the surface morphology, we have clues to recognize the relation between the transfer characteristics and the graining formation of the organic semiconductor. During the scanning of tapping-mode, the probe oscillates up and down regularly. It prevents the probe from damaging the surface of the organic samples and obtains extra topographic information about the samples. The computer records the feedback amplitude and the phase signals of the cantilever. From the amplitude signals we can obtain the morphology information. The phase signals reveals the different materials or arranged formation of the sample.

2.4 Contact Angle Measurement

The contact angle, formed between the liquid/solid interface and the liquid/vapor interface, is defined by the edge of a liquid droplet on the surface of flat sample, which is illustrated in Fig. 2-5 indices s and l stand respectively for “solid” and “liquid”; the symbols σ_s and σ_l denote the surface tension components of the two phases; symbol γ_{sl} represents the interfacial tension between the two phases, and θ stands for the contact angle corresponding to the angle between vectors σ_l and γ_{sl} .

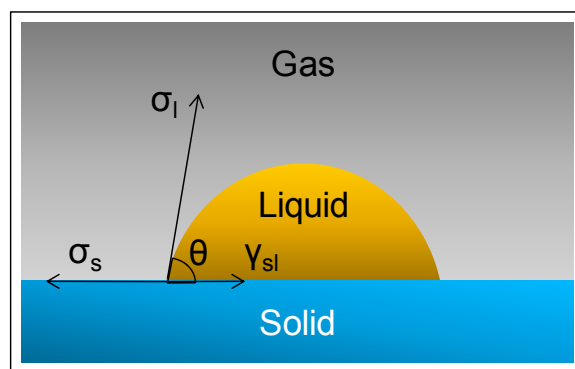
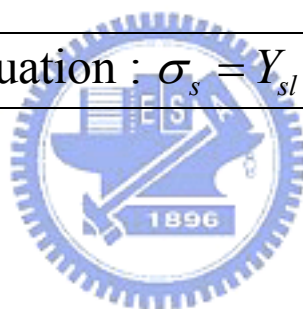


Fig. 2-5 The contact angle formation of liquid on solid surface

The contact angle is specific for any given system and is determined by the interactions across the three interfaces. The concept of static measurement mode is illustrated with a small liquid droplet resting on a flat horizontal solid surface. This method is used to estimate wetting properties of a localized region on a solid surface.

We dropped respectively diiodo-methane, water and ethylen glycol liquids on the SiO₂ surfaces with various modification to measure the contact angle in each case. Furthermore, use Young's equation [16] to calculate the surface energy of different modified insulators. The contact angle measurement and surface energy calculation were finished by Kruss Universal Surface Tester, GH100.

$$\text{Young's equation : } \sigma_s = Y_{sl} + \sigma_l \times \cos \theta$$



2.5 Sputtering

(1) RF sputtering

RF sputtering uses a radio frequency power supply, operating at 13.56 MHz, to generate plasma, which creates ions are used to sputter the target material. The ions are accelerated towards the target by a negative DC bias on the target due to the flux of electrons. The ions hit the target with enough energy to dislodge the target atoms, which are then redeposited onto the substrate. RF sputtering is performed under vacuum, typically between 1 mTorr and 50 mTorr, to improve the quality and the deposition rate of the deposited film. A lower pressure increases the mean free path, the distance between collisions, and results in the deposited species having more energy to diffuse along the substrate surface in order to find the lowest energy state possible. RF sputtering can be used to sputter both insulating and conducting targets,

since charge does not build up on the surface of the target. The major disadvantages of RF sputtering are cost and deposition rate.

(2) DC sputtering

The only major change from RF to direct current (DC) sputtering is the power supply used. In DC sputtering, as the name suggests, a DC power supply is used to create the plasma. The physics of the sputtering process is unchanged. Direct current sputtering allows for higher deposition rates and is less expensive than RF sputtering. Conventional DC sputtering can only be used to sputter conductive targets. The flux of electrons from the DC supply causes charge to build-up on the surface of an insulating target, rendering the plasma unstable so that it eventually extinguishes. One method used to sputter insulating targets using DC sputtering involves the use of a pulsed DC source. When using a pulsed DC source, the voltage is periodically pulsed positive for a very short time to remove the charge on the insulating target. This positive pulse duration is a very small fraction of the entire period, resulting in a higher sputter rate than that of RF sputtering.

(3) Sputter system in NCTU

We have our-own sputtering system in class 10K clean room. Schematic outline is shown in Fig. 2-6. Vacuum system composes of rotation pump and cryo pump, which work for different pressure range. Power system consists of several DC and RF power modules with 6 sputtering guns. Purified gas sources are Ar, N₂, and O₂. There is also an rotation system to get high uniformity by rotating sample disk and sample holders.

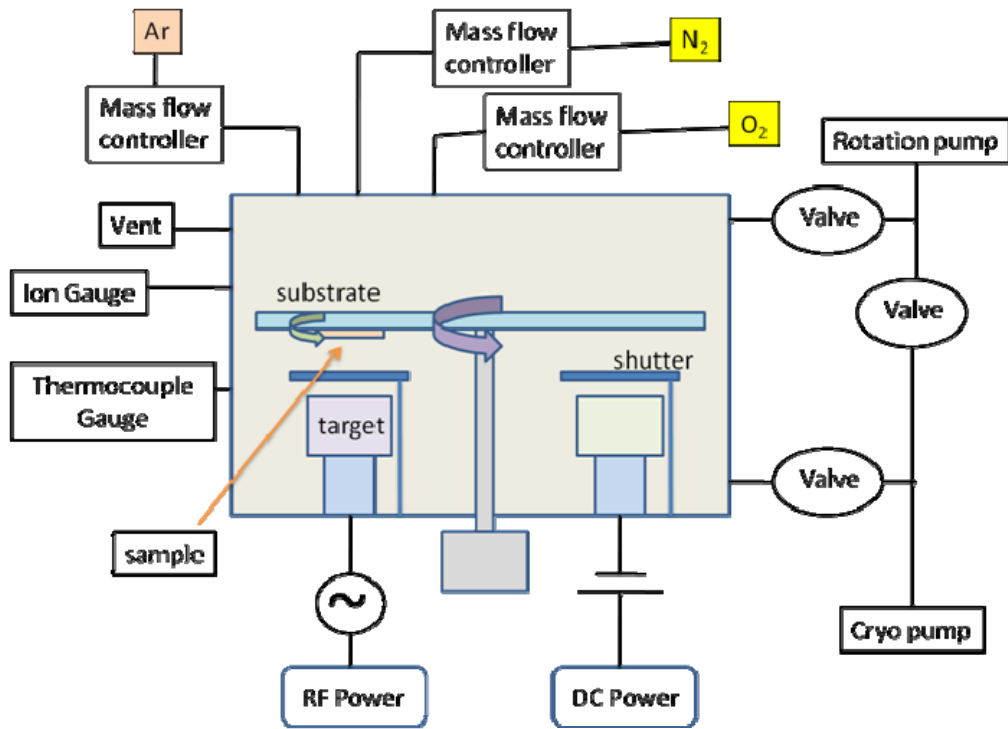


Fig. 2-6 Schematic sputtering system in NCTU



Chapter 3

Organic Thin-film transistors with polymeric nanocomposite dielectrics

3.1 Introduction

Organic thin-film transistors (OTFTs) have been recognized as promising technology for next generation electronics due to their unique advantages, such as light-weight, flexibility, and low-cost fabrication [17-19]. Potential applications include flexible displays [20,21], radiofrequency identification (RFID) tags [22], “smart” cards, and other consumer electronics [23,24]. However, the major challenge to realize the commercialization of related products comes from their high threshold and operating voltages, due to the intrinsic low charge motilities of organic semiconductors. Because the field-induced current is proportional to the field-induced charge density, one feasible approach to achieve low-voltage operation in OTFTs is to use high dielectric constant (high- κ) materials as the gate insulators, which can afford greater surface charge density at the semiconductor-dielectric interface. Several works, especially those adopting inorganic high- κ materials, have demonstrated successfully the reduction of the OTFTs operating voltages using this concept [25,26]. However, these inorganic materials are usually expensive to fabricate and not compatible with plastic substrates due to the high-annealing-temperature processes and their fragility. Using a solution-processable method high- κ polymers can be easily fabricated and used as dielectrics for OTFTs without the complications associated with sputtering high- κ materials and the high-temperature annealing [27]. Nanocomposite materials,

consisting of titanium dioxide (TiO_2) nanoparticles and cross-linked poly-4-vinylphenol (PVP), were dispersed well in organic solvents. Upon spin-coating and thermal annealing, a composite insulator film was obtained. Due to the limited solubility of TiO_2 nanoparticles, the dielectric constant only increased from 3.5 to 5.4 after blending high- κ nanoparticles into the polymer matrix. In this work, surface modified TiO_2 nanoparticles with organosiloxane was used in order to increase the solubility in organic solvents. With the higher content of TiO_2 incorporated, a dielectric constant higher than 11 is achieved. More importantly, we will show that the current leakage problem through the gate dielectrics can be overcome by further applying another thin organic polymer insulator. As a result, we have also demonstrated low-voltage OTFTs, which can operate within 10 V.

3.2 Experiment

Titanium dioxide exists naturally as three possible crystal types, namely, rutile, anatase and brookite [28]. In this study, we employed TiO_2 with rutile structure due to its higher dielectric constant ($\kappa = 114$) than that of other structures. In addition, rutile TiO_2 has much lower photocatalytic activity; possible photoreactions can be avoided. Nanocomposite dielectric layers, consisting of TiO_2 nanoparticles, whose surface was further modified with organosiloxane (Ishihara Sangyo Kaisha LTD., Japan), and cross-linked PVP were prepared for OTFT gate insulators. PVP (11 wt%) and poly (melamine-co-formaldehyde) methylated (4 wt%), as a cross-linking agent, were dissolved in propylene glycol monomethyl ether acetate (PGMEA), [29] and blended with different concentrations of TiO_2 nanoparticles. The composite solution was then spin coated onto indium–tin-oxide (ITO) patterned glass substrates which were used as gate electrodes. The thickness of these insulators is ~ 700 nm.

Pentacene was thermally evaporated as the semiconductor layer. Finally, gold metal was thermally evaporated through the shadow mask and used as the source and drain electrodes (top-contact). The channel length (L) and width (W) are 160 and 2000 μm , respectively. The film thickness and roughness were measured by DI 3100 series atomic force microscopy (AFM). The current–voltage (I–V) characteristics of OTFTs were measured by a HP 4156A semiconductor parameter analyzer. The devices with metal–insulator–metal (MIM) structure, consisting of different dielectric materials sandwiched between ITO and Al electrodes, were used for capacitance measurements. The capacitance measurements were conducted with a HP 4284A Precision LCR meter. The dielectric constants were calculated by eq. (3-1):

$$C = \kappa\epsilon_0 A/t$$

eq. (3-1)

where C is the measured capacitance, ϵ_0 is the permittivity of free space, A is the area of the capacitor, and t is the thickness of the dielectric.

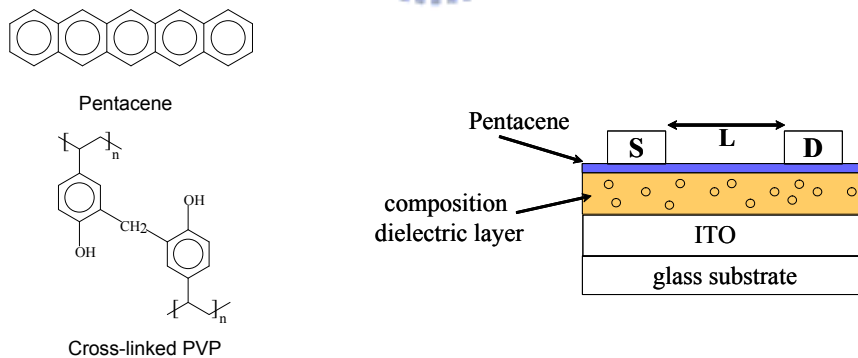
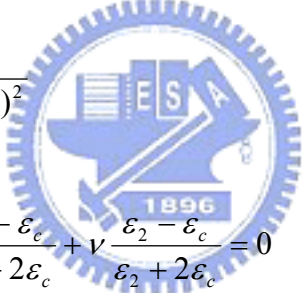


Fig. 3-1 Chemical structures of the pentacene and cross-linked PVP; device structure of the OTFT

3.3 Result and Discussion

For a pure cross-linked PVP film, the dielectric constant is 4.3 at 1 kHz, which close to the value reported earlier [27,30]. From Table 3-1, we can see that the dielectric constant increases with the amount of the TiO₂ nanoparticle embedded in the thin films. For the dielectric film with 15 wt% of TiO₂ nanoparticle, the dielectric constant increased to 10.8, due to the higher solubility of the organosiloxane surface modified TiO₂ fillers, compared to that reported earlier [27].

Several theoretical models have been investigated to predict the dielectric constant of the nanocomposite [31,32]:



Model A $\varepsilon_c = \frac{\varepsilon_1}{(1-\nu)^2}$ (Bruggeman)

Model B $(1-\nu)\frac{\varepsilon_1 - \varepsilon_c}{\varepsilon_1 + 2\varepsilon_c} + \nu\frac{\varepsilon_2 - \varepsilon_c}{\varepsilon_2 + 2\varepsilon_c} = 0$ (EMT)

Model C $\log \varepsilon_c = (1-\nu)\log \varepsilon_1 + \nu\log \varepsilon_2$ (Log Law)

Model D $\varepsilon_c = \varepsilon_1 \left[1 + 3\nu \left(\frac{\varepsilon_2 - \varepsilon_1}{2\varepsilon_1 + \varepsilon_2} \right) \right]$ (Rayleigh)

where ε_c , ε_1 and ε_2 are the composite, base and filler dielectric constant, respectively, and ν is the filler volume percentage. Compared the modeling results with the experimental data, as shown in Fig. 3-2, the Model B, called Effective Medium Theory (EMT), which considers the average permittivity around the fillers

expanding from Bruggeman's theory, can better and accurately predict the dielectric constant of the nano-composite.

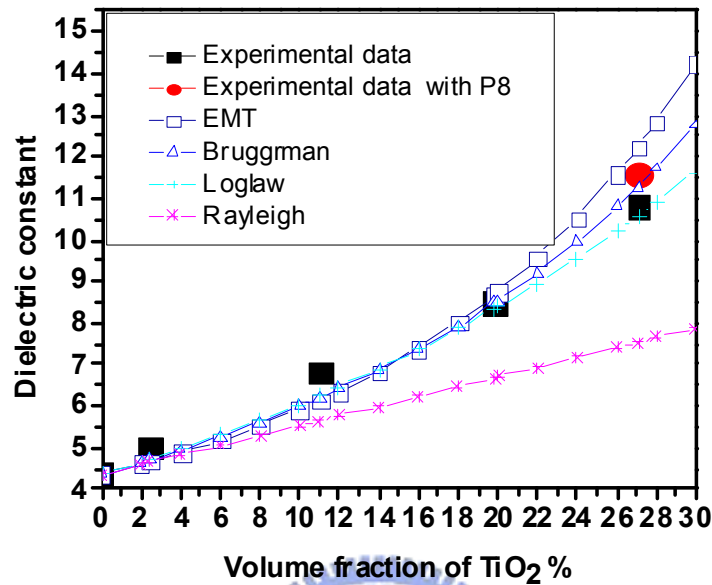


Fig. 3-2 Calculated and experimental dielectric constants

Table 3-1 Electrical parameters of the OTFTs in this study.

TiO ₂ wt%	TiO ₂ volume fraction	Dielectric constant	μ_{sat} (cm ² /Vs)	V _t (V)	Surface roughness (nm)	On/Off ratio
			160um+/-5%			
0%	0	4.3	0.42	-5.2	0.30	5 x 10 ⁴
1%	2.41	4.8	0.39	-14.4	9.76	4 x 10 ⁴
5%	11.01	6.7	0.42	-10.9	16.19	9 x 10 ³
10%	19.84	8.5	0.34	-3.3	26.99	6 x 10 ³
15%	27.07	10.8	0.32	+5.9	31.43	1 x 10 ³
15% / PαMS	27.07	11.6	0.41	-3.0	13.30	3 x 10 ⁴

From the experimental data, the dielectric constant of PVP film blended with 15%wt TiO₂ was smaller than that of the film further modified with PαMS. It is suspected that the higher leakage current, resulted from the blending of nanoparticles, reduces the effective dielectric behavior of the dielectrics. After

PαMS treatment, the value of dielectric constant ($\kappa=11.7$) is closer to the value predicted from EMT model ($\kappa=12.2$). It is also found that at high filler volume regions, the dielectric constant increases exponentially with filler volume. Based on our calculation, it is anticipated that this method is promising for increasing the dielectric constant of organic insulators as long as we can load more fillers into the matrix.

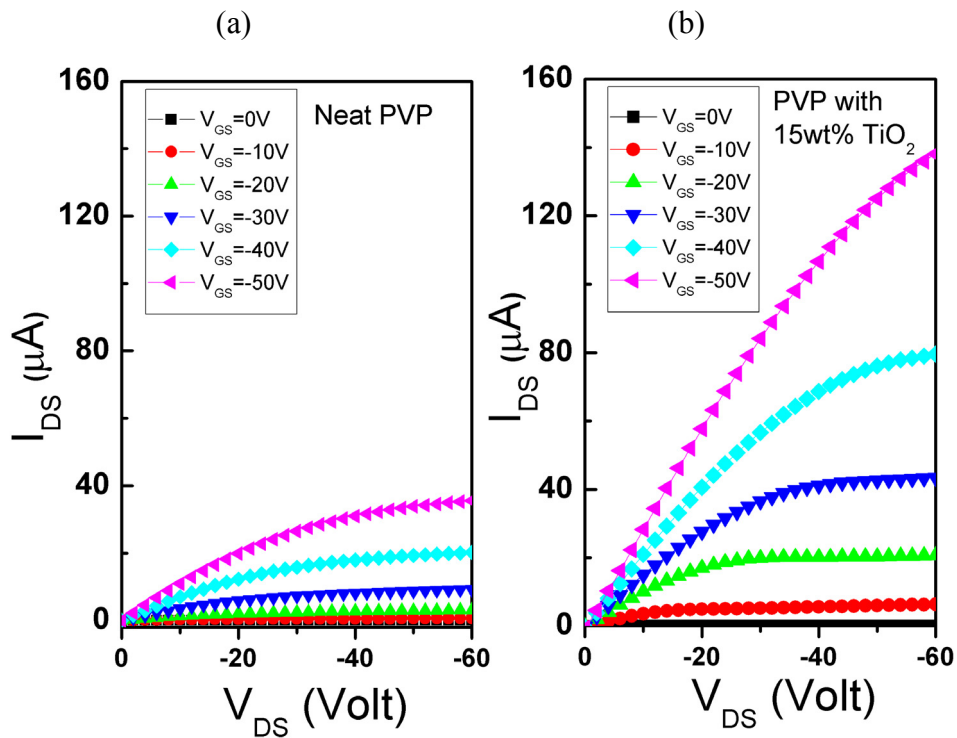


Fig. 3-3 The output characteristics of OTFTs with (a) a neat PVP insulator (b) a composite insulator with 15 wt% TiO₂

The drain–source current (I_{DS}) vs. drain–source voltage (V_{DS}) of OTFTs with different TiO₂ concentrations incorporated in the gate insulators is shown in Fig. 3-3. The carrier mobility was calculated in the saturation regime using the following equation:

$$I_{DS} = (WC_i/2L)\mu(V_G - V_{TH})^2 \quad \text{eq. (3-2)}$$

where C_i is the capacitance per unit area of the insulator, and V_{TH} is the threshold

voltage. For the device with a neat PVP gate insulator, (Fig. 3-3(a)) the mobility in the saturation region and the threshold voltage of the OTFT are $0.42 \text{ cm}^2 \text{ V}^{-1} \text{ s}^{-1}$ and -5.2 V , respectively. The on-off ratio is more than 10^4 . With 15 wt% of TiO_2 nanoparticles blended into the dielectric layer, (Fig. 3-3(b)) the device exhibits more than triplet the field-induced current compared with that of the device using the pure PVP insulator which is attributed to the higher surface capacitance. Fig. 3-3 reveals that the drain-source current increased by increasing the content of TiO_2 nanoparticles in the gate insulators. The parameters of the dielectric materials as well as the corresponding electrical characteristics of the OTFTs with different amount of TiO_2 nanoparticles embedded in the gate insulators are summarized in Table 3-1. On the other hand, we also observe that the threshold voltage (V_{TH}) decreases and then increases when more nanoparticles were added (Table 3-1). From the surface morphology study by AFM, the insulator roughness increased with the increasing concentration of TiO_2 blended. Consequently, the shift of V_{TH} to higher values may be the result of the insulators surface roughness. The interface between the organic semiconductor and the insulator is affected by the incorporation of TiO_2 nanoparticles. Additionally, we can also find that the on/off ratio decreases while the concentration of TiO_2 increases (Table 3-1). Fig. 3-4 shows clearly that the device with 15 wt% TiO_2 has much higher leakage current than that with 1 wt% nanoparticles. The leakage problem is probably due to the low-band gap of TiO_2 . In addition, structure defects induced by the present of high concentration TiO_2 might also result in the higher leakage current, which has been confirmed from the fact that the surface roughness of the insulators increased with the content of nanoparticles (Table 3-1). In order to rectify this problem, the insulator layer was covered with a poly(α -methylstyrene) (P α MS) layer. Due to the robustness of cross-linked polymers, the underlayer was not affected by this process. As shown in Fig. 3-4, the

device off current is dramatically suppressed after spin-coating ~ 3 nm P α MS on the nanoparticle/cross-linked PVP insulator. The over-coating of another interfacial layer can reduce the concentration of surface defects of the dielectrics and smooth the dielectric surface. In addition the dielectric constant of the insulator modified with P α MS is higher than that without modification. This further supports the fact that P α MS can inhibit the leakage current and enhance the dielectric strength of the composite polymer. On the other hand, the smooth dielectric surface might also induce the formation of a more orderly crystalline pentacene film, and subsequently, increase the device mobility as shown in Table 3-1.

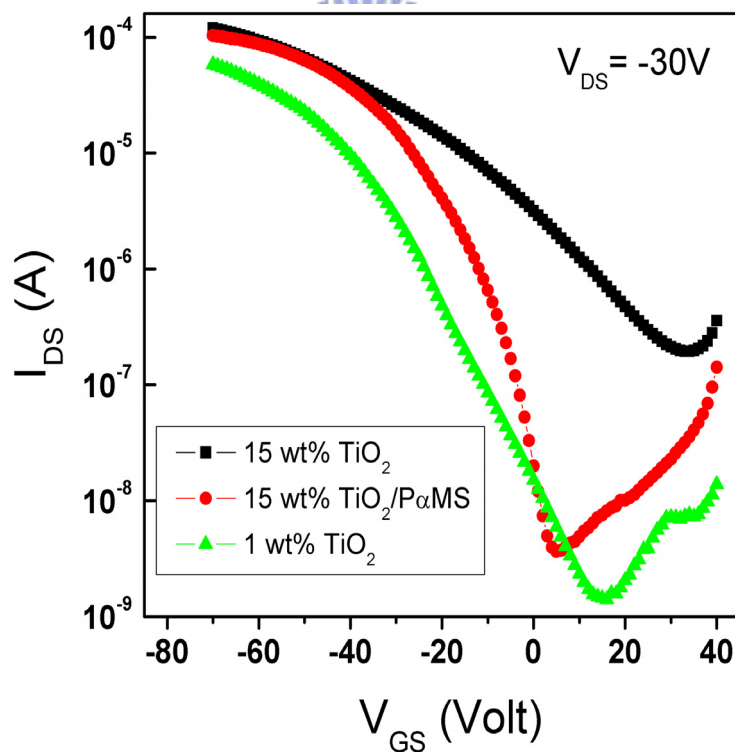


Fig. 3-4 The transfer characteristic at constant $V_{DS} = -30V$ for OTFTs with 1wt%, 15wt% of TiO_2 nanocomposite insulators, and nanocomposite insulator with P α MS interfacial layer

Table 3-1 apparently shows that the surface roughness of the dielectric layer affects the device mobility in the saturation regime. While the concentration of TiO_2 is more than 5 wt%, the mobility drops dramatically. The rough dielectric surface probably interferes with the formation of an ordered crystal structure. Fig. 3-5 shows the surface morphology of pentacene deposited on different dielectrics. In contrast to the clear crystal formation on the neat crosslinked PVP, the grain size of pentacene on the 15 wt% TiO_2 filled-PVP film is rather small. The higher concentration of grain boundary might limit the charge transport in the organic films. However, after over-coating the P α MS layer, typical lamella morphology appears again, which implies the formation of an ordered crystal structure.

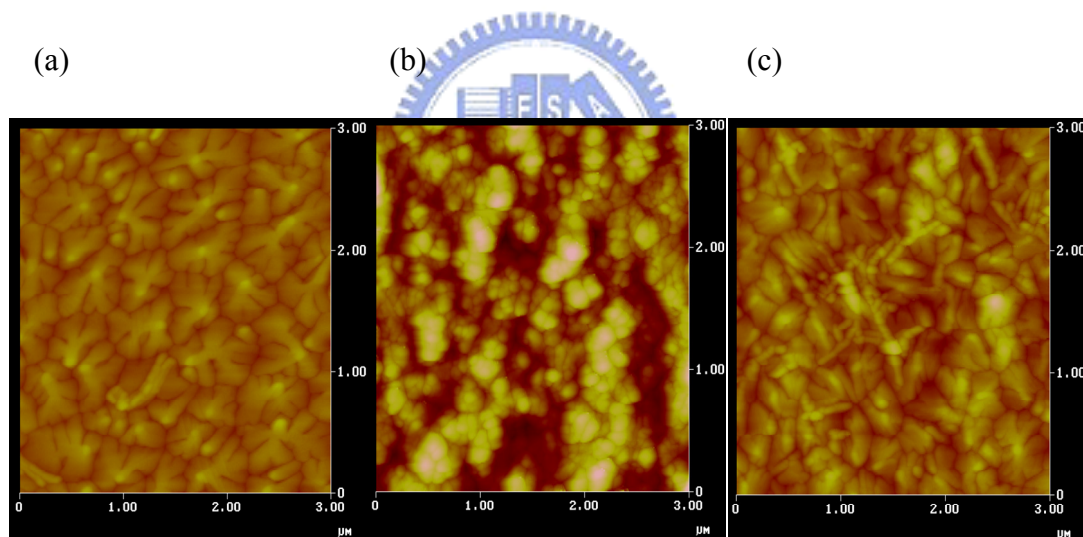


Fig. 3-5 AFM height-mode images of pentacene deposited on the surface of (a) neat cross-linked PVP; (b) cross-linked PVP blended with 15 wt% TiO_2 nanoparticles; (c) cross-linked PVP blended with 15 wt% TiO_2 nanoparticles and further modification with P α MS interfacial layer.

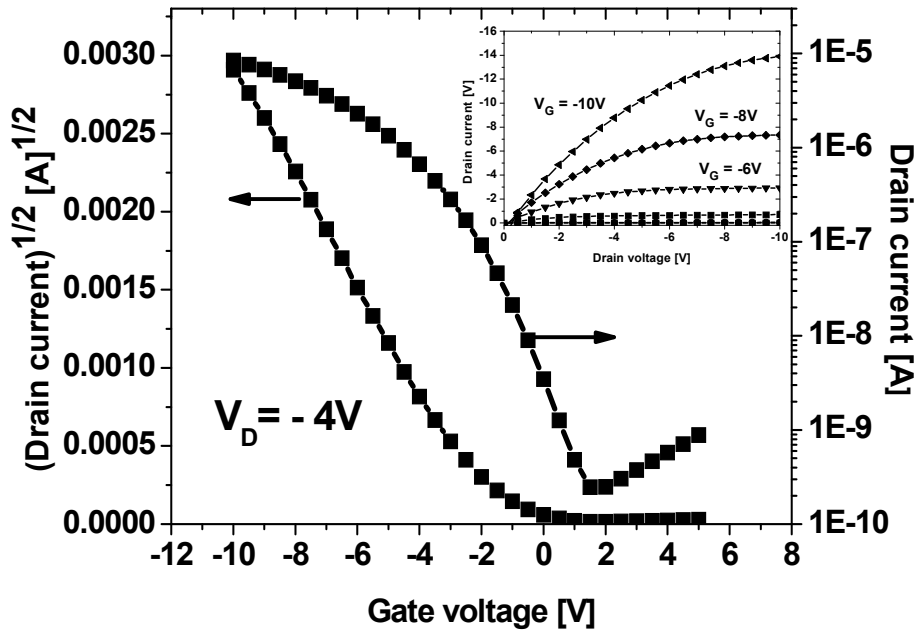


Fig. 3-6 The transfer characteristics of the OTFT with a thinner gate insulator. The inset shows the corresponding output characteristic from $V_{GS} = 0$ V to -10 V

In summary, the P α MS layer not only suppresses the leakage current by reducing the concentration of defects in the dielectric layer, but also induces pentacene to form a more ordered molecular conformation thus maintaining the high mobility in the conducting channel. Since the leakage problem has been overcome by incorporating an interfacial layer, thinner dielectric layers will be allowed to achieve a greater capacitance value. Fig. 3-6 shows the output characteristics for an OTFT with a 270 nm nanocomposite insulator, consisting of one layer of 15 wt% TiO₂ filled PVP film and another thin P α MS. The dielectric constant of this composite is 10.5, which is slightly lower than that of previous one. The device exhibits mobility of ~ 0.4 cm² /Vs. The subthreshold swing is 1.0 V/decade and the threshold voltage is -2.9 V. The on-off ratio is more than 3.0×10^4 . From Fig. 3-6, it is apparent that low-voltage OTFTs can be fabricated by using nanocomposite dielectric polymers

with simple and solution-processable processes.

We also tried to make the devices onto flexible PET substrate. The device structure was same as pure PVP gate insulator device (700 nm PVP gate insulator). Due to the limitation temperature of PET substrate, we changed the PVP curing condition from 200⁰C, 20 min to 100⁰C, 12 hour. Fig. 3-7 shows the bendable devices and output curves. The averaged mobility was around 0.1 cm²/Vs. The flexible organic TFTs were demonstrated by using polymer-based gate insulators.

3.4 Conclusion

In conclusion, high performance organic thin-film transistors incorporated with high dielectric nanoparticles in the dielectric layers have been demonstrated successfully. Moreover, the problem of leakage current of OTFTs, while using the nanocomposite insulators, has been overcome using over-coat of another thin interfacial layer. This method offers a feasible and economic way to deposit gate insulators for OTFTs with high capacitance without the complications associated with sputtering of high dielectric materials and high temperature annealing. Finally, one low-voltage OTFT, which can operate within 10 V, has also been achieved by this method.

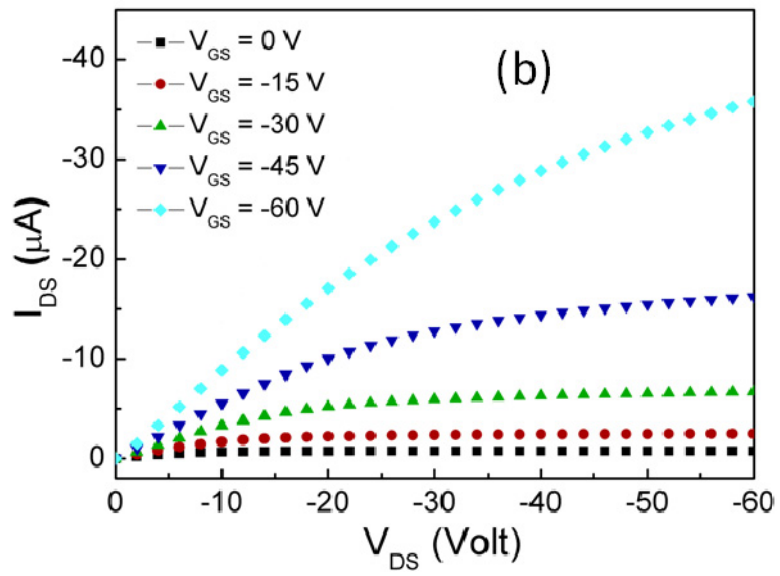
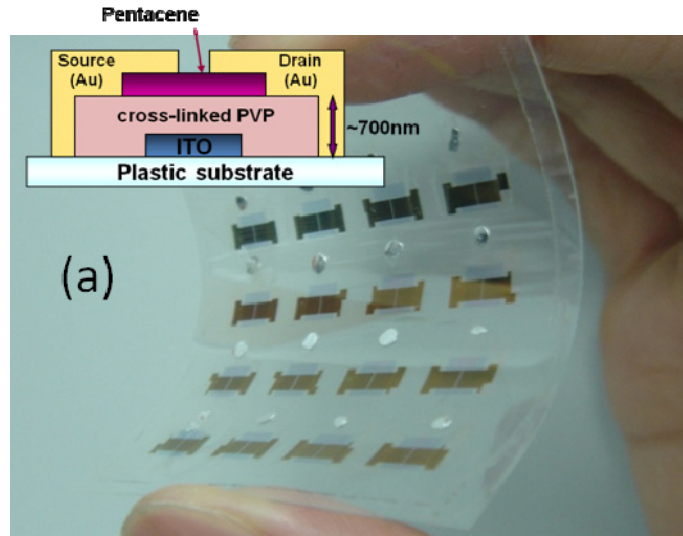


Fig. 3-7 (a) Device structure and bending view of flexible OTFTs. (b) Output characteristics (I_{DS} - V_{DS}) of the flexible OTFT.

Chapter 4

Organic thin-film transistors with reduced photosensitivity

4.1 Part. A Organic thin-film transistors with reduced photosensitivity

4.1.1 Introduction

Currently, there is increased interest in thin-film transistors made of organic materials due to their great potential applications in low-cost and flexible electronics, such as smart cards, radio-frequency identification (RFID) tags and paper-like displays [17,33- 37]. A level of performance by organic thin film transistors (OTFTs) comparable to that of amorphous silicon (a-Si) has been achieved. For example, a field-effect mobility higher than $1 \text{ cm}^2/\text{Vs}$ and with several orders of on–off ratio has been demonstrated for OTFTs based on pentacene. While the intrinsic properties of organic semiconductors and the device physics of OTFTs have been studied extensively, their reliability and photoresponse levels have not received much attention until recently [38- 43]. Moreover, methods to lower photosensitivity and to improve device stability have received considerably less attention. On the other hand, the photosensitivity of OTFTs is a critical issue for driving applications in displays, such as liquid–crystal displays (LCDs) [43]. For instance, pentacene has high level of photo absorption in the visible range, which is due to its high oscillator strength and low energy between its highest occupied molecular orbital (HOMO) and its lowest unoccupied molecular orbital (LUMO): around 2.3 eV. Therefore,

light from backlight modules may pass through the OTFTs and cause a serious threshold voltage (V_{TH}) shift [43]. As a result, OTFTs usually cannot be turned off effectively when the gate bias is set at zero under illumination [42,43]. In this work, one method to reduce photosensitivity and to enhance device stability has been reported. To put it simply, by blending the polymer dielectrics with titanium dioxide (TiO_2) nanoparticles, the V_{TH} shift is minimized and the output current becomes more stable under white light illumination. This improvement can be attributed to the recombination centers induced by the TiO_2 nanoparticles. Moreover, by reducing the photosensitivity, the pentacene-based OTFTs have the potential to drive the circuits without a noticeable V_{TH} shift and with no light shield. Finally, the device reported in this work will greatly facilitate the making of more reliable transparent organic electronics: an area which has received much attention recently [44,45].

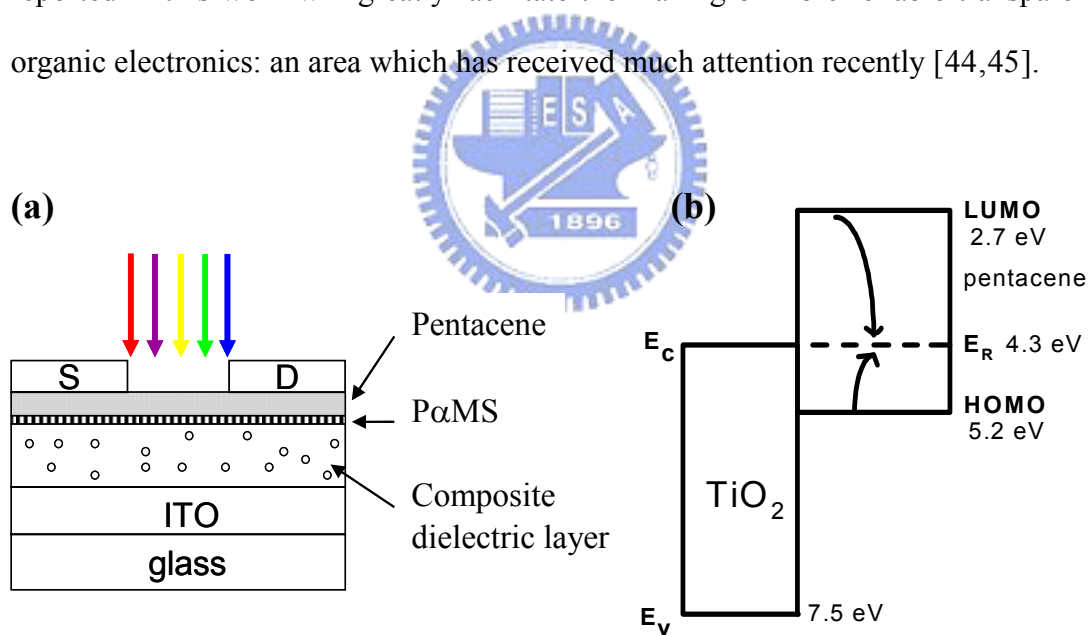


Fig. 4-1 (a) The device structure of the OTFTs in this study. (b) Energy band diagram of pentacene and TiO_2

4.1.2 Experiment

Titanium oxide with a rutile structure ($\kappa = 114$) was used as the high-dielectric component in the nanocomposite dielectrics [27,46]. The device structure is shown in Fig. 5-1(a). Poly-4-vinylphenol (PVP) and poly(melamine-co-formaldehyde) methylated were dissolved in propylene glycol monomethyl ether acetate (PGMEA), blended with TiO_2 nanoparticles, whose surface was further modified with organosiloxane to enhance their solubility (Ishihara Sangyo Kaisha LTD., Japan) [46]. The solution was then spin-coated onto the indium–tin-oxide (ITO) patterned glass substrates and ITO was used as the gate electrodes. The resulting film was further thermally annealed to 200 °C. Then, the thermally evaporated pentacene was used as the semiconducting layer for the OTFTs. Next, gold was thermally evaporated as the source and drain electrodes. The channel length (L) and width (W) of the devices were 100 and 2000 μm , respectively. To suppress the degradation of the on–off ratio after adding the nanoparticles, the insulator was further overcoated with a very thin-layer of poly(a-methylstyrene) (P α MS) by spin-coating from a diluted toluene solution (0.1 wt%). Due to the robustness of the cross-linked polymers, the underlayer was not affected by this process [46]. The film thickness and roughness were measured using a DI 3100 series atomic force microscope (AFM). The current–voltage (I–V) characteristics of the OTFTs were measured with a HP 4156A semiconductor parameter analyzer. The illumination light source was a standard Hg lamp. All measurements were performed under the atmosphere.

4.1.3 Result and Discussion

The transfer characteristics of the devices before and after the modification of the

P α MS are shown in Fig. 4-3(a). The extracted mobility of the PVP device following the conventional field effect transistor model is 0.1 cm² /V s. The threshold voltage (V_{TH}) and subthreshold swing (S) are 0.5 V and 2.9 V/ decade, respectively. Initially, the on/off ratio was about 1.0 x 10⁴, but after the addition of a thin layer of the low- κ material, P α MS, the S became smaller, the on/off ratio was improved by one order; while the mobility was almost unchanged. The controllable V_{TH} and turn-on voltages (V_{TO}) in pentacene TFTs have been demonstrated by using different organosilanes with various functional groups as the self-assembled monolayers (SAMs) on the SiO₂ insulators [47,48]. To quantify the device characteristics, the V_{TO} is defined as the gate voltage at which the drain current starts to increase exponentially; while the transistor is in a flat-band position [48,49]. The built-in electric field resulting from the polar SAM molecules induces mobile charges which alters the threshold voltage [49].

Table 4-1 Water contact angle of different surface

Insulator	Modified material	Water angle
SiO ₂	P α MS	86.7
SiO ₂	PMMA	73.2
SiO ₂	PVP	69
SiN	P α MS	84.6
SiN	PMMA	74.5
SiN	PVP	70
PVP	P α MS	83.7
PVP+1wt% TiO ₂	P α MS	85.9
PVP+1wt% ZrO ₂	P α MS	84.8
PVP+15wt% TiO ₂	P α MS	90.5

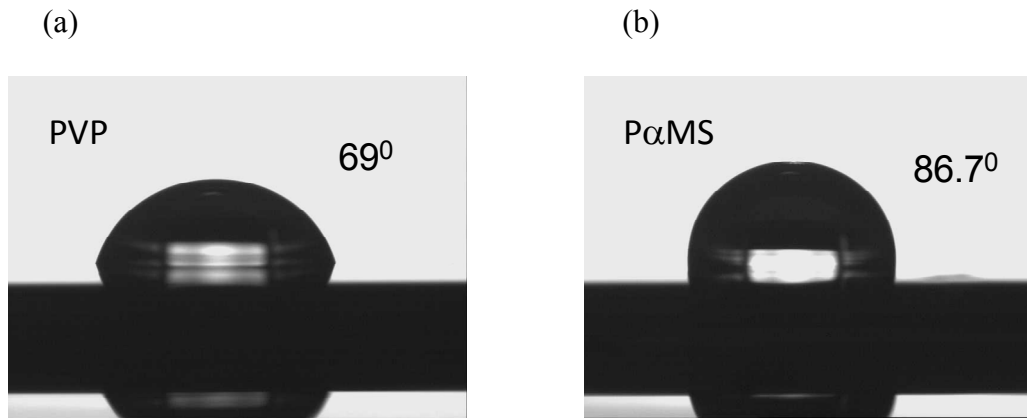


Fig. 4-2 (a) Water contact angle of PVP; (b) P α MS

In this study, the water contact angle on the cross-linked PVP surface is 69.0° , while the angle on P α MS is 83.7° (Table 4-1 and Fig. 4-2). This indicates that cross-linked PVP is much more polar than P α MS. Similarly, the high polarity of cross-linked PVP, which is attributable to its hydroxyl groups, may also explain the high surface polarization which causes the higher mobile charge density. Consequently, as shown in Fig. 4-3(a), the V_{TH} and V_{TO} are more positive when compared with those of devices with a P α MS thin-film. Such phenomena suggest the presence of a dipole field at the pentacene/dielectrics interface [48]. However, after applying a low- κ P α MS onto the PVP, the V_{TO} shifts from 7.5 V to 2.5 V. This change implies a lower free charge density at the interface. The non-polar properties of P α MS prevent surface polarization, thereby reducing the charge density in the conducting channel at $V_{GS} = 0$ V. While the device was under white illumination (10 mW/cm^2), the V_{TH} and V_{TO} of both the devices shifted toward the positive direction, the off-current became stronger (Fig. 4-3(a)). In addition, the S also increased. It has been suggested that the photo-generated electron-hole pairs increase the off-state current dramatically [42,43]. However, while the holes can flow out through the drain electrode under the electrical field, the electrons may be trapped at the grain

boundaries of the pentacene, and/or the insulator/pentacene interface, resulting in a positive shift in the V_{TH} [42,43].

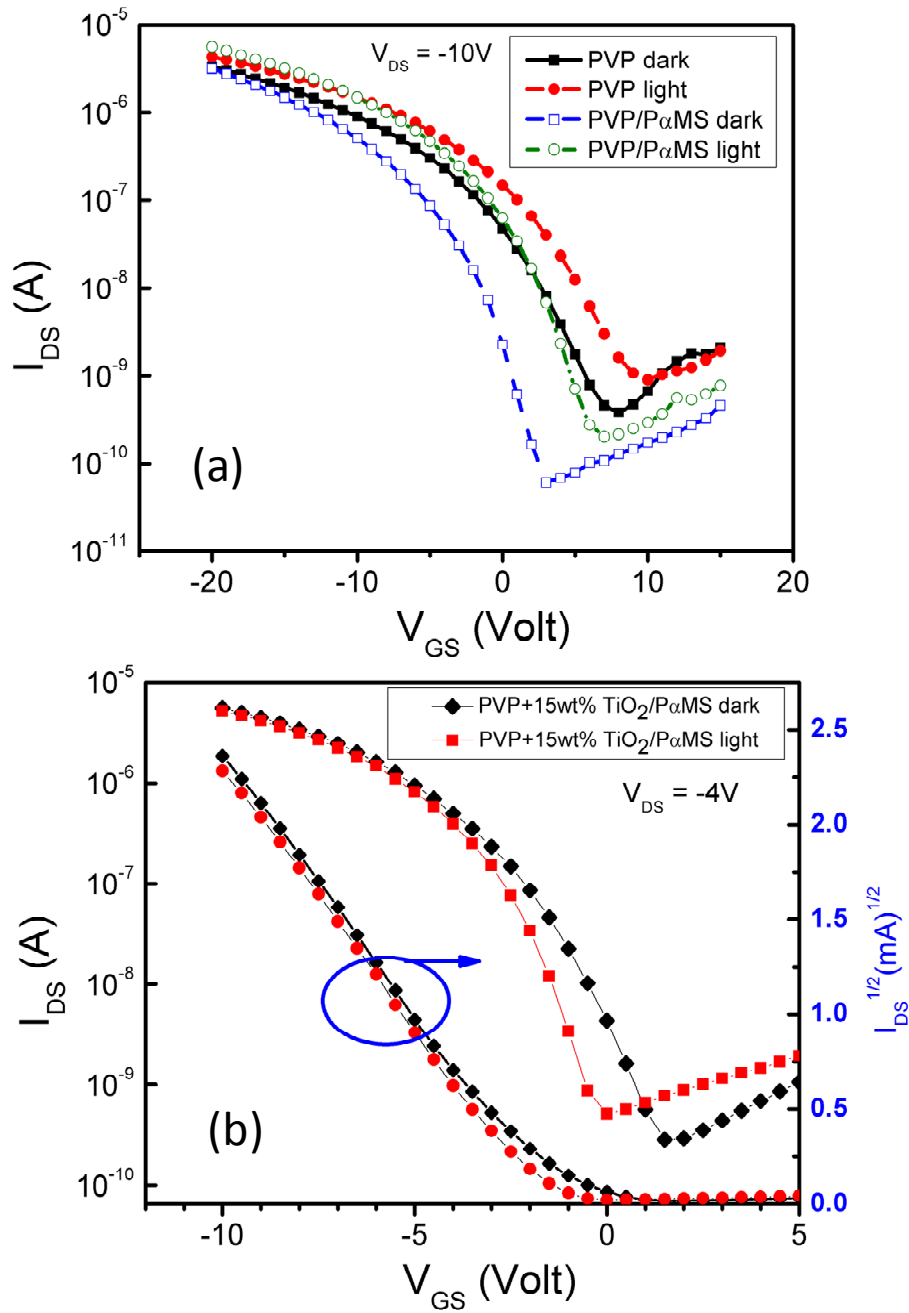


Fig. 4-3 Transfer curves for devices in the dark and under illumination (10mW) with (a) cross-linked PVP and cross-linked PVP/P α MS double layers as the dielectric insulators and (b) PVP + 15 wt% TiO₂ as the gate insulator.

A change in the behavior of the devices was observed upon blending the TiO₂ nanoparticles into the gate dielectrics. Fig. 4-3(b) shows the transfer characteristics of the device in the dark and under illumination. In the dark, the V_{TH} becomes lower because of the use of an insulator with a higher dielectric constant. While the S also decreases to about 1 V/decade. Such phenomena are quite consistent with previous reports on OTFTs with adopted high-κ insulators [36]. Upon illumination, instead of a positive shift, the V_{TO} comes closer to 0 V, the S becomes even better. The changes of the V_{TH} and S are exactly opposite to those of the devices with PVP and PVP/PαMS (Fig. 4-3(a)) as the gate dielectrics. The electric parameters of the devices have been summarized in Table 4-2.

Table 4-2 *Electrical parameters in this study*

Device	Mobility (cm ² /Vs)	Dielectric constant	Insulator thickness	C _i (nF/cm ²)	V _t (V)	S.S. (V/decade)	Interface state density	on/off ratio
PVP dark	0.1	4.3	290nm	13.1	0.51	2.85	3.86*10 ¹²	9*10 ³
PVP light	0.1	4.3	290nm	13.1	4.5	3.19	4.33*10 ¹²	4*10 ³
PVP/PαMS dark	0.13	4.2	290nm	12.8	-4.34	1.76	2.30*10 ¹²	8*10 ⁴
PVP/PαMS light	0.14	4.2	290nm	12.8	0.23	2.13	2.80*10 ¹²	5*10 ⁴
PVP/15wt%TiO ₂ /P8 dark	0.4	10.5	270nm	34.1	-2.83	1.09	3.71*10 ¹²	5*10 ⁴
PVP/15wt%TiO ₂ /P8 light	0.4	10.5	270nm	34.1	-2.89	0.85	2.85*10 ¹²	2*10 ⁴

To explain the different behaviors of the devices represented in Fig. 4-3, several experiments have been conducted which attempt to identify the possible mechanisms involved. First, from the surface morphology analysis using an AFM, it has been shown that the morphology of pentacene is quite similar on the surfaces of both the neat cross-linked PVP and the nanocomposite with the thin PαMS film (Fig. 4-4) [46]. Furthermore, the X-ray diffraction patterns of the pentacene deposited on the neat crosslinked PVP, the PαMS, the nanocomposite with additional PαMS, all

reflect the so-called “thin film” phase structure (Fig. 4-5) [50].

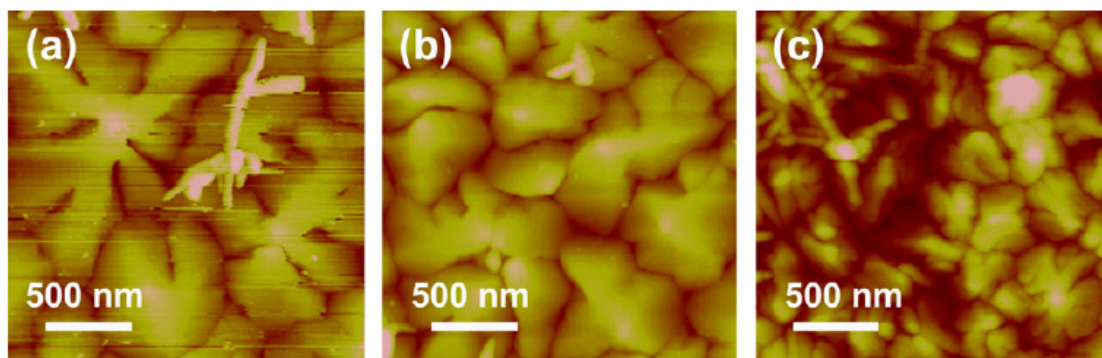


Fig. 4-4 AFM images of pentacene on (a) cross-linked PVP, (b) P α MS/cross-linked PVP and (c) P α MS/TiO₂ nanoparticles + cross-linked PVP

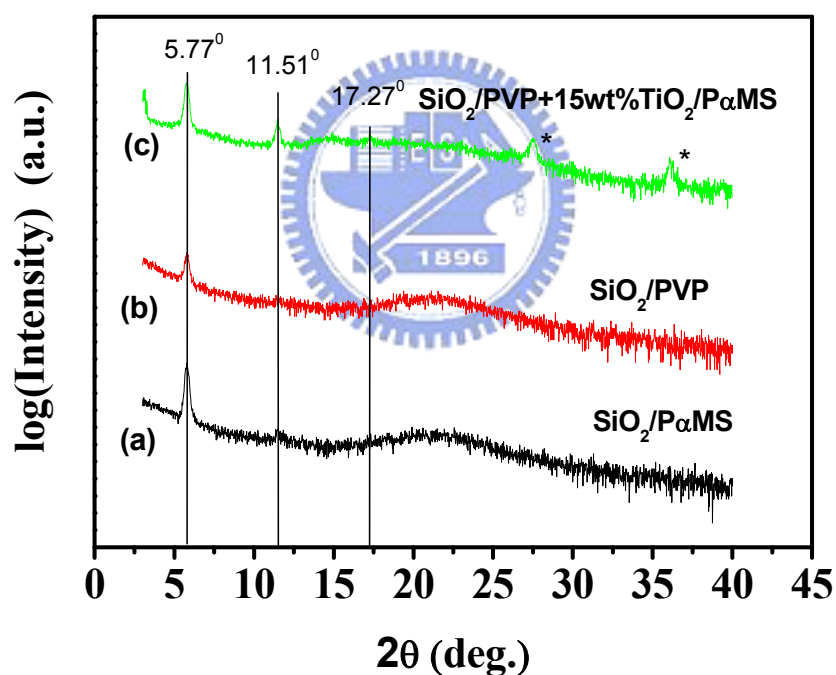


Fig. 4-5 The x-ray diffraction pattern of pentacene deposited on Si/SiO₂ substrates modified with (a) P α MS; (b) cross-linked PVP; (c) cross-linked PVP blended with 15 wt% TiO₂ nanoparticles and further modification with P α MS. The peaks marked with asterisks are due to the structure of TiO₂ nanoparticles.

Consequently, the morphology change is not likely to be the mechanism which

causes the different device behaviors upon blending the nanoparticles. The above mentioned observation is also probably due to the processes occurring at the ITO–insulator interface. In order to determine whether the effect is due to the interface, heavy n-type doped Si and SiO₂ were used in the devices as the gate electrode and the dielectrics, respectively (Fig. 4-6).

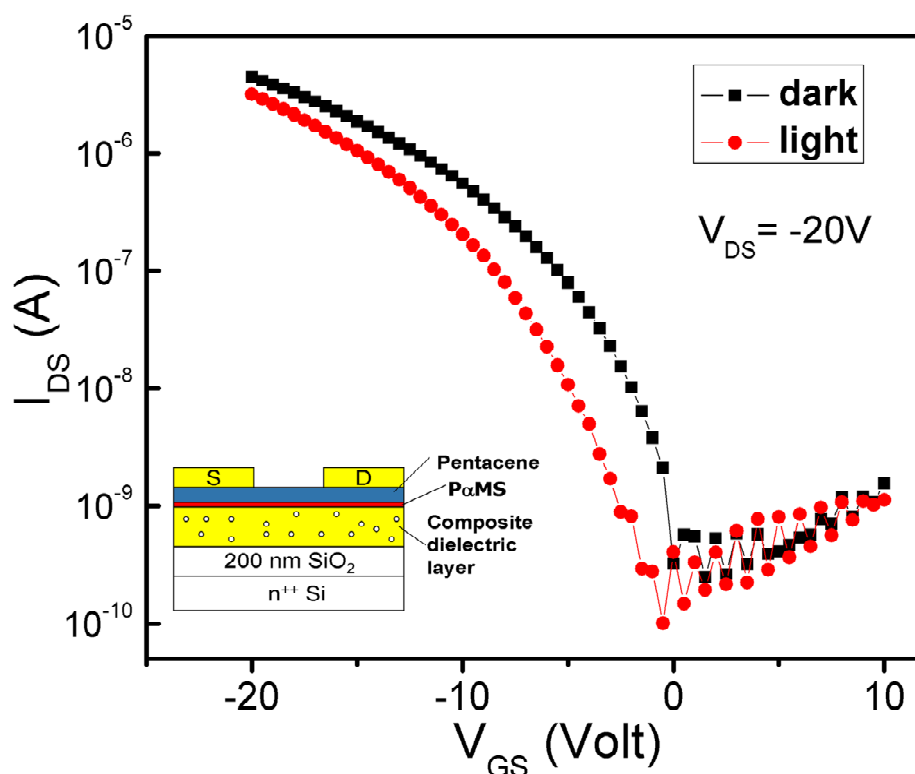


Fig. 4-6 Transfer characteristics of the device with n-doped Si/SiO₂ as the substrate in the dark and under illumination (10mW). The inset shows the device structure.

The SiO₂ surface was further modified with a nanocomposite (15 wt% TiO₂ in PVP)/P α MS bi-layer. However, the device with TiO₂ exhibited similar behavior (that is, a negligible V_{TH} shift), which implies that the mechanism is not relevant to the different processes of the gate electrodes. On the other hand, the present of TiO₂ nanoparticles in the gate insulator seems essential to minimize the effect of white

illumination for the device. The results strongly indicate that the blending of TiO₂ nanoparticles is an important part of the mechanism. The present of TiO₂ nanoparticles probably induces the recombination of the centers in the channel. As seen in Fig. 4-1(b), because of the conduction band of TiO₂ and/or the energy levels induced locate between the HOMO and LUMO of the pentacene, they may behave like recombination centers; thereby releasing the trapped electrons. Consequently, upon illumination, the excess electrons can be eliminated more easily and the V_{TH} shift is suppressed. Stress tests on the three different devices were also performed to further understand the effects of the TiO₂ nanoparticles. The typical stress-test results of the devices, both in the dark and under illumination, used in this study are shown in Fig. 4-7. For the device with a neat cross-linked PVP as an insulator, the field-induced current and/or photocurrent increased steadily over time. This result was consistent with the previous report [39,43]. It has already been indicated that the absorption of water molecules in cross-linked PVP enhances surface polarization, thus the accumulation of extra charges increases the current and results in a positive shift of V_{TH} [39]. However, after modification with PαMS, the current increased initially, but then, decreased with time. Since PαMS is non-polar, the surface polarization probably was found to be inhibited. In addition, it was also found that the hydrophobic PαMS may also retard water absorption. Consequently, after the initial sharp increase, the increase of photocurrent is relieved and the current decreases again, probably due to the natural device decay [39]. On the other hand, a more stable current was observed after the introduction of TiO₂ nanoparticles in the dark (Fig. 4-7(a)). Furthermore, upon white-light illumination, although an initial increase in photocurrent was also observed, the magnitude was much smaller (Fig. 4-7(b)). The device only exhibited a very small current decay. The more stable photocurrent may further confirm the presence of recombination centers introduced

by the TiO_2 nanoparticles dispersed in the organic insulator; the latter can suppress the electron trapping. Without the recombination centers, the trapped electrons will cause a dramatic increase in current.

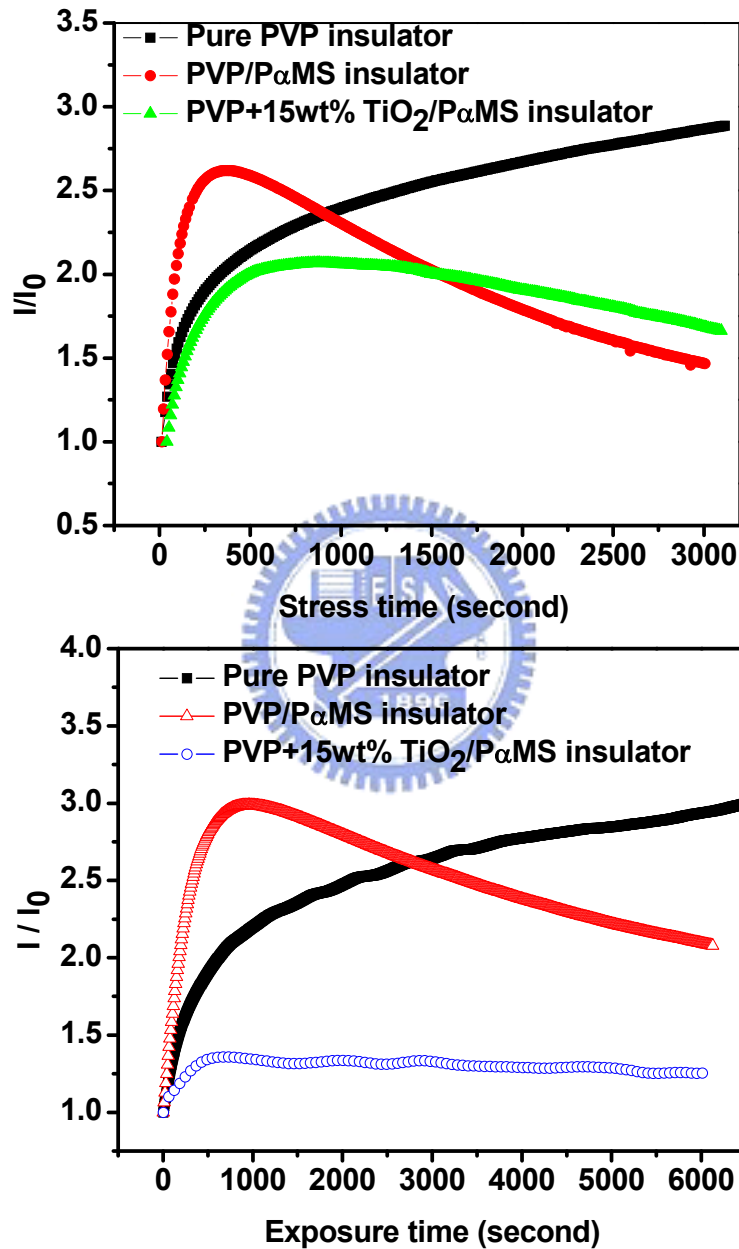


Fig. 4-7 The normalized time-dependent current of the devices (a) in the dark; and (b) under illumination (10mW). The devices with PVP and PVP/P α MS as the dielectric layers were biased at $V_{GS} = -10$ V and $V_{DS} = -10$ V; while the device with 15 wt% TiO_2 nanoparticles was measured at $V_{GS} = -5$ V and $V_{DS} = -4$ V.

4.1.4 Conclusion

It has been shown that the issues of light sensitivity and V_{TH} shift can be overcome by blending TiO_2 nanoparticles into the polymer dielectrics. The more stable photocurrent and minimized V_{TH} shift can be attributed to the recombination centers induced by the doping of the TiO_2 nanoparticles. The energy levels deep in the energy gap and away from the HOMO and LUMO of the pentacene can serve as the recombination centers, which, in turn, can enhance substantially the recombination process in the OTFTs.



4.2 Part. B Photocurrent suppression of transparent organic thin-film transistors

4.2.1 Introduction

Transparent thin-film transistors (TTFTs) have received considerable attention recently since some promising applications, such as see-through active-matrix elements for displays, could be realized by utilizing this technology [51- 54]. Currently, the most common inorganic semiconductors used for TTFTs are metal oxides, such as In–Ga–Zn–O systems, and In_2O_3 [51,52]. On the other hand, organic materials have been considered as promising candidates for the next generation electronics, since the as-made organic thin-film transistors (OTFTs) are potentially flexible, lightweight, and low cost [54,55,50]. The fusion of both research areas of TTFTs and OTFTs is expected to allow interesting applications to be developed [45]. For example, organic TTFTs will be easily integrated with common transparent screens, like the windscreens, to serve as multi-functional components in cars. In addition, OTFTs could be also applied onto the fabrication of transparent displays with great flexibility [53,44,56]. However, although TTFTs has been extensively developed, there is still very limited study about the photosensitivity of these transparent devices. The concern of photoresponse level is of great importance because the transport of light through the devices is inevitable. Therefore, it is crucial to investigate the device photoresponse and to develop methods to lower the device photosensitivity [57]. In our recent studies, pentacene-based OTFTs with high transparence have been demonstrated by inserting one thin layer of metal oxides between the transparent electrode (indium-tin-oxide, ITO) and pentacene to reduce the contact resistance [58]. However, because of its low energy gap, pentacene absorbs the visible light easily even while a thin layer is used as the active

material in OTFTs. Hence, the electrical characteristics change seriously upon illumination. In this work, we further present one method to fabricate transparent OTFTs with low photosensitivity by introducing one layer of nanocomposite dielectric layer, consisting of one polymer matrix and titanium dioxide (TiO_2) nanoparticles, into the device. The high transparency and low photosensitivity have been achieved simultaneously. It is anticipated that the transparent OTFTs reported in this study would be very suitable for the future “invisible electronics” [52].

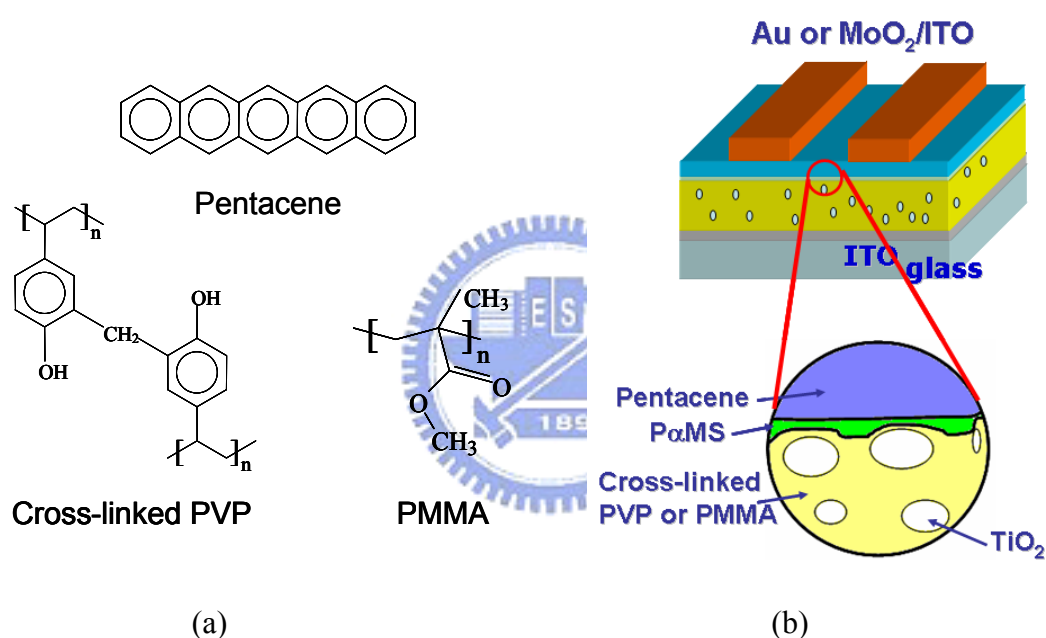


Fig. 4-8 (a) Chemical structures of the organic semiconductor, pentacene, and the polymer gate insulators, cross-linked PVP and PMMA. (b) The device structure of the OTFTs in this study.

4.2.2 Experiment

The chemical structures of the organic materials used in this study and the device structure are illustrated in Fig. 4-8. Poly-4-vinylphenol (PVP; $M_w = 20,000$) and poly(melamine-*co*-formaldehyde) methylated ($M_n = 511$) were dissolved in propylene glycol monomethyl ether acetate (PGMEA), and blended with titanium

dioxide (TiO_2) nanoparticles, whose surface was further modified with organosiloxane to enhance the solubility [27,46]. The solution was then spin-coated onto the patterned ITO glass substrates. The resulting film was further thermally cross-linked at $200\text{ }^\circ\text{C}$ and served as the gate insulator. To smooth the surface of the gate insulator, the insulator was further over-coated with a thin-layer ($\sim 2\text{ nm}$) of poly(α -methylstyrene) (P α MS), while TiO_2 nanoparticles were embedded into the gate insulator (Fig. 4-8) [46]. Then, pentacene (60 nm) was thermally evaporated as the semiconducting layer. To fabricate transparent source and drain electrodes with low contact resistance, molybdenum(IV) dioxide (MoO_2) was thermally evaporated as the hole injection layer before the deposition of ITO [58,59]. The channel length (L) and width (W) of the devices were 100 and 2000 μm , respectively. The film thickness and roughness were measured using a DI 3100 series atomic force microscopy (AFM). The current-voltage (I-V) characteristics of OTFTs were measured by a Keithley 4200 semiconductor parameter analyzer. The illumination light source was a standard Hg lamp. Incident light was from top of the device. All measurements were performed under the atmosphere.

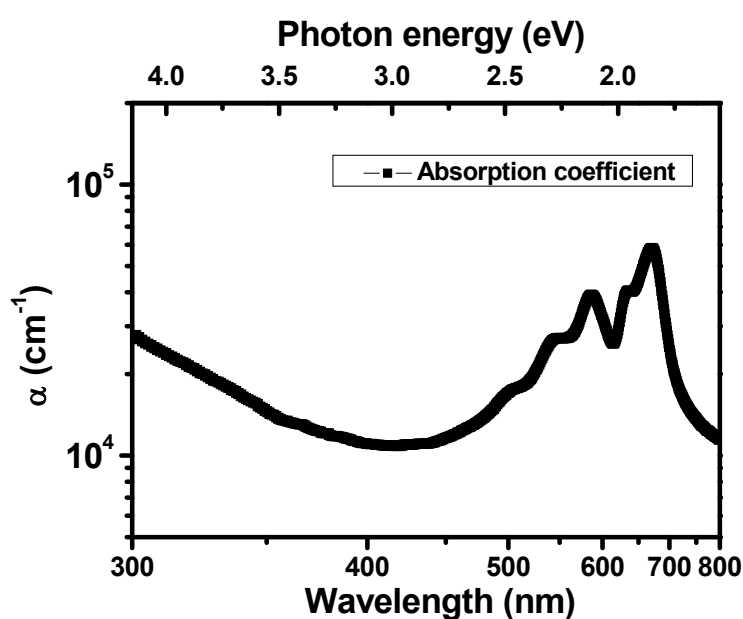


Fig. 4-9 Absorption coefficient of pentacene.

4.2.3 Result and Discussion

The ultraviolet-visible absorption spectrum of a pentacene thin-film (60 nm) on a quartz substrate is shown in Fig. 4-9. From the result, the absorption peaks of pentacene were located at 550 – 600 and 650 – 700 nm. In these wavelength ranges, the absorption coefficient (α) varied from 6×10^4 to $1 \times 10^4 \text{ cm}^{-1}$, providing a $1/\alpha$ light absorption depth from 167 – 1000 nm. Since the thickness of pentacene film is 60 nm, we can assume that the light intensity is constant across the film, and the irradiance at the channel is approximately equal to the irradiance at the film surface. The transfer characteristics of the device with the crosslinked PVP insulator and transparent electrodes are shown in Fig. 4-10(a). The extracted mobility in the saturation regime following conventional field effect transistor model was $0.12 \text{ cm}^2/\text{Vs}$. The threshold voltage (V_{TH}) and subthreshold swing (S) were 7.1V and 11.6 V/decade, respectively. The on/off ratio was about 2.6×10^4 . While the device was under white illumination ($10 \text{ mW}/\text{cm}^2$) the V_{TH} shifted to the positive direction and the off-current increased [Fig. 4-10(a)]. It has been suggested that the photogenerated electron–hole pairs increase the off-state current dramatically [43]. While the holes can be flow out through the drain electrode under the electrical field, the electrons may be trapped at the grain boundaries of pentacene, and/or the insulaor/pentacene interfaces, resulting in a positive threshold-voltage shift. On the contrary, different device behavior was observed upon blending TiO_2 nanoparticles into the gate dielectrics [57]. Fig. 4-10(b) shows the transfer characteristics of the device with 1wt% TiO_2 nanoparticles and the smooth layer (P α MS) [46]. Since the dielectric constant of TiO_2 is much higher ($\kappa = 114$) than that of the polymer matrix, the composite dielectric layer has higher dielectric constant as well. Because the field-induced current is proportional to the field-induced charge density, larger

output current was obtained under the same bias and, therefore, the operating voltage was reduced after blending of 1wt% high- κ TiO₂ into the gate insulator [27,46]. On the other hand, the device behavior under illumination was quite different from that of the device without TiO₂ nanoparticles. Upon illumination, the V_{TH} was almost unchanged and the off current merely increased slightly as shown in Fig. 4-10(b).

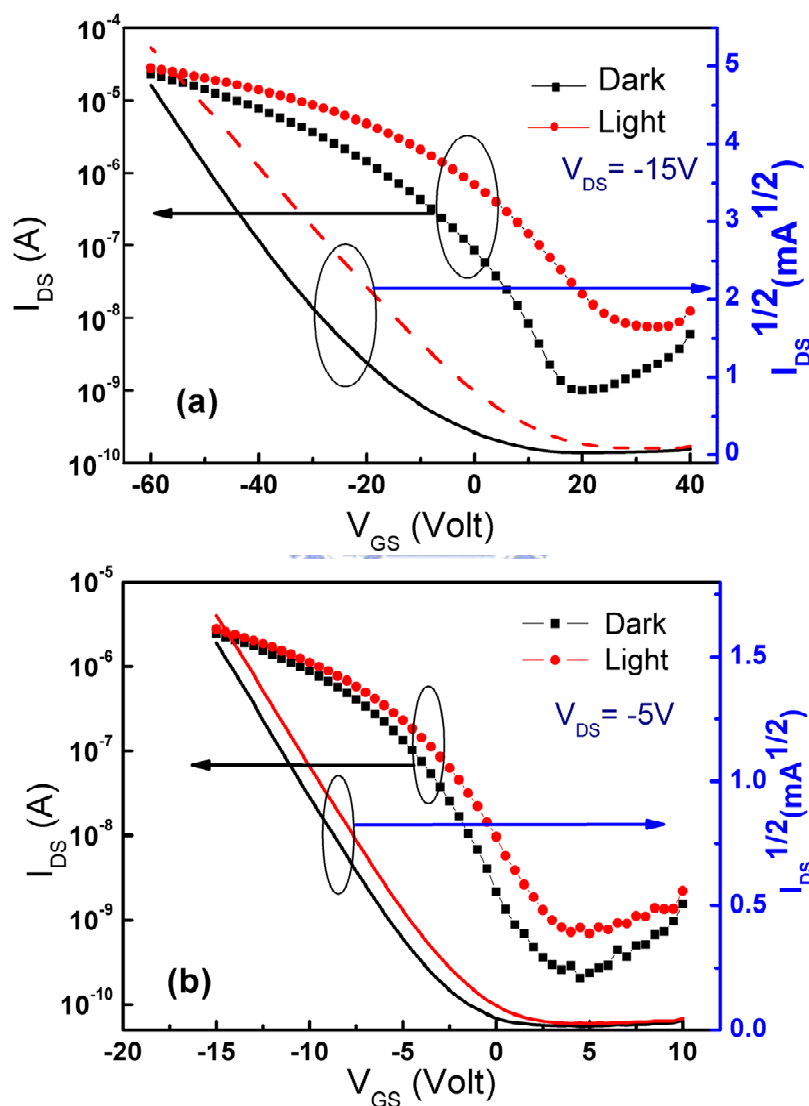


Fig. 4-10 The transfer characteristics of the OTFTs in the dark and under the illumination (10mW) with (a) neat cross-linked PVP as the gate dielectric layer; (b) cross-linked PVP/P α MS bilayer insulator blended with 1 wt% TiO₂ nanoparticles as the gate dielectric. ITO modified with MoO₂ (20 nm) was used as the source and drain electrode materials for both devices.

To explain the above results, it is suggested that recombination centers are introduced into the device after blending of TiO₂ nanoparticles.

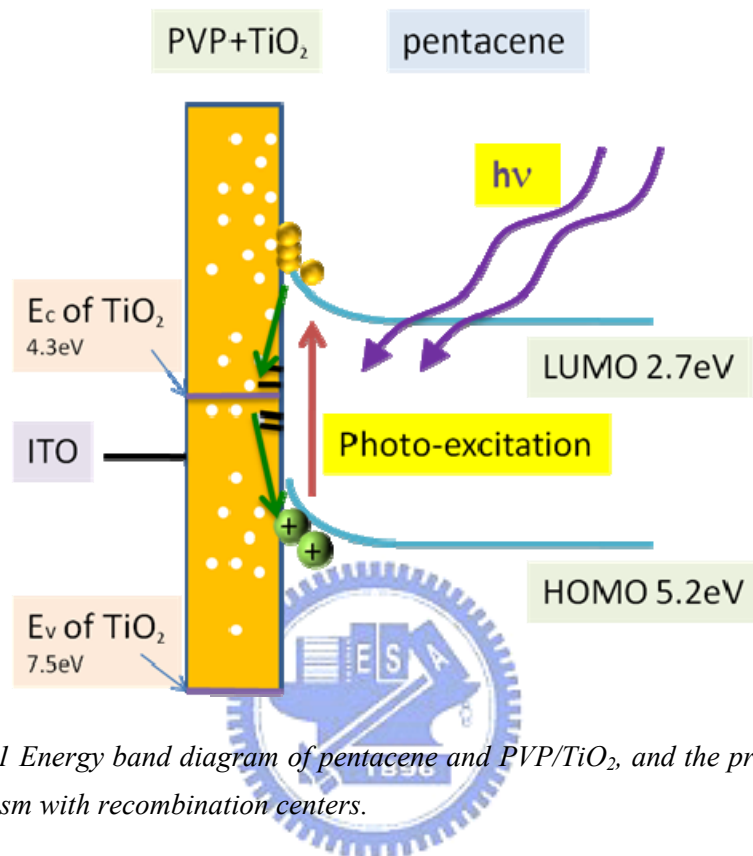


Fig. 4-11 Energy band diagram of pentacene and PVP/TiO₂, and the proposed mechanism with recombination centers.

As in Fig. 4-11, because the conduction band of TiO₂ is located between the highest occupied molecular orbital (HOMO) and the lowest unoccupied molecular orbital (LUMO) of pentacene, it may behave as recombination centers to facilitate the recombination of holes and electrons and, thus release the electron trapping. Therefore, the excess and trapped electrons upon illumination into the channel could recombine easier. As a result, with reduced number of trapped electrons, the V_{TH} shift is suppressed. In order to examine the validation of mechanism, another organic insulator, poly(methyl methacrylate) (PMMA), blended with 1wt% TiO₂ nanoparticles was used as the dielectric layer. Fig. 4-12(a) shows the transfer characteristics of OTFT with PMMA as the gate insulator. The device exhibited low

leakage current and a high on/off ratio. It is probably owing to the excellent insulating property of PMMA, because it lacks of delocalized π electrons such as those of on the benzene rings of cross-linked PVP.

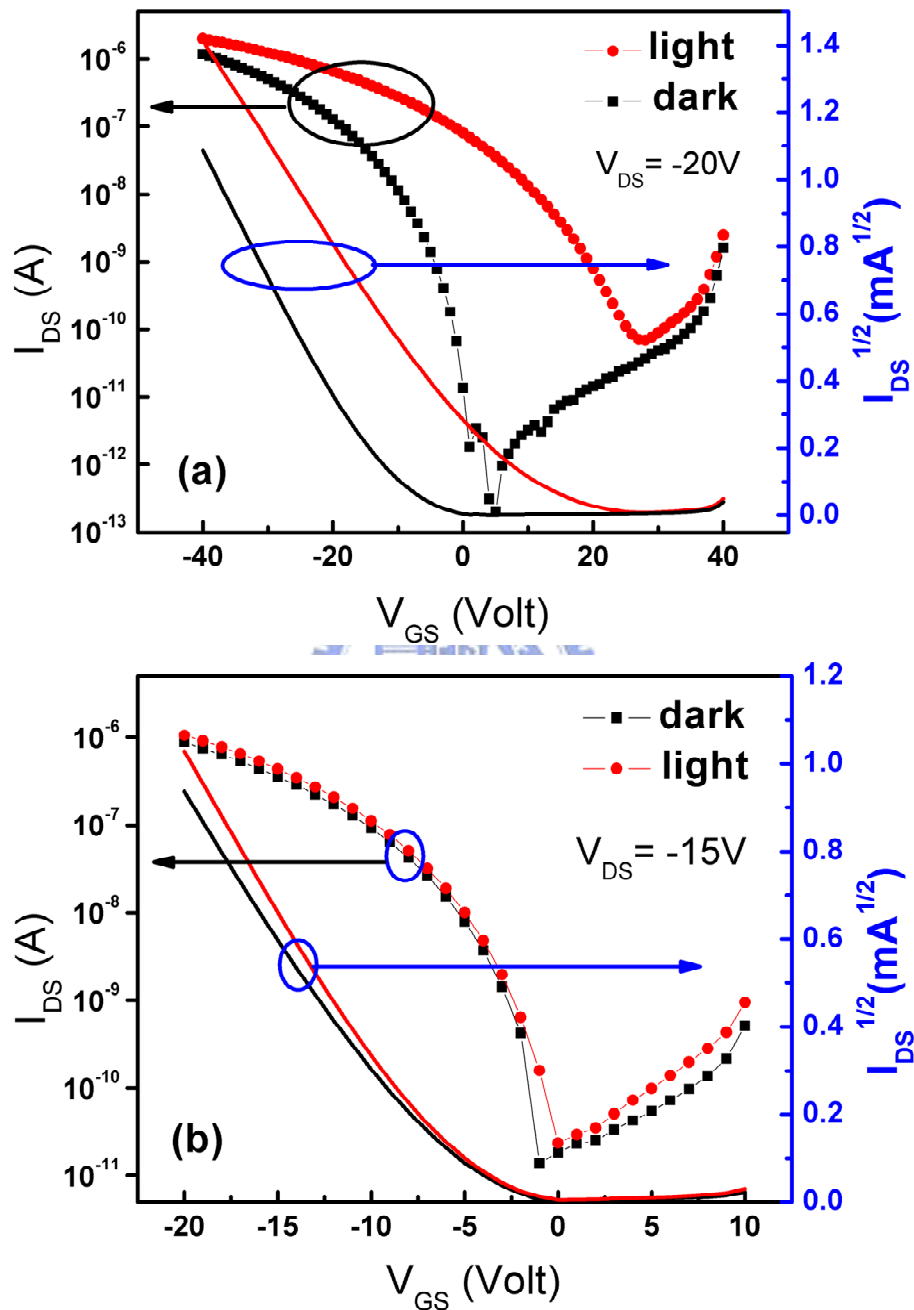


Fig. 4-12 The transfer curves for devices in the dark and under the light illumination (10mW) with (a) neat PMMA as the gate insulator; (b) PMMA blended with 1wt% TiO_2 as the gate insulator.

However, the mobility in the saturation region ($0.08 \text{ cm}^2 / \text{Vs}$) was lower than that of the device with PVP gate insulator, which might be due to the different morphology of pentacene on PMMA. While the device was under white illumination (10 mW/cm^2), a very large V_{TH} shift was also observed. The off-current also increased upon the illumination. Similar to the case of the device with cross-linked PVP (Fig. 4-10), the same phenomenon suggests electron trapping in the conducting channel. On the contrary, while 1wt% TiO_2 nanoparticles were incorporated into PMMA, not only the operating voltage was reduced because of the higher dielectric constant of the dielectric layer but V_{TH} shift was eliminated as well [Fig. 4-12(b)]. Therefore, no matter what polymer matrix was used, once TiO_2 has been added, the photoresponse of the device was reduced. From the results in Figs. 4-10 and 4-12, it is realized that TiO_2 nanoparticles are essential. Since both kinds of inert polymers (PMMA and crosslinked PVP) with different chemical structures exhibit similar device behavior with reduced photosensitivity, it demonstrated the trust worthiness of this recombination center model.

It is interesting to reduce operating voltage by utilizing high dielectric constant gate insulator [17]. N (accumulated carriers in the channel region) depends on both the dielectric constant of the gate insulator and its thickness, whereas E (gate field) depends on only its thickness. By using higher dielectric constant insulators, a sufficient number of carriers to fill all traps are generated by the field effect at much lower gate voltages. As a result, operating voltage can be reduced as well. From our previous report [60], eq. (4-1), can accurately predict the dielectric constant of nano-composite.

$$(1 - \nu) \frac{\epsilon_1 - \epsilon_c}{\epsilon_1 + 2\epsilon_c} + \nu \frac{\epsilon_2 - \epsilon_c}{\epsilon_2 + 2\epsilon_c} = 0 \quad \text{eq. (4-1)}$$

Here, ϵ_c , ϵ_1 , and ϵ_2 are the composite, base, and filler dielectric constant, respectively, and v is the filler volume percentage. The dielectric constant of bulk film rised from 4.3 (Cross-linked PVP), 2.7 (PMMA) to 4.8 and 2.9, respectively after blending 1wt% TiO_2 nanoparticles. Although the dielectric constant of these bulk films did not increase dramatically, the more accumulated carrier concentration was attained by high dielectric constant ($\kappa = 114$) of TiO_2 nanoparticles closed to the channel regime. Not only the photosensitivity respect to white illumination has been reduced, a high transparence has also been achieved simultaneously. Transparent OTFTs have been demonstrated by using NiOx or printed carbon nanotubes as the transparent electrodes [44,53,56]. In our approach, MoO_2 was utilized as the hole injection layer, resulting in good ohmic contacts with pentacene when ITO was used as the source/drain electrodes [58].

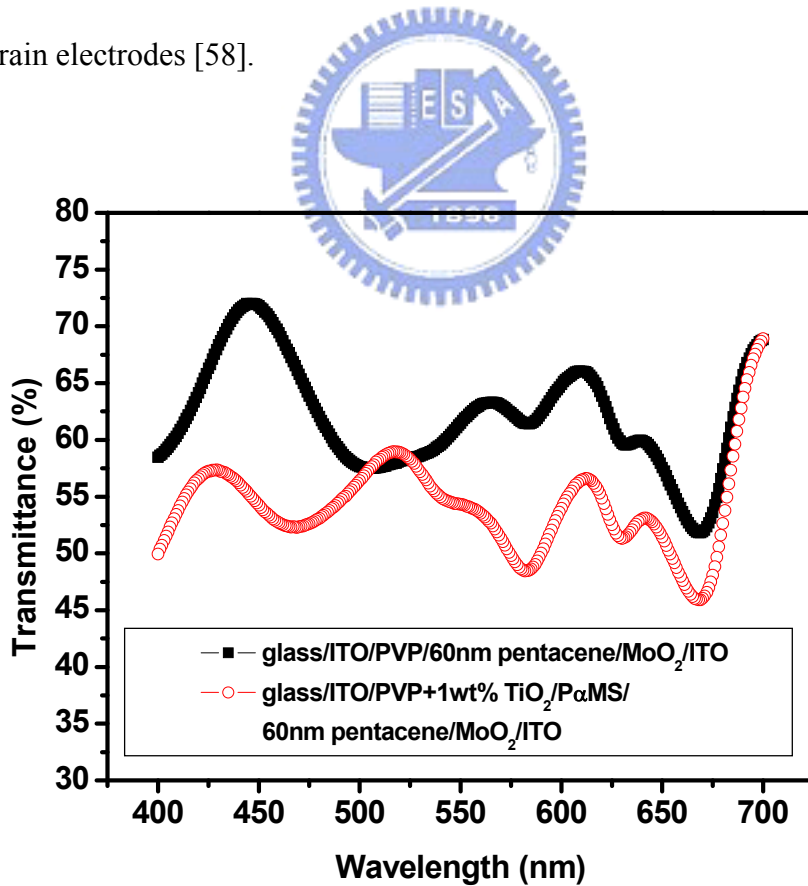


Fig. 4-13 Transmittance spectra of various OTFT layers.

The transmittances of the devices with cross-linked PVP and with the nanocomposite insulator as the dielectric layer are shown in Fig. 4-13. The average transmittance of the device with PVP was about 62% in the visible region. For the device with TiO₂ nanoparticles, the transmittance decreased slightly due to the light-scattering from the nanoparticles. However, the average transmittance remained as high as 54%. Hence, the photosensitivity of pentacene based OTFTs were resolved effectively and could be used in active driving circuits without the drawback of noticeable V_{TH} shift.

4.2.4 Conclusion

Organic and transparent thin-film transistors with reduced photoresponse have been demonstrated by using the TiO₂ nanoparticles as the additives in the gate insulators. The as made device shows simultaneously a high transparency and a minimal threshold voltage shift under white light illumination. It is inferred that the localized energy levels deep in the energy gap and away from the HOMO and LUMO of pentacene behave as the recombination centers, enhancing substantially the recombination process in the organic TFTs. Hence, the electron trapping is relieved and the shift of threshold voltage is reduced upon white illumination. Finally, the device shows great promises to realize the next generation electronics with invisibility.

Chapter 5

Color filtering functional organic thin-film transistors

5.1 Part. A Organic thin-film transistors with color filtering functional gate insulators

5.1.1 Introduction

Organic electroactive materials have received much attention recently because they could offer low-cost approaches, such as low temperature and printing methods, for the manufacture of electronic products [61]. Additionally, the devices made of organic compounds have great potential for applications on flexible electronics such as smart cards, radio-frequency identification tags, and paper-like displays [62- 67,24]. On the other hand, from the viewpoint of the value structure of printing technology, it is necessary to reduce the number of printing steps to fabricate truly low-cost products [61]. Therefore, to accomplish printed electronics, one rather promising approach is to use a multifunctional material (ink) as the common component of different devices in parallel in a certain electronic system [61]. For example, the polymer material, poly(3,4-ethylenedioxythiophene): poly(styrenesulphonate) (PEDOT:PSS), could be used as the active material for electrochemical transistors, electrochromic displays, push-button input devices and batteries in a system-on-a-sheet label [68]. As a result, only one step is required to print the PEDOT:PSS layer for all the devices in the electronic label. Herein, we reported organic thin-film transistors (OTFTs) with an additional function of color-filtering. The colored polymer insulators not only serve as the dielectric

materials for field-effect transistors, which could be the driving-circuits, but also as color filters for liquid crystal displays (LCDs). Traditional LCDs compose of a backlight module, 2 polarized films, a TFT circuit array, a liquid crystal layer, and a color filter array. For saving the earth, reducing the number of process steps, improving material recycling ratio, and minimizing energy/waste have to be taken into consideration. This work represents one potential example for multifunctional organic electronics. Further, since color filters significantly contribute the bulk of material cost, integrating color filters and gate insulators is also an effective method for reducing the overall cost of LCDs and process steps.

5.1.2 Experiment

Typical colorant inks are composed of dispersants, nano-sized pigments, styrene, acrylic acid, and azo-bisisobutyronitrile. To achieve multiple functions, we further introduced a polymeric material, poly(2,2,2-trifluoroethyl methacrylate) (PTFMA) [69,70] (Fig.5-1), whose dielectric constant (κ) is equal to 6.0, to modify the surface of the color filters. The PTFMA layer smoothes the surface of the color filters, facilitating the crystallization of the semiconducting molecules, pentacene, and its higher dielectric constant helps to induce more field-effect charges, increasing the output current and driving capability. The molecular structure of PTFMA is similar the that of polymethylmethacrylate (PMMA) (Fig. 5-1). Although PMMA has excellent film formation properties, the low dielectric constant of PMMA ($\kappa = 2.7$) [71] usually results in lower output current. Therefore, we replaced the hydrogens on the terminals of the side chains with trifluoromethyl ($-\text{CF}_3$) groups. Owing to its high polarity, the CF_3 group increased the dielectric constant from 2.7 to 6.0. As a result, the use of PTFMA could increase the capacitance of the dielectric insulators.

Further, from the viewpoint of optical properties, PTFMA has limited absorption in the visible regime. Therefore, the absorption spectra and the corresponding CIE coordinates of the multilayer insulators remain unchanged.

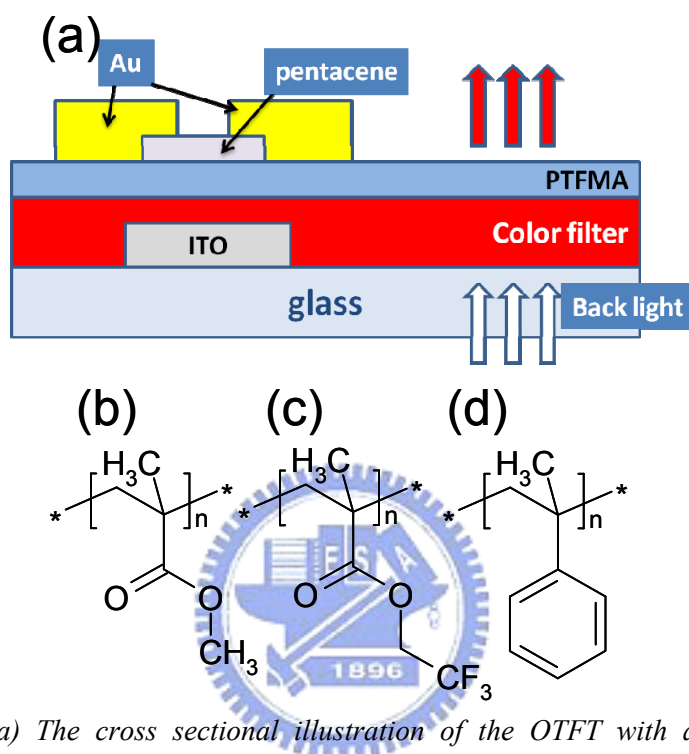


Fig. 5-1 (a) The cross sectional illustration of the OTFT with a bi-layer colored dielectric insulator consisting of a commercial color filter and PTFMA. (b) Chemical structure of polymethylmethacrylate (PMMA) (c) Chemical structure of poly(2,2,2-trifluoroethyl methacrylate) (PTFMA). (d) Chemical structure of poly(α -methylstyrene) (P α MS).

The cross-section of the OTFTs in this work is illustrated in Fig. 5-1. The devices were fabricated on indium tin oxide (ITO) patterned glass substrates and the 100 nm thick ITO was used as the gate electrodes. Commercial colorant inks (Everlight Chemical Industrial Corporation) [46] were spin-coated on the substrates, and the colored films were subsequently cured at 90°C for 15 min and then at 230°C for 40 min. PTFMA dissolved in propylene glycol monomethyl ether acetate (PGMEA) (9.0 wt%) was spin-coated on the as-prepared color filters and then cured at 100°C

for 1 hr. For some devices, an additional layer of poly(α -methylstyrene) (P α MS) (5 nm) was further coated from toluene solutions (0.1 wt%). After the preparation of the dielectric layers, pentacene was thermally evaporated on the insulators as the semiconductors of the devices. Finally, gold was thermally deposited as the source (S) and drain (D) electrodes through a shadow mask. The channel length (L) and width (W) of the pentacene OTFTs were 130 and 2000 μm , respectively. The devices with a metal-insulator-metal (MIM) structure, consisting of the dielectric layers sandwiched between ITO and Al, were used for capacitance measurements. The calculated dielectric constants were 3.5, 4.7, and 4.0 for red, green, and blue dielectric layers, respectively. The capacitance measurements were conducted with a HP 4284A Precision LCR meter. The transmittance spectra were obtained by a Perkin Elmer Lambda 650 spectrometer. The CIE coordinates were measured by a ConoScope (Autronic-Melchers, GmbH). The film thickness and roughness were measured using a DI 3100 series atomic force microscope (AFM). The electrical characteristics of the OTFTs were measured with a Keithley 4200 semiconductor parameter analyzer in a light-shielded ambient environment.

5.1.3 Result and discussion

Initially, the colorant materials were used directly to serve as the dielectric layers. However, limited field-effect and larger hysteresis were observed. The poor device performance was probably owing to the high polarity of the surface. On the other hand, after the modification of PTFMA, hysteresis was inhibited and larger output current was obtained. Fig. 5-2(a) show the transfer characteristics of color filtering OTFTs at room temperature. The extracted motilities in the saturation region following the conventional field effect model were 0.31, 0.21, and 0.42 cm^2/Vs for

red, green, and blue devices, respectively. On/off current ratios for all the devices were around 10^5 . We also discovered that the red device modified with a second thin layer of P α MS layer had an even higher mobility ($\sim 0.51 \text{ cm}^2\text{Vs}$) [Fig. 5-2(a)].

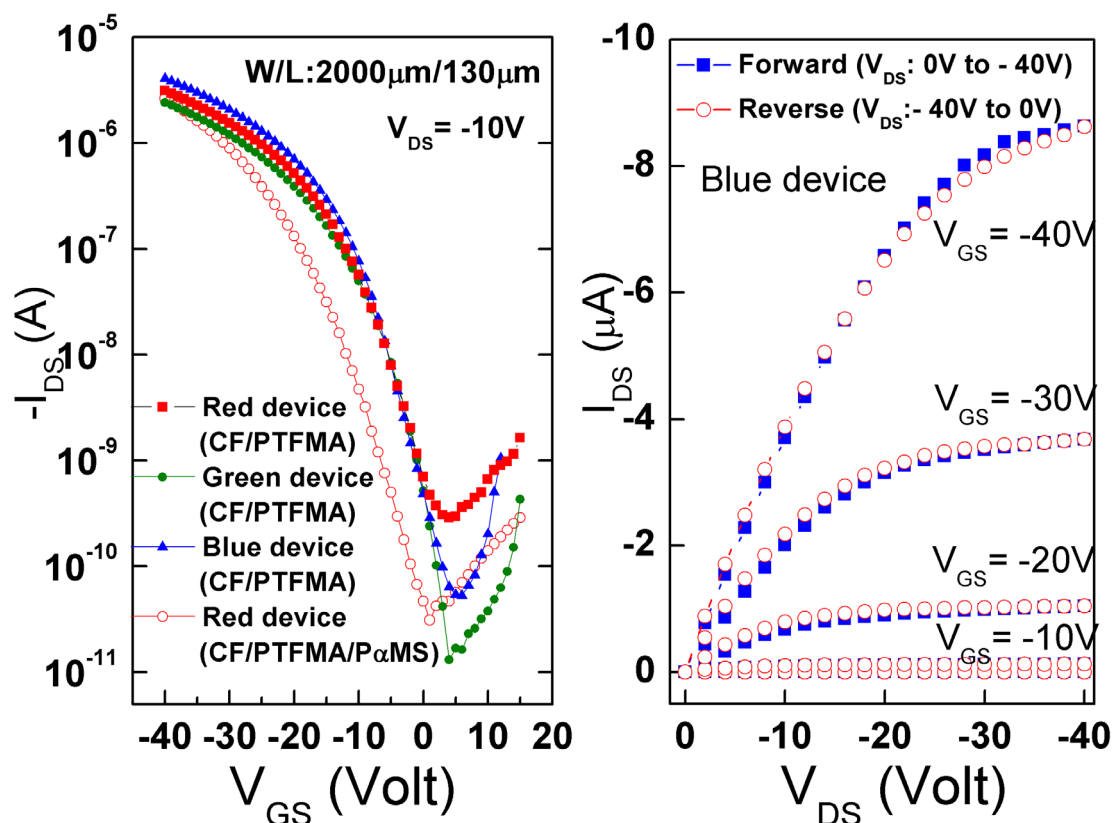


Fig. 5-2 (a) The transfer and (b) output characteristics of the color filtering functional devices.

Further, Fig. 5-2(b) shows the typical output characteristics of colored devices (with a blue colored dielectric insulator in this case). Apparently, when the gate voltage was reversely swept, very limited hysteresis was observed, suggesting very stable device characteristics.

To further identify the function of the buffer layer, PTFMA, the surface morphologies of the colored films and the pentacene thin films on different

dielectric surfaces were examined by AFM. The typical AFM images are displayed in Fig. 5-3.

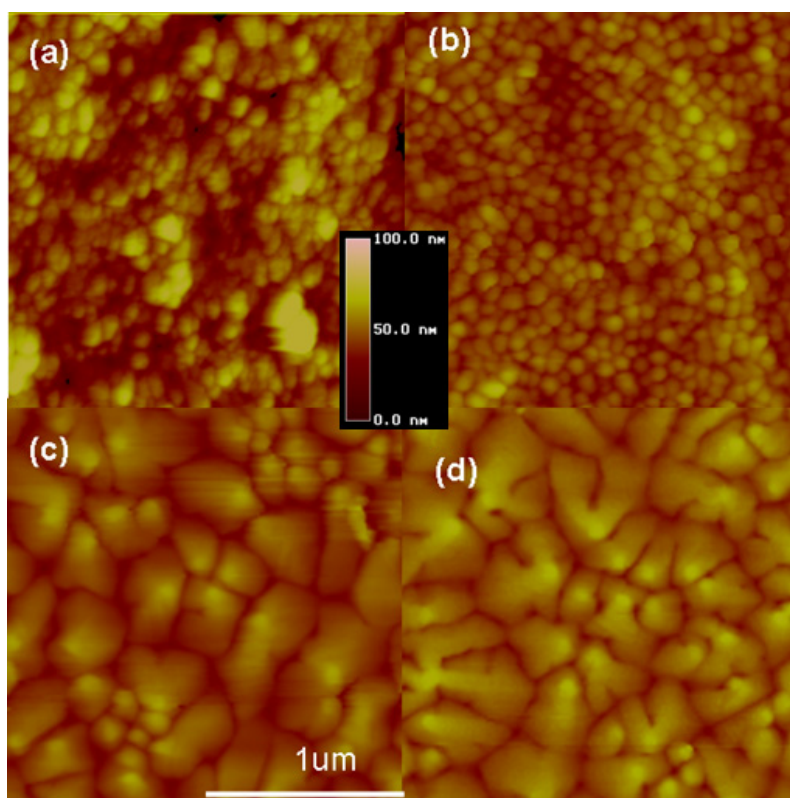


Fig. 5-3 (a) The AFM image of the surface of the red color filter. The surface morphology of the pentacene layers on (b) the red color filter; (c) the red color filter/PTFMA insulator; (d) the tri-layer red color filter/PTFMA/P α MS insulator.

The surface of the color filters was quite rough as shown in Fig. 5-3(a). Therefore, pentacene molecules were not able to grow well on the rough surface. The grain size of pentacene on the neat color film was very small, thereby leading poor device performance [Fig. 5-3(b)]. The grain boundaries might trap great amount of charges, limiting charge transport and resulting in significant hysteresis. On the other hand, the grain size on the surface of the PTFMA modified bilayer insulator became larger

[Fig. 5-3(c)]. The PTFMA significantly smoothed the surface and further changed the surface energy of the colored film, facilitating the crystallization of pentacene molecules. Further, for the devices with tri-layer insulators, pentacene also grew well on P α MS. [Fig. 5-3(d)]. The more “compact” grains of the pentacene film probably reduced the density of charge traps at the grain boundaries, leading to even higher device mobility [Fig. 5-2(a)]. The nonpolar nature of P α MS might improve the crystal growth of pentacene. The results of the morphology study were consistent well with the aforementioned electrical characteristics.

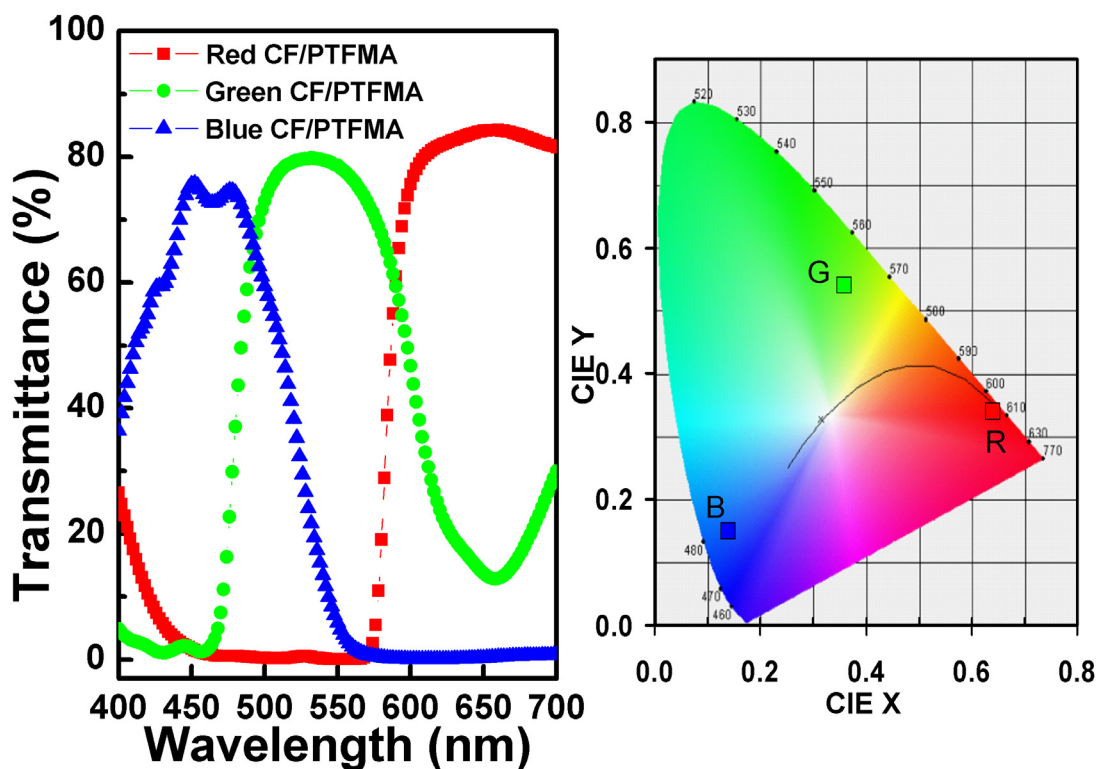


Fig. 5-4 Optical properties of red, green, and blue functional OTFTs: (a) The transmission spectra and (b) CIE 1931 coordinates.

Since the light absorption of organic materials increases with the film thickness, thick color filter layer usually have better filtering performance. On the other hand, the capacitance of the gate dielectric decreases with the increasing insulator

thickness. Therefore, the smaller capacitance would lead to lower density of field-effect charge carriers and, therefore, higher operating voltages. As a result, the optimum thicknesses of red, green, and blue colorant films with PTFMA bi-layer were 1.36, 1.20, and 1.37 μm , respectively. Fig. 5-4(a) shows the transmission spectra of these colored devices. The light transmitted through ITO glasses, the color-filtering and the PTFMA layers. Since PTFMA has limited absorption in the visible regime, the absorption spectra were almost unchanged after the addition of the PTFMA layer. Fig. 5-4(b) shows the corresponding CIE coordinates, which were (0.64, 0.34), (0.36, 0.54) and (0.14, 0.15) for red, green and blue devices, respectively, covering 49.2% National Television Systems Committee (NTSC) standard. From the above results, it is proved that the devices not only have high electrical performance, but also have satisfied optical properties.



5.1.4 Conclusion

In summary, we demonstrated color filtering OTFTs with multilayer gate insulators exhibiting high field effect mobilities, on-off current ratios as well as color filter functions. The PTFMA polymer smoothed the surface of the colored films and improved the crystallization of pentacene molecules, thereby enhancing the device performance. This study provides an alternative approach to integrate gate insulators and color filters in LCDs, and even open a new vision for developing unique materials which having color-filtering, insulating, and polarizing abilities. Finally, the current work also represents one practical example for multifunctional organic electronics.

5.2 Part. B Organic thin-film transistor with colorful PMMA gate dielectrics

Over the years, there has been great interest in thin-film transistors made of organic compounds. This is mainly due to the fact that organic thin-film transistors (OTFTs) have many unique advantages which range from light weight, flexibility, low fabrication cost, and solution processability [62-68]. Traditional OTFTs compose of silicon dioxide or silicon nitride as gate insulators. However, the use of inorganic dielectrics deposited at high temperatures is not quite attractive for large area display applications. Organic and polymeric materials which can be solution-processed to be gate insulators are more suitable for low temperature manufacturing and flexible application [30]. There are many organic and polymeric materials to be used as gate insulators, such as benzocyclobutene (BCB), polyvinyl phenol (PVP), polymethyl methacrylate (PMMA), and polyvinyl alcohol (PVA) [30]. For our study, we first utilize colored polymer PMMA to demonstrate colorful TFTs. The novel colored PMMA layers not only serve as gate dielectric but also show color filtering function, which offers a cost effective way to integrate color filters and gate dielectrics together.

OTFTs were fabricated using staggered source and drain electrodes and patterned 100nm-thick ITO glass substrate. The cross-sectional view of the OTFTs in this work is illustrated in Fig. 5-5. Commercial PMMA and Dyeing polymer P6-A [72] (5wt%) were spin-coated onto the substrates and cured at 100⁰C for 30 min to form 650 nm gate insulators. After that, 60 nm pentacene (Aldrich without purification) and 50 nm Au source/drain electrodes were thermally evaporated through stencil mask sequentially. The channel length (L) and width (W) of the TFTs were 130 and

2000 μm , respectively. The devices with a metal-insulator-metal (MIM) structure, consisting of the dielectric layers sandwiched between ITO and Al, were used for capacitance measurements [70]. The calculated dielectric constants were 2.7 and 2.8 for PMMA and colored P6-A, respectively. The capacitance measurements were conducted with a HP 4284A Precision LCR meter. The electrical properties of devices were then measured using a Keithley 4200 IV analyzer. The thin-film transmittance and its corresponding thickness were measured by using a Lambda 650 UV/Vis spectrophotometer and an Alpha-step IQ Surface Profiler, respectively. Film morphology was monitored by Atomic Force Morphology (DI 3100 series).

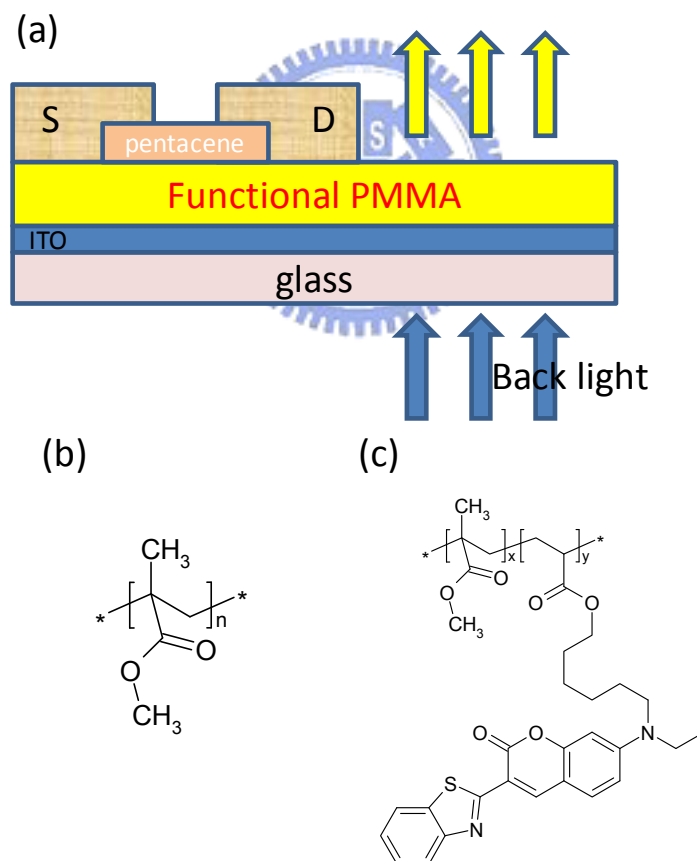


Fig. 5-5 (a) The cross sectional illustration of the OTFT with a colored dielectric insulator P6-A. (b) Chemical structure of polymethylmethacrylate (PMMA). (c) Chemical structure of P6-A, X:Y=50:1.

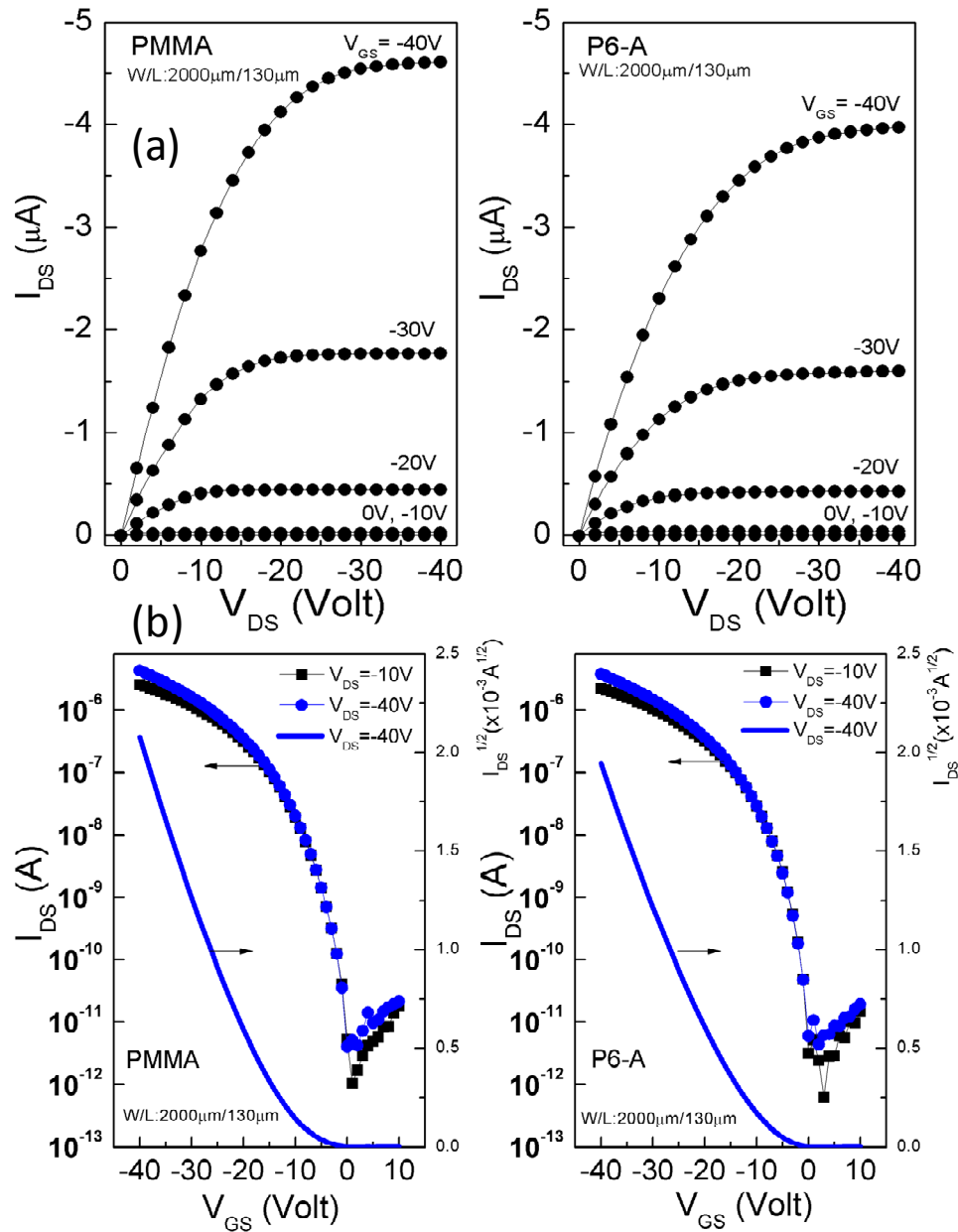


Fig. 5-6 (a) I_{DS} - V_{DS} curves and (b) I_{DS} - V_{GS} transfer characteristics of the PMMA and P6-A devices.

We proposed a new concept that using colored PMMA (called P6-A) replaced of traditional transparent PMMA as shown in Fig. 5-5(c). We used organic synthesis methods to put functional groups into PMMA polymer chain [70]. White light will be absorbed and translated into desired colors. We characterized the TFTs electrical properties composed of PMMA and P6-A gate insulators as shown in Fig. 5-6(a) and

Fig. 5-6(b). The standard MOSFET saturation-region drain current equation was used for parameter extraction:

$$I_{DS} = \mu_{eff} C_{ox} \frac{W}{2L} (V_{GS} - V_{TH})^2 \quad \text{eq. (5-1)}$$

where C_{ox} is the gate insulator capacitance per unit area, μ_{eff} is the field-effect mobility, V_{TH} is the threshold voltage and W and L are channel width and length of the TFT device, respectively. The extracted μ_{sat} from the PMMA and P6-A OTFTs is 0.17 and 0.13 cm^2/Vs , respectively. V_{TH} value of saturation regime is -10.31 and -9.02 V calculated by 90%-10% linear fit method of the $I_{DS}^{1/2}$ vs. V_{GS} curve. We also evaluate the TFT subthreshold swing (S) between off and on states, using the following equation:

$$I_{DS} \propto 10^{\frac{V_{GS}}{S}} \quad \text{eq. (5-2)}$$



The S of PMMA and P6-A devices is 1.34 and 1.35 V/decade. Off state drain current (I_{DS-off}) of both devices are also around 1 pA. The results reveal that P6-A not only keeps good insulating behavior but also shows similar interface states. To further quantify the interface states difference, from the value of the S , we can also calculate the equivalent maximum density-of-states that can be present at the semiconductor/gate insulator interface:

$$N_{ss}^{max} = \left(\frac{S \log(e)}{kT/q} - 1 \right) \frac{Ci}{q} \quad \text{eq. (5-3)}$$

where Ci is the gate insulator capacitance, q is the electron charge, κ is the

Boltzmann constant, and T is the temperature. N_{ss}^{\max} can be used to compare devices with different gate insulator characteristics. The calculated N_{ss}^{\max} values of PMMA and P6-A devices are 5.88×10^{11} and $6.14 \times 10^{11} \text{ cm}^{-3}$, respectively. The maximum surface states of P6-A device is only 4.42% more than PMMA device.

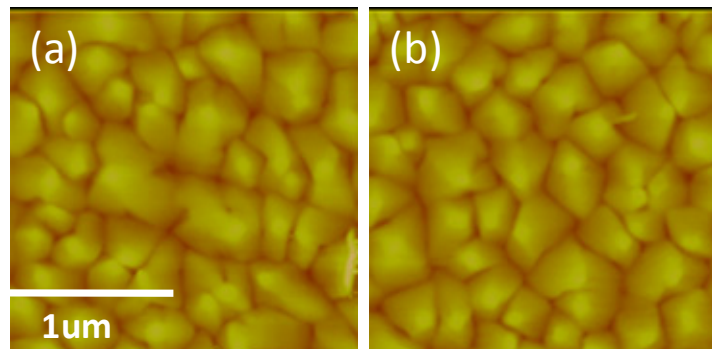
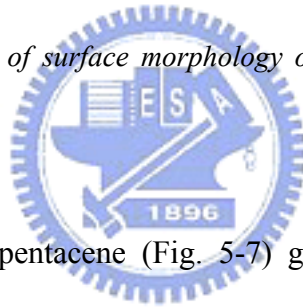


Fig. 5-7 The AFM image of surface morphology of the pentacene layers on PMMA and P6-A.



Besides, AFM images of pentacene (Fig. 5-7) grown onto PMMA and P6-A insulator exhibit all of them were well crystallized. From these results, we can conclude that P6-A demonstrate similar insulating and surface properties to traditional PMMA.

We illustrated our colored TFT measurement results of transmittance and CIE coordinates in Fig. 5-8(a) and 5-8(b). Light pass covers layers only including substrate, ITO and insulator layers. Fig. 5-8(a) shows the transmittance of PMMA, P6-A, and conventional red color filter devices presented in ref. x. For our case, wavelength of light larger than 500 nm can pass through P6-A while less than 500 nm will partially absorbed. Fig. 5-8(b) points out the CIE coordinates value is (0.41, 0.45). Since the transmittance and CIE don't meet conventional color filter

specification, we can further study to put suitable functional group into polymer chain to get the desired color.

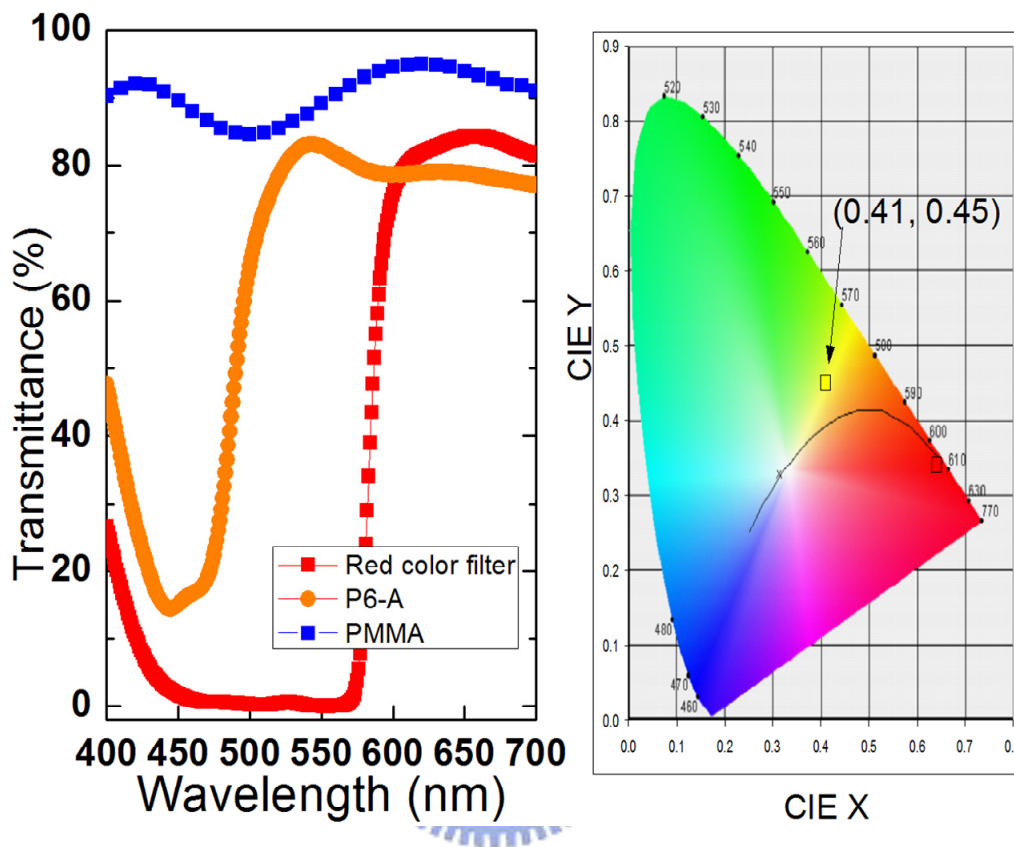


Fig. 5-8 Optical properties of colored OTFTs: (a) The transmission spectra and (b) CIE 1931 coordinates.

In summary, we have shown that OTFTs can be colored by utilizing functional gate insulator. P6-A exhibits same insulating and interface states comparing to conventional PMMA. This method offers an easy and economically viable way to prepare gate insulators of OTFTs with color filtering functions. Hence, we can conclude that this method presents a new way to integrate color filter and gate insulator by ink jet printing processes.

Chapter 6

Photosensitivity of amorphous In-Ga-Zn-O thin-film transistors

6.1 Introduction

Today, conventional active-matrix (AM) flat panel displays (FPDs) are based on amorphous or polycrystalline silicon thin-film transistor (TFT) technology. Limitations of amorphous silicon (a-Si:H) include visible light sensitivity and a low field-effect mobility, which reduce the pixel aperture ratio and driving ability for some applications. Although polycrystalline silicon TFTs have a larger field-effect mobility, their uniformity over large area might not be acceptable for high yield manufacturing. Over the last several years, there has been great interest in thin-film transistors made of transparent oxide semiconductors [73,74,12]. This is mainly due to metal oxide semiconductor thin-film transistors' unique advantages, such as visible light transparency, large-area uniform deposition at low temperature, and high carrier mobility. However, conventional metal oxide semiconductors such as zinc oxide (ZnO) are polycrystalline in nature, even at room temperature. The grain boundaries of such metal oxides could affect device properties, uniformity and stability over large areas. To overcome this issue, a new ternary oxide material comprised of In, Ga, Zn and O has been proposed for use as the channel layer in TFTs [51]. The amorphous In-Ga-Zn-O (a-IGZO) can more easily form a uniform amorphous phase while still having a high carrier mobility, like most oxide semiconductors. Although several papers have discussed the a-IGZO TFT electrical

performance and its visible light transparency, a more in-depth photosensitivity study is necessary for implementing this technology in real display or photo-sensor products. In this paper, we report on the optical and electrical properties of amorphous a-IGZO TFTs, which are suitable for active-matrix display and photo-sensor applications.

6.2 Experiment

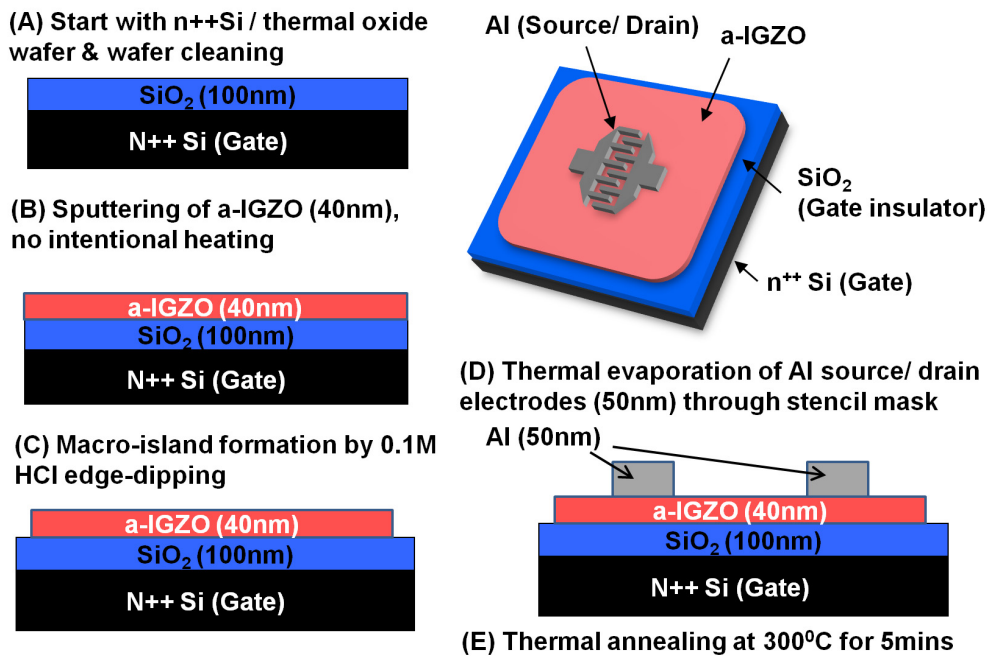


Fig. 6-1 a-IGZO TFT processes.

We made the device on the silicon substrate. Fig. 6-1 shows a bottom gate a-IGZO TFT structure used in this study. A heavily doped (N^{++}) silicon wafer with 100 nm thermal oxide layer was selected as the gate electrode and insulator, respectively. A 40 nm thick a-IGZO (In:Ga:Zn=1:1:1) active layer was deposited on the substrate by pulse-laser deposition (PLD) [75]. A KrF laser ($\lambda=238$ nm) was used and the laser energy density was set at ~ 2 J/cm²-pulse. The substrate was

placed in an ultra-high vacuum system where the target-to-substrate distance is 3 cm and the deposition was done in an oxygen atmosphere ($\sim 8\text{Pa}$) without any intentional substrate heating. Before the source/drain electrodes deposition, a macro-island was formed by edge-dipping/etching of the substrate in 0.1M HCl solution. The 50 nm thick aluminum (Al) source/drain electrodes were deposited through stencil mask openings by thermal evaporation. Finally, the device was thermally annealed in air at 300°C for 5 min. In order to get a good and uniform photo-response under light illumination, finger-type (interdigitated) source/drain electrodes are chosen as shown in Fig. 6-1. We also deposited a-IGZO thin film directly onto quartz substrate to measure its optical properties. The absorption spectrum of a-IGZO thin-film was collected by a Cary 5E UV-VIS spectrometer using polarized light [76]. Quartz substrates were used to minimize the back ground interference during transmittance measurement. Electrical measurement of the a-IGZO TFT were carried out with a probe station system located in a light tight box. The transistor electrical properties were measured by a PC controlled Agilent 4156 Parametric Analyzer. For measuring TFT transfer characteristics, the drain-to-source voltage (V_{DS}) was changed between 0.1V and V_{GS} , and gate-to-source voltage (V_{GS}) was varied from -10 V to 20 V. For photoelectric measurement, photo excitation was provided by a He-Xe lamp in combination with narrow band filters and an optical fiber. The monochromic light passed through a fiber cable and probe station microscope, which is used to focus the illumination on the specific device. The wavelengths ranging from 660 to 365 nm with a constant optical flux of 1×10^{13} photons/cm²-sec incident on the a-IGZO TFT channel were used in this experiment. For each measurement light intensity was calibrated by Oriel 70260 radiant power meter with the photodiode sensor attached. All measurements were done at room temperature in ambient air.

6.3 Result

● 6.3.1 a-IGZO Optical Properties

We studied the optical absorption spectrum of the PLD a-IGZO thin films (thickness=181nm) (Fig. 6-2). We assumed parabolic densities of band states within a-IGZO and extracted the optical energy band gap (E_g , also called Tauc gap) by applying the Tauc method [77]:

$$(\hbar\omega\alpha)^{1/2} = B(\hbar\omega - E_g) \quad \text{eq. (6-1)}$$

where $\hbar\omega$ is the photon energy (E) and α is the absorption coefficient. The Tauc gap (E_g) was determined to be ~ 3.05 eV as shown in Fig. 6-2. We also observed the exponential energy dependence of the absorption coefficient in the vicinity of E_g which can be described by [77]:

$$\alpha \propto \exp\left(\frac{E}{E_0}\right) \quad \text{eq. (6-2)}$$

where E is the photo energy and E_0 is the characteristic slope also frequently called Urbach energy. The Urbach energy is determined to be around 124 meV as indicated in Fig. 6-2. The Urbach energy is related to the joint density-of-states determined by both conduction and valence band tail states. However, the valence-band-tail can be broader (or shallower) than conduction-band-tail and dominates the optical absorption [78].

As a result, Urbach energy will be fairly close to the valence-band-tail slope value. Such phenomenon had been commonly observed in a-Si:H thin-film; and

conduction-band-tail slope is usually about half of the valence-band-tail slope [79]. If we assume a similar situation to occur in a-IGZO, the valence-band-tail slope is approximately 124 meV. This values should be confirmed by other methods in near future.

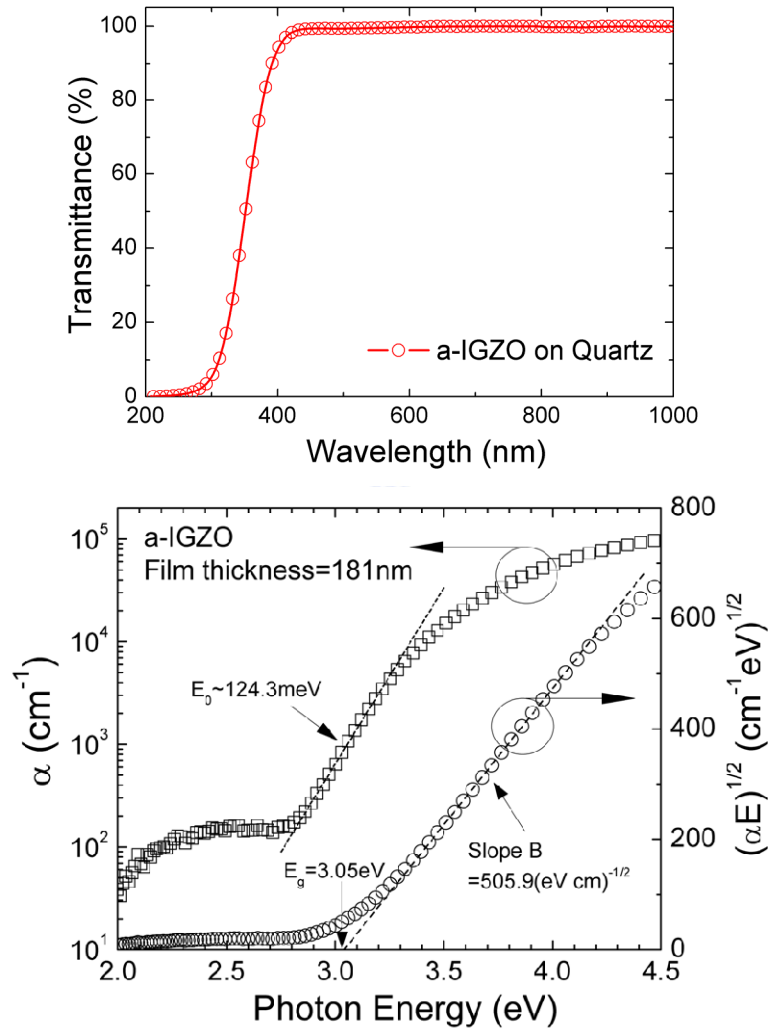


Fig. 6-2 Optical absorption spectrum of PLD a-IGZO thin film.

● 6.3.2 a-IGZO Electrical Properties

We used four-point measurement method to study the thermal conductivity and activation energy of the PLD a-IGZO thin films (thickness=40nm). Different amounts of current were applied between first electrode and fourth electrode and the voltage drops were recorded by second and third electrodes. (Fig. 6-3)

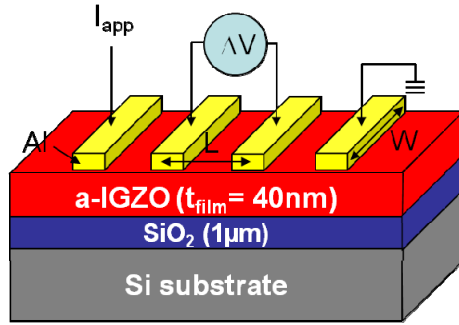


Fig. 6-3 Illustration of four-point measurement method

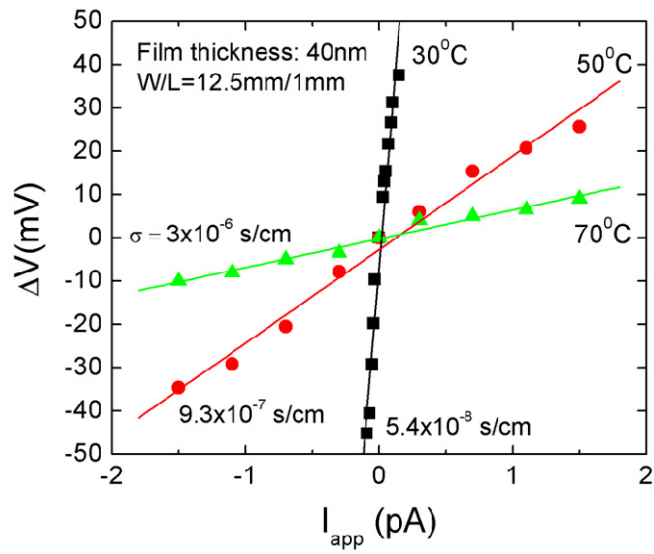


Fig. 6-4 Thermal conductivity of a-IGZO film

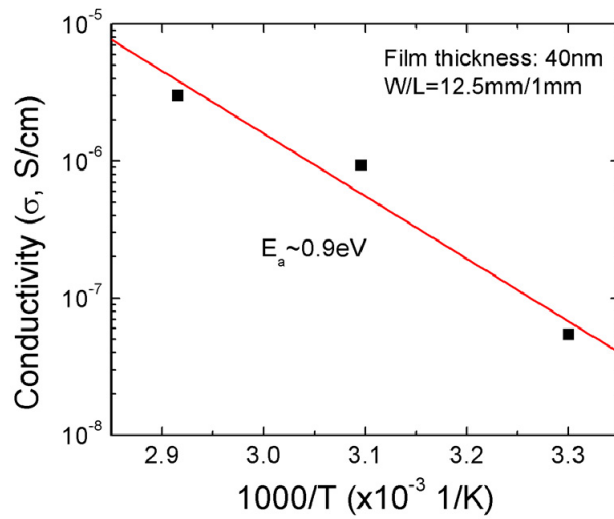


Fig. 6-5 Calculated activation energy

Conductivity of a-IGZO is proportional to the temperature. (Fig. 6-4) We got the conductivity 5.4×10^{-8} , 9.3×10^{-7} , and 2.0×10^{-6} S/cm for 30°C , 50°C , and 70°C , respectively from the equation as below.

$$\sigma = \left(\frac{\delta \Delta V}{\delta I_{app}} \right)^{-1} \left(\frac{L}{W \times t_{film}} \right) \quad \text{eq. (6-3)}$$

Activation energy of PLD a-IGZO film are also calculated as shown in Fig. 6-5. The slope of conductivity/(1/T) indicates that the activation of this film is around 0.9 eV. This means that the Fermi level could be around 0.9 eV lower than conduction band for this case.



● 6.3.3 TFT electrical properties

6.3.3.1 Dark

Before illumination, we characterized the a-IGZO TFT electrical properties in the dark. Device parameters are extracted by standard MOSFET drain current equations:

$$I_{DS} = \mu_{eff}^{lin} C_{ox} \frac{W}{L} \left(V_{GS} - V_{th} - \frac{V_{DS}}{2} \right) V_{DS} \quad \text{eq. (6-4)}$$

for linear region and

$$I_{DS} = \mu_{eff}^{sat} C_{ox} \frac{W}{2L} (V_{GS} - V_{th})^2 \quad \text{eq. (6-5)}$$

for saturation region. C_{ox} is the gate insulator capacitance per unit area,

μ_{eff}^{lin} and μ_{eff}^{sat} are the effective field-effect mobility, V_{TH} is the threshold voltage and

W and L are channel width and length of the TFT device, respectively.

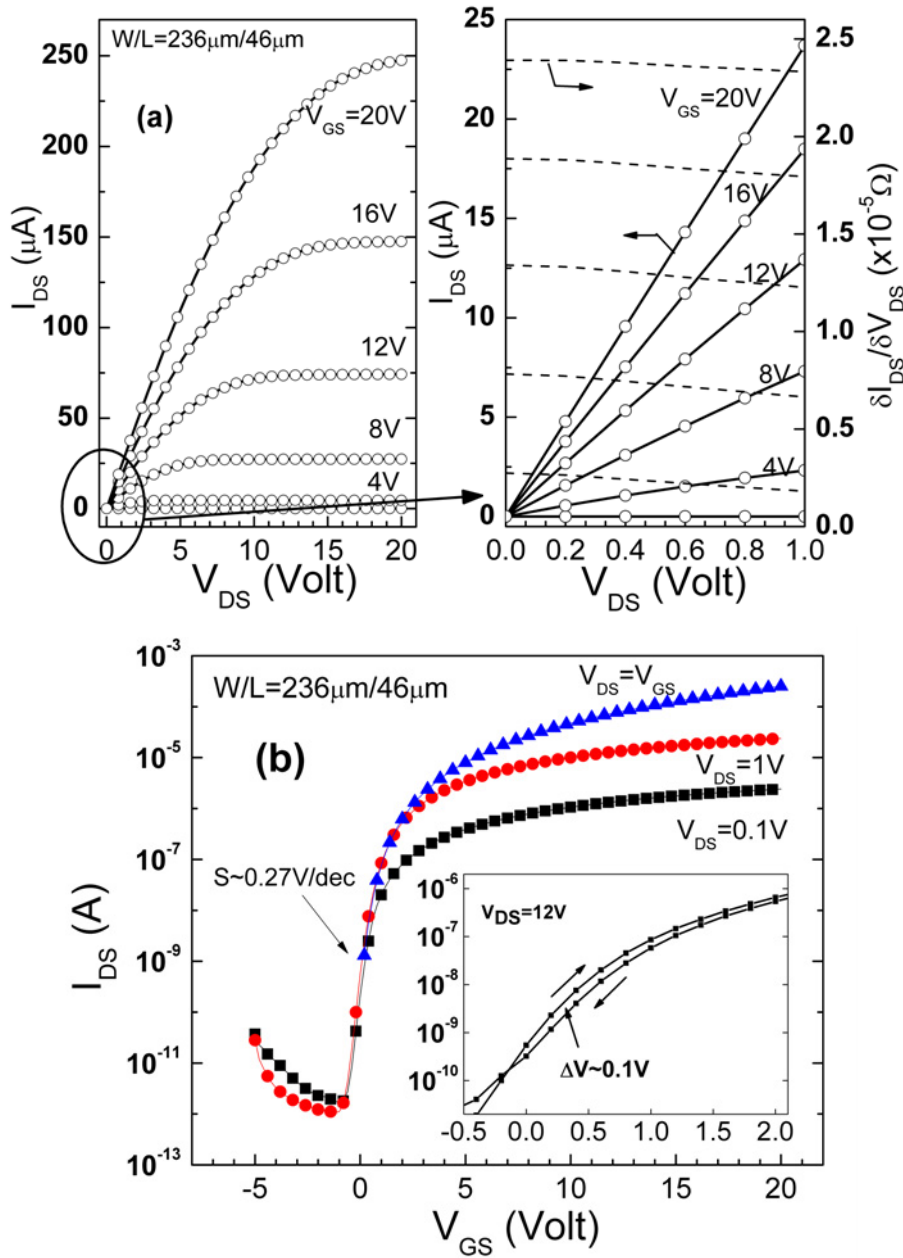


Fig. 6-6 (a) Dark I_{DS} - V_{DS} and (b) I_{DS} - V_{GS} characteristics of PLD a-IGZO TFT.

The typical extracted μ_{eff}^{lin} and μ_{eff}^{sat} from the TFT are 7.3 and 8.2 cm^2/Vs , respectively; V_{TH} value for linear regime is 2.13 V. It should be noted that field-effect-mobility seems to be W/L dependent. We also evaluated the TFT

subthreshold swing (S) between off- and on-states, using the following equation:

$$I_{DS} \propto 10^{V_{GS}/S} \quad \text{eq. (6-6)}$$

The TFT exhibits a good subthreshold swing (S) of 0.27 V/decade and a low off-state drain current (I_{DS-off} , below 1 pA). For comparison, we conveniently set the on-states drain current (I_{DS-on}) to be the drain current at $V_{DS}=V_{GS}=20V$. In general, PLD a-IGZO TFT shows good transistor behavior in both saturation regime and linear regimes of operation, Fig. 6-6(a). As can be seen in Fig. 6-6(b), the TFT dark on/off current ratio is larger than 10^8 with low hysteresis (inset of Fig. 6-6(b), $\Delta V \sim 0.1V$, where ΔV is the sub-threshold characteristic shift) during measurements.

6.3.3.2 Under illumination

The response of the PLD a-IGZO TFT to monochromatic illumination has been studied by measuring the TFT transfer characteristic for various light wavelengths. Fig. 6-7 shows the a-IGZO TFT transfer characteristic in the dark and under illumination. We observed clearly a shift in TFT electrical properties under illumination. Furthermore, a “threshold” wavelength exists when TFTs are illuminated, Fig. 6-7. In other words, little or no shift occurs in TFT properties under illumination with $\lambda > 420nm$ (2.95 eV) while a much larger change takes place when $\lambda < 420$ nm. As shown in Fig. 6-7(a) under illumination, TFT I_{DS-off} increases significantly as the illumination wavelength getting closer to UV region. Compare to the original dark condition, about three orders of magnitude increase occurs when we illuminated the device at $\lambda = 365$ nm (3.4 eV). In contrast with I_{DS-off} , the I_{DS-on} is rather constant. The onset of off-to-on V_{GS} voltage (or V_{TO}) also changes. Initially, the V_{TO} is very close to zero volts for TFT in the dark and a negative shift in V_{TO} is

observed during illumination; $V_{TO} \sim -7$ V was recorded for $\lambda = 365$ nm (3.4 eV). Finally, the off-to-on switching in I_{DS} becomes less steep when we illuminate the TFT under shorter wavelength. As consequence, the TFT subthreshold swing increases. In on-region, a negative shift of V_{TH} , similar to V_{TO} as shown in Fig. 6-7(b), is observed. The threshold voltage shift ($\Delta V_{TH} = V_{TH\text{-under illumination}} - V_{TH\text{-in dark}}$) was determined to be about negative 6 V under illumination at $\lambda = 365$ nm (3.4 eV). The slope of $\sqrt{I_{DS}} - V_{GS}$ shows almost no change within the wavelength range used in this study (Fig. 6-7(b)). This suggests the field-effect mobility (μ_{eff}) is not affected by illumination.

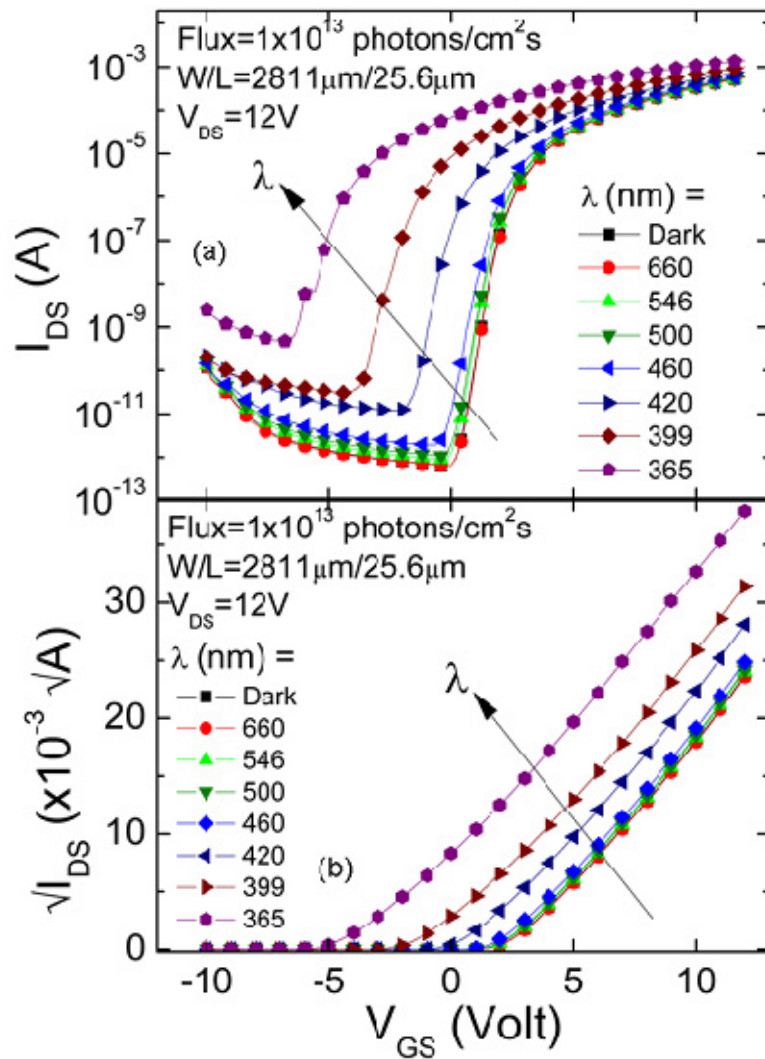


Fig. 6-7 $I_{DS} - V_{GS}$ curves for constant photo flux with the varying light wavelengths.

6.4 Discussion

We combined the light transmittance spectra of LCD color filter [80] and light emission spectra of the AM-PLED [81] in Fig. 6-8. Their maximum blue, green and red responses are about 450, 550 and 650 nm, respectively.

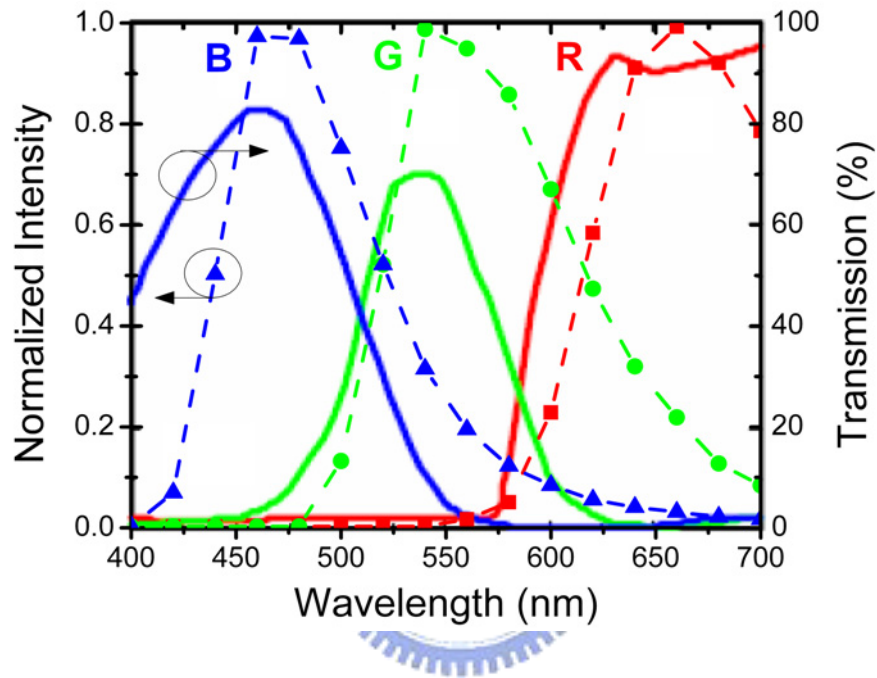


Fig. 6-8 Example of the color filter transmission spectra of the LCD (solid curves) and light emission spectra from multicolor PLED (symbol and dash curves).

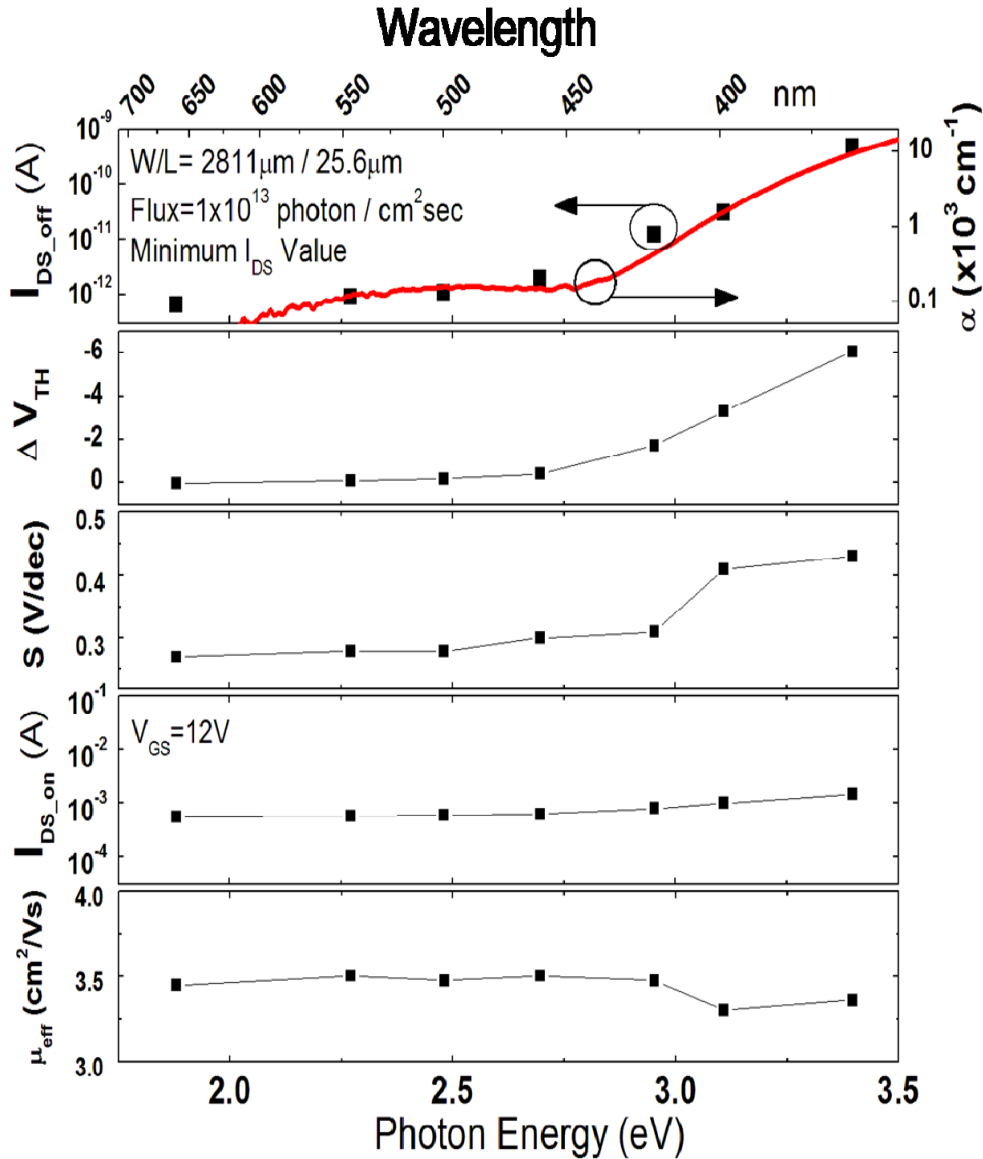


Fig. 6-9 Dependence of PLD a-IGZO TFT minimum off-state drain current (I_{DS-off}), on-state drain current (I_{DS-on}), threshold voltage shift (ΔV_{TH}), subthreshold swing (S), and field-effect mobility (μ_{eff}) on incident photons energy for constant photon flux.

From these figures, it is clear that the illumination wavelengths (365~660 nm) in this experiment do cover the photon energy range of interest to AM-LCDs and AM-OLEDs, and the optical band-gap of the a-IGZO (~410 nm). We summarize our results by plotting various TFT parameters as a function of incident photon energy (Fig. 6-9). By following eq. 6-3~ 6-5 and other definitions previously described in

section 6.3.2, TFT off-state drain current (I_{DS_off}), threshold voltage shift (ΔV_{TH}), subthreshold swing (S), on-state drain current (I_{DS_on}) and μ_{eff} are extracted and shown in Fig. 6-9.

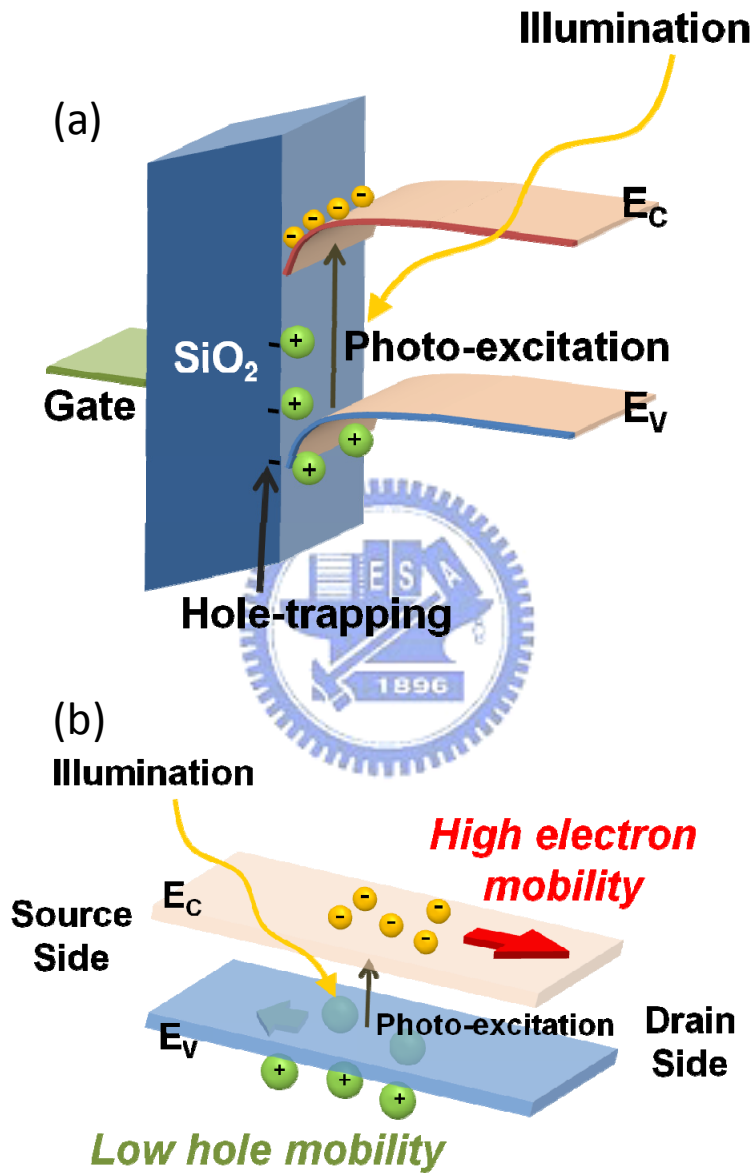


Fig. 6-10 (a) Band diagram of a-IGZO TFT operated under illumination (b) closer look at the channel region

In the order to elucidate the physical origin of the shift in TFT electrical properties, the a-IGZO absorption spectrum (solid curve) is overlapped with the

variation of the I_{DS_off} data in Fig. 6-9. It can be concluded that the light with energy less than 3.0 eV (visible region) is only weakly absorbed and has a negligible effect on the TFT transfer characteristics, while light with energy larger than 3.0 eV is strongly absorbed and is expected to generate a large density of electron-hole pairs that are separated in the device channel. During illumination, the threshold voltage (V_{TH}) shifts to more negative V_{GS} values with the increasing photo energy, indicating that the holes are trapped (positive space charge) within the channel or/and at the $SiO_2 / a\text{-IGZO}$ interface, e.g., electrons appears to be more mobile than holes in a-IGZO TFTs (Fig. 6-10(a)). The TFT I_{DS_off} , ΔV_{TH} , and subthreshold swing (S) are increasing with the increasing film absorption coefficient. After illumination, we can bring the device back to its original pre-illumination state by a 100°C thermal treatment for 3 min. With no applied heat, the device will regain its pre-illumination properties after a much longer period of time. Since this is a fully reversible process, the photogenerated carriers (holes) are most likely trapped during photo-generation process. Electrons appear to have higher mobility than holes (Fig. 6-10(b)). The exact nature of the traps is under present investigation.

6.5 Conclusion

In conclusion, we have shown that the a-IGZO TFTs off-state drain current, subthreshold swing, and V_{TH} shift under illumination follows material optical absorption spectrum. The a-IGZO TFT is stable under visible light illumination while electrical properties start to change when the illuminating photon energy is approaching or is above its absorption gap energy ($\sim 3\text{eV}$, near-UV region) The illuminated devices can be return to their initial dark state after just short thermal treatment at higher temperature. This study indicates how the a-IGZO TFTs

photosensitivity could affect active-matrix LCDs and OLEDs, and photo-sensors operation. May be light shield electrodes used in a-Si:H TFT AM-FPDs or photo-imagers could be avoided when a-IGZO TFTs are used.



Chapter 7

2-D Numerical simulation of RF sputter amorphous In-Ga-Zn-O TFTs

7.1 Introduction

Over the past few years, there is an increasing interest in using amorphous In-Ga-Zn-O thin-film transistors (a-IGZO TFTs) to replace a-Si:H TFTs for next generation flat-panel displays. There are many unique advantages of adapting a-IGZO as channel layer such as high carrier mobility, visible light transparency and the capability of large area deposition at low processing temperature [51]. Many research efforts focused on developing proper processing approaches and optimizing thin-film deposition conditions. RF magnetron sputtering and pulse laser deposition (PLD) are two main techniques that have been reported for depositing a-IGZO thin film. TFTs made by these two methods with high field-effect mobility (μ_{eff}) and good switching properties have also been reported by several groups [82- 86]. For commercial integrated circuit or display applications, sputtering could be more promising due the easy of integration with existing processing facilities [84,87].

In a-Si:H TFT research, physics-based numerical simulation has been a powerful tool for engineer to understand the device operation and optimizing of its electrical performance and structure [88]. Despite all the success in device fabrication, there is lack of similar study for a-IGZO TFT. To bridge such technological gap, we report in this paper the latest results on a-IGZO TFTs 2-D simulation based on proposed density-of-states (DOS) model to describe electronic properties of the RF sputter

a-IGZO thin-film.

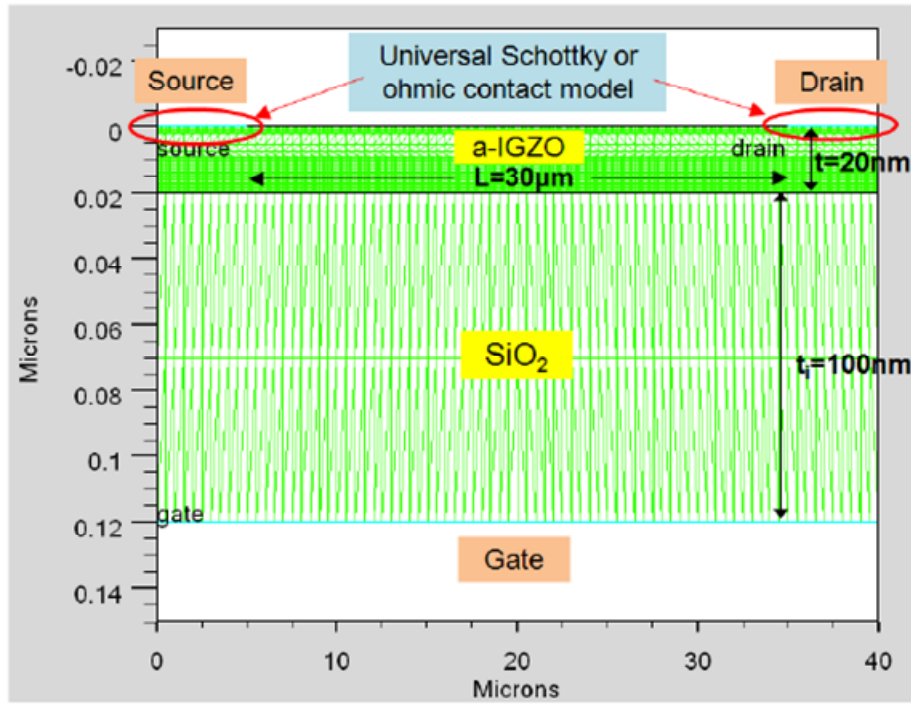


Fig. 7-1 Cross-sectional view of inverted-staggered a-IGZO TFT

7.2 Simulation

We first construct the device structure which represents the RF sputter a-IGZO TFT used in this study [89]. A 2-D, inverted-staggered a-IGZO TFT structure used for numerical simulation is shown in Fig. 7-1. The structure consists of a 20nm thick a-IGZO channel layer and a 100nm thick SiO₂ gate insulator layer. The TFT channel length (L) is 30µm. To facilitate the finite element analysis, the 2-D structure is further decomposed into smaller mesh structures. The spaces (or resolution) between grid points for different regions were optimized for computing time and best fit to experimental data; denser grid points are placed near the source/drain contacts and interface between a-IGZO and gate insulator. The contacts between source/drain electrodes and a-IGZO channel are either assigned as Schottky or ohmic in nature in this work.

To develop the proper DOS model, we referred to several published results. Takagi *et al.* have extracted the conduction band effective mass (m_c) to be $\sim 0.34 m_e$ (m_e is the mass of free electron) in their early work on a-IGZO [90]. We further calculated the effective conduction band density of states (N_c) to be $5 \times 10^{18} \text{ cm}^{-3}$ [91].

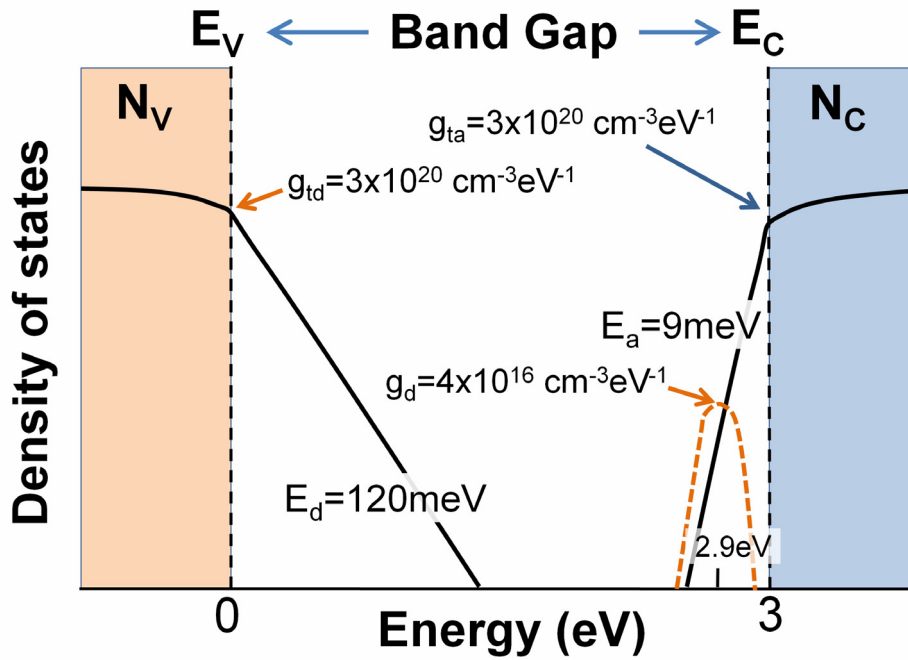


Fig. 7-2 Propose density-of-states (DOS) model for a-IGZO. E_C and E_V are conduction and valence band-edge energy, respectively. Solid curves within band-gap represent the exponentially-distributed band tail states (g_{CBa} , g_{VBd}), while the dash curve near the conduction band-edge represents the Gaussian-distributed donor-like oxygen vacancy states (g_{Gd}).

The increasing structural disorder within amorphous material can induce electron scattering and eventually localized wave-functions. Such phenomenon can be approximately represented as localized tail states within band gap, near the band edges. In this study, band tail states of a-IGZO are represented as a function of energy (E) by following expressions (Fig. 7-2):

$$g_{CBa} = g_{ta} \exp((E - E_C)/E_a) \quad \text{eq. (7-1)}$$

$$g_{vBd} = g_{td} \exp((E_V - E)/E_d) \quad \text{eq. (7-2)}$$

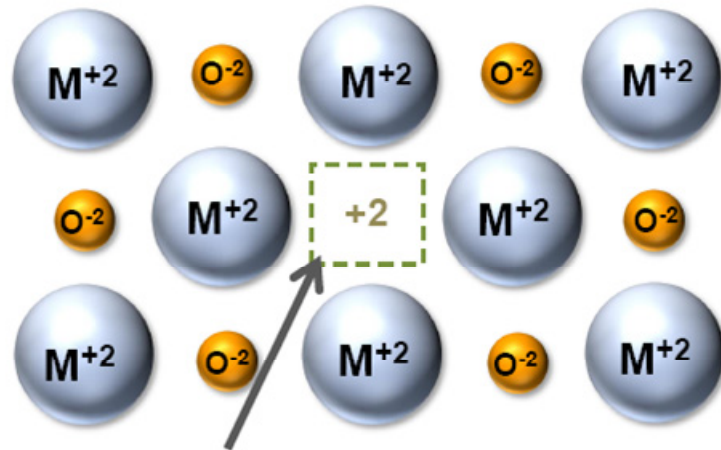
where E_C and E_V are conduction and valence band edge energy, g_{ta} and g_{td} are density of acceptor and donor like states at $E=E_C$ and $E=E_V$, respectively, and E_a and E_d are characteristic slopes of conduction and valence band tail states, respectively [88]. To determine the proper range for g_{ta} , we considered the fact that the DOS has a continuous distribution from tail states to extended states. Therefore, it is reasonable for N_C (or N_V) and g_{ta} (or g_{td}) to have a proportional relation. Since N_C of a-IGZO is about an order smaller than a-Si:H (N_C for a-Si:H is $\sim 3 \times 10^{19} \text{ cm}^{-3}$), we assume g_{ta} of a-IGZO should be around $10^{20} \text{ cm}^{-3} \text{ eV}^{-1}$ (g_{ta} for a-Si:H is $10^{21} \text{ cm}^{-3} \text{ eV}^{-1}$ [88]). The band gap (E_g) and valence-band-tail slope (E_d) were further determined by optical absorption measurement on a-IGZO thin film [92].



It is well known that due to the unique conducting mechanism through metal ion's spherical s-orbital, band conduction can still exist in a-IGZO TFT even it is an amorphous phase. Therefore, we set the electron band mobility (μ_n) to be the maximum differential mobility ($\mu_{\text{diff-MAX}}$) obtained from TFT measurement (in this study, its $15 \text{ cm}^2/\text{Vs}$). Oxygen vacancies can also alter the electrical properties of oxide semiconductors (Fig.6-3). It is commonly believed that the vacancies created additional states near the conduction-band edge (CBE) [93,94]. We include a Gaussian-distributed donor-like state located near the CBE to phenomenologically model the oxygen vacancies in oxide semiconductor with equation:

$$g_{Gd} = g_d \exp(-(E - \lambda)^2 / \sigma^2) \quad \text{eq. (7-3)}$$

where g_d , λ and σ are peak value, mean energy and standard deviation of states, respectively. The schematic of the proposed DOS model is illustrated in Fig. 7-2 and this model is further supported by independent simulation and experiments results.



- Oxygen vacancy is effectively “positive charged” indicated a donor-like behavior

Fig. 7-3 Oxygen vacancy in oxide semiconductor

Table 7-1 Key simulation parameters used in this study

Symbol	Value	Unit	Description
N_c	5×10^{18}	cm^{-3}	Effective conduction band DOS
N_v	5×10^{18}	cm^{-3}	Effective valence band DOS
g_{ta}	3×10^{20}	$\text{cm}^{-3} \text{eV}^{-1}$	Density of tail states at $E=E_c$
g_{td}	3×10^{20}	$\text{cm}^{-3} \text{eV}^{-1}$	Density of tail states at $E=E_v$
E_a	9	meV	Conduction-band-tail slope
E_d	120	meV	Valence-band-tail slope
E_g	3.05	eV	Band gap
Φ	4.3		Electronic affinity
ϵ	10		Permittivity
μ_n	15	cm^2/Vs	Band mobility (electron)
μ_p	0.1	cm^2/Vs	Band mobility (hole)
m_c	0.34	m_e	Conduction band effective mass
g_d	4×10^{16}	$\text{cm}^{-3} \text{eV}^{-1}$	Peak of oxygen vacancy (OV) states
λ	2.9	eV	Mean energy of OV states
σ	0.1	eV	Standard deviation of OV states

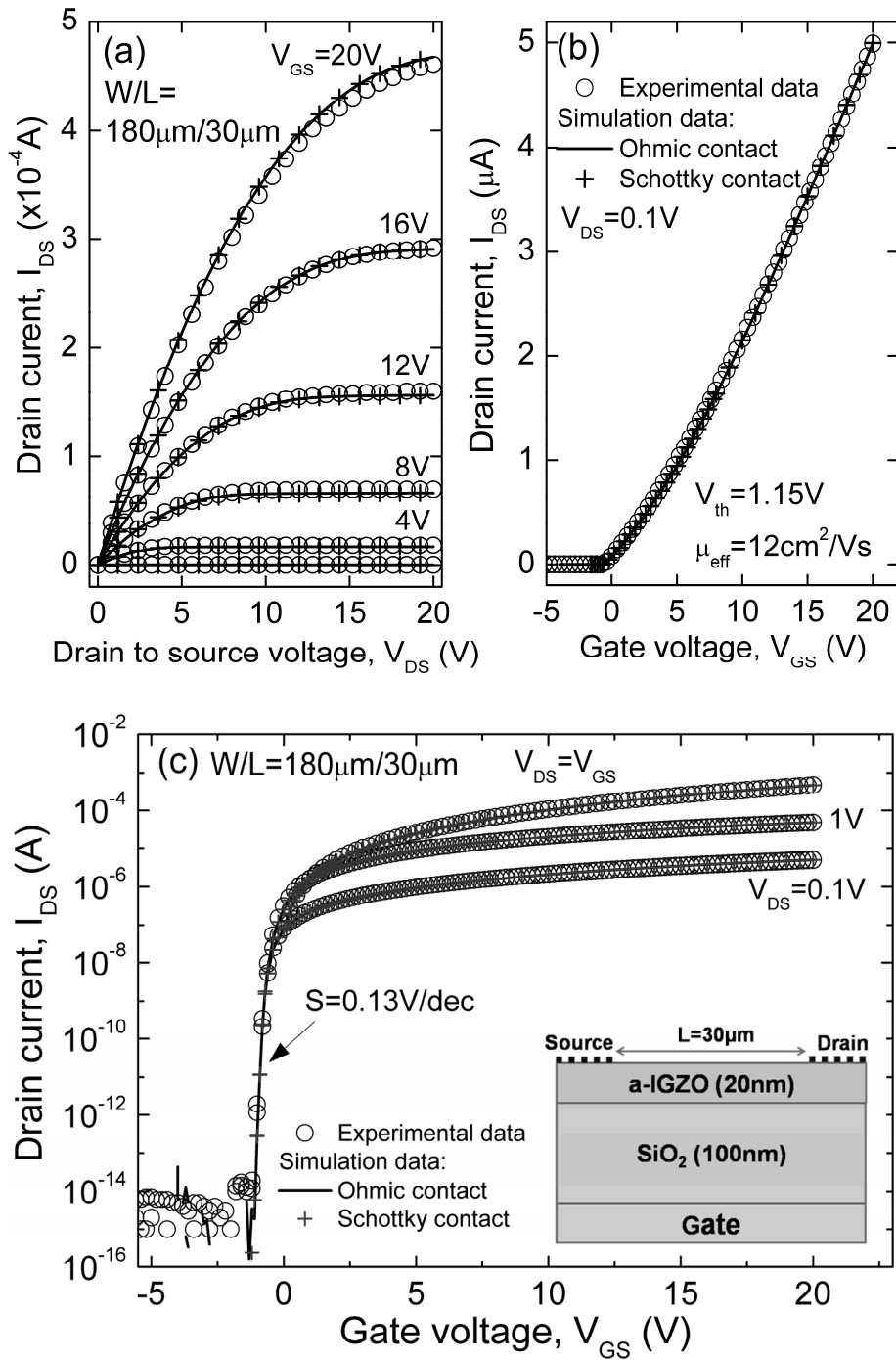


Fig. 7-4 (a) Output and (b)(c) transfer characteristics for a-IGZO TFT ($W/L=180\mu\text{m}/30\mu\text{m}$). Both experimental (\circ) and simulation data (solid line: ohmic contact; +: Schottky contact) are presented. Extracted threshold voltage (V_{th}), field-effect mobility (μ_{eff}) and sub-threshold swing (S) are also indicated. Inset of (c): TFT structure used in simulation.

7.3 Result and Discussion

All the parameters are then inputted into the simulation software [95] that was modified for this study. The final set of parameters optimized for our a-IGZO TFT are listed in Table I. Results show that our physics based model can reproduce with a very highly accurate output, transfer and sub-threshold a-IGZO TFT experimental characteristics (Fig. 7-4). It is worth to notice that the final E_a we obtain (9 meV) is lower than common a-Si:H value (~25meV) and agree fairly well with what Kamiya *et al.* predicted in their original work [94]. This result also support the fact that the conducting mechanism between a-IGZO and a-Si:H are fundamentally different [51]. We speculate our RF sputter a-IGZO has sufficient metal s-orbital overlap allowing the electrons to have a nearly “scattering free” conduction. In comparison, the directional Si sp^3 bonds are inevitably distorted under amorphous phase. As a result, a-IGZO can have a much sharper conduction band-tail distribution than a-Si:H. Both Schottky and ohmic contact models have been considered, and give similar simulation results. This suggests that the S/D metal (in this study, it's Ti) is forming an ohmic-like contact with the a-IGZO layer. In summary, the RF sputter a-IGZO TFT we used in this study has the following properties: $\mu_{\text{eff}} = 12 \text{ cm}^2/\text{V}\cdot\text{s}$, threshold voltage (V_{TH})=1.15V, sub-threshold swing (s)=0.13V/dec, off-current (I_{off}) $< 10^{-14}$ and on/off ratio $\sim 10^{10}$.

We further utilized this model to investigate impacts of the S/D series resistance ($R_{\text{S/D}}$) and DOS properties on TFT performance. During the numerical simulation, $R_{\text{S/D}}$ values were varying from 0~30 k Ω in a logarithmic increment. Based on experimental results, we approximated the $R_{\text{S/D}}$ for our a-IGZO TFT to be less than 300 Ω (Fig. 7-5(a)). Also conduction band tail slop (E_a) was changed from 5~20 meV. Our results clearly indicated that a larger E_a (shallower tail state distribution) can

increase V_{TH} and also degrade the maximum μ_{eff} which TFT can achieve (Fig. 7-5(b)).

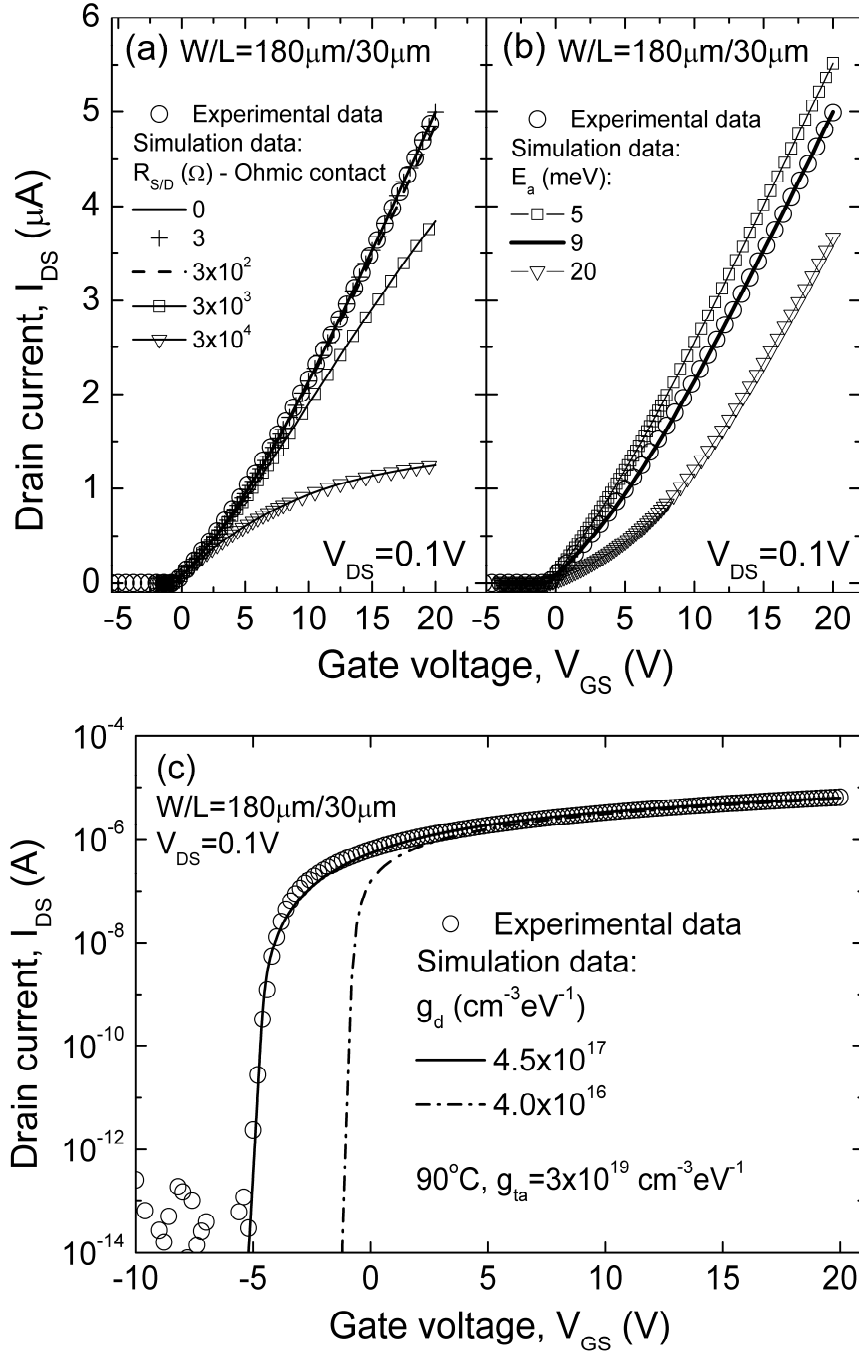


Fig. 7-5 Simulated I_{DS} - V_{GS} curves of a-IGZO TFT in linear region (Drain to source voltage, $V_{DS}=0.1\text{V}$) for various (a) source / drain contact resistance ($R_{S/D}$) and (b) conduction band tail slope (E_a). (c) Example of using oxygen vacancy states (g_{Gd}) to simulate a-IGZO TFT shifting behavior at high temperature. Real experimental data (\circ) are also shown as reference.

On another a-IGZO TFT (with lower g_{ta} value), we measured the electrical properties at a high temperature (90°C) and observed a shift in turn-on voltage (V_{TO}). Since there is no electrical stressing involved, it is more reasonable assuming that the physical origin of such shift is due to increasing oxygen vacancies (OV) in a-IGZO at the higher temperature. Fig. 7-5(c) shows that our model can simulate such observation by increasing OV states (g_{Gd} , eq.(7-3)). Compare to the conduction band-tail states (g_{CBa}), the increase of g_{Gd} is relatively small and doesn't alter the sub-threshold swing significantly. However, these OV states are effectively ionized during the pre-threshold state of the TFT operation and induce the observed shift in V_{ON} . Furthermore, we can also use OV states to explain why V_{TH} shift to negative value if lacking of oxygen in a-IGZO film during processing.

7.4 Conclusion

We demonstrated the results on two-dimensional (2-D) simulation of high performance amorphous In-Ga-Zn-O (a-IGZO) TFTs for flat panel displays. Our RF sputter a-IGZO TFT has following properties: field-effect mobility (μ_{eff})= $12\text{cm}^2/\text{Vs}$, threshold voltage (V_{TH})= 1.15V , sub-threshold swing (S)= $0.13\text{V}/\text{dec}$ and on/off ratio over 10^{10} . A density-of-states model is developed, to accurately simulate the measured transistor properties. The donor-like oxygen vacancy states are also included to simulate the high temperature TFT behavior. The results show that RF sputter a-IGZO TFT has very sharp conduction band-tail slope distribution ($E_a=9\text{meV}$) and ohmic like source / drain contact which can be the physical origin of the high performance we observed. Such device is very desirable for a high resolution flat panel displays.

Chapter 8

Ambipolar TFTs and CMOS-like inverter

8.1 Introduction

Recently, we combined pentacene and a-IGZO these two active materials into one TFT devices. These TFTs which show both p-type and n-type characteristics, they are called ambipolar TFTs as shown in Fig. 8-1. There are several objectives of ambipolar TFTs, including the simplification of the process and circuit design, the elimination of the problem to choose between n-type and p-type TFT before fabricating, also the acquisition of the characteristics under both positive and negative bias. Stability in ambience air is the critical issue of OTFTs at present. For n-type organic materials, electron channel can not be formed stably in ambience so that the TFTs show only p-type characteristics. The characteristics of ambipolar TFTs was measured in inert gas environment in most previous works [96-99]. Stability has always been an important issue for these ambipolar TFTs.

8.2 Latest results

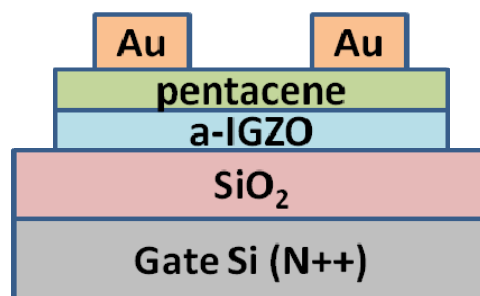


Fig. 8-1 Cross-sectional view of proposed ambipolar TFT

We used pentacene/a-IGZO to fabricate devices which can be operated stably in ambient air. Fig. 8-2 illustrates the I_{DS} - V_{DS} curves of our ambipolar TFT. It shows both p-type and n-type behavior.

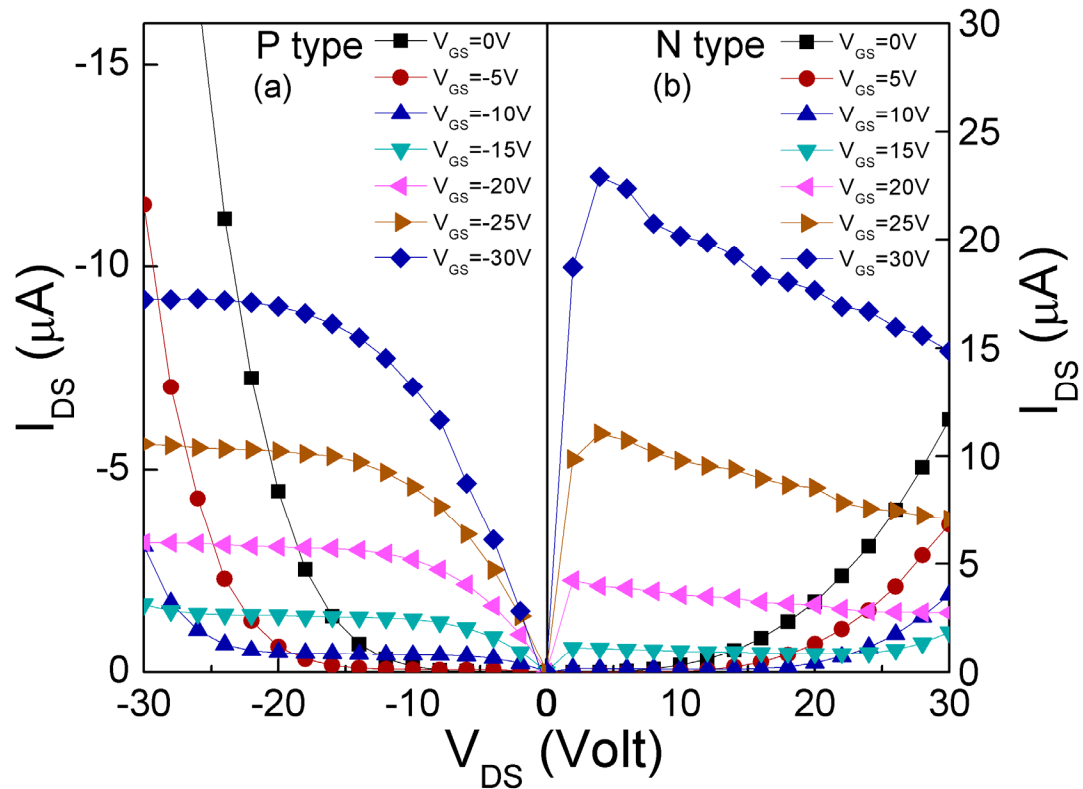


Fig. 8-2 I_{DS} - V_{DS} curves of ambipolar TFT

We also measured the I_{DS} - V_{GS} curves of the ambipolar TFT. On/off current ratio is decreased when V_{DS} is increased. Take n-type operation for example, when $V_{DS} > V_{GS}$, holes are induced and injected into active layer due to electric field between gate and drain electrode. (Fig. 8-3)

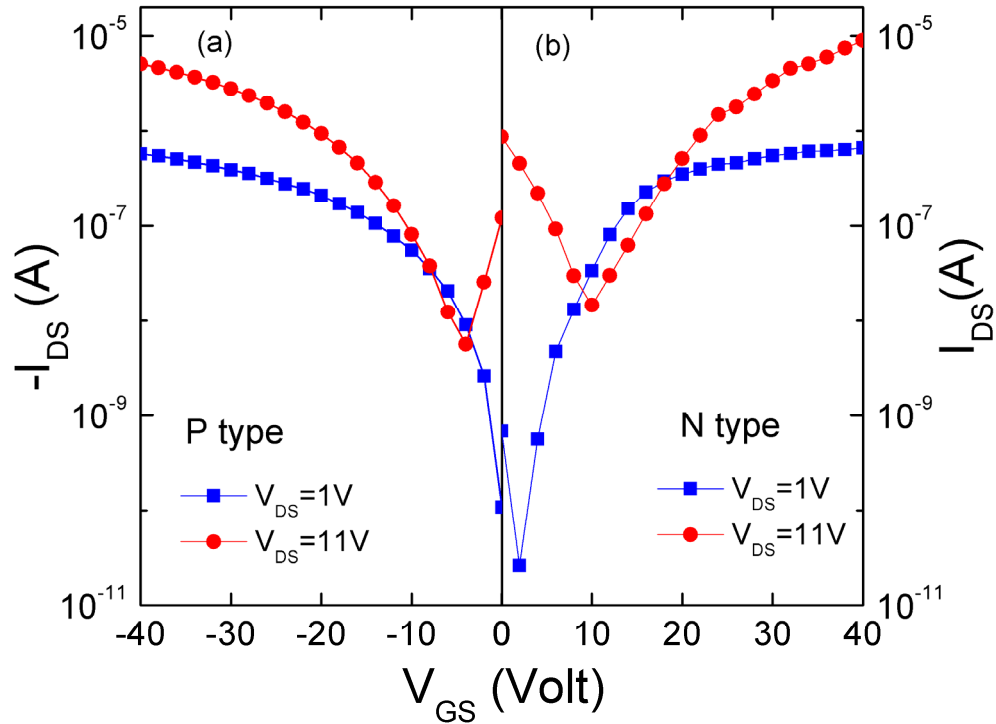


Fig. 8-3 I_{DS} - V_{GS} curves of ambipolar TFT

The most advantage of ambipolar TFTs application is inverter. Traditional CMOS inverter composes of a NMOS and a PMOS device. For our study, we connect 2 identical ambipolar TFTs as CMOS-like inverter. The cross-sectional view of this CMOS-like inverter and schematic circuit are shown in Figs. 8-4 (a) and (b). In the inverter circuit, the gate is common for both transistors and serves as an input node (V_{in}). When the supply voltage V_{DD} and the input voltage V_{in} are biased positively, the inverter function in the first quadrant, and the output voltage V_{out} versus input voltage V_{in} plot exhibits a gain of 62. When V_{DD} and V_{in} are negative, the inverter exhibited a gain of 43 in the third quadrant as shown in Fig. 8-5.

Unlike conventional CMOS inverter, our CMOS-like inverter can be operated in 2 quadrants. It is because the ambipolar TFTs have both n-type and p-type behavior. This makes the circuit design simpler, and can be adopted for display circuit applications.

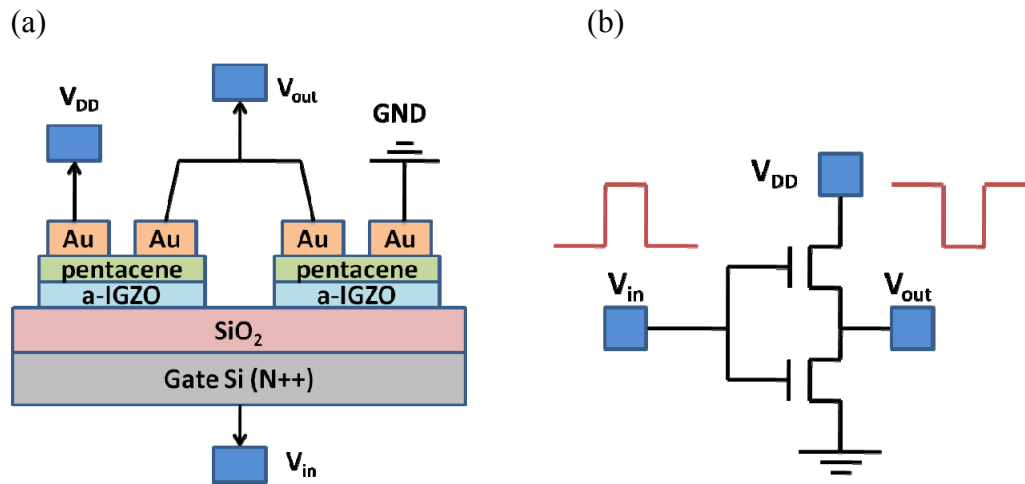


Fig. 8-4 (a) Cross-sectional view of CMOS-like inverter (b) Schematic circuit of CMOS-like inverter

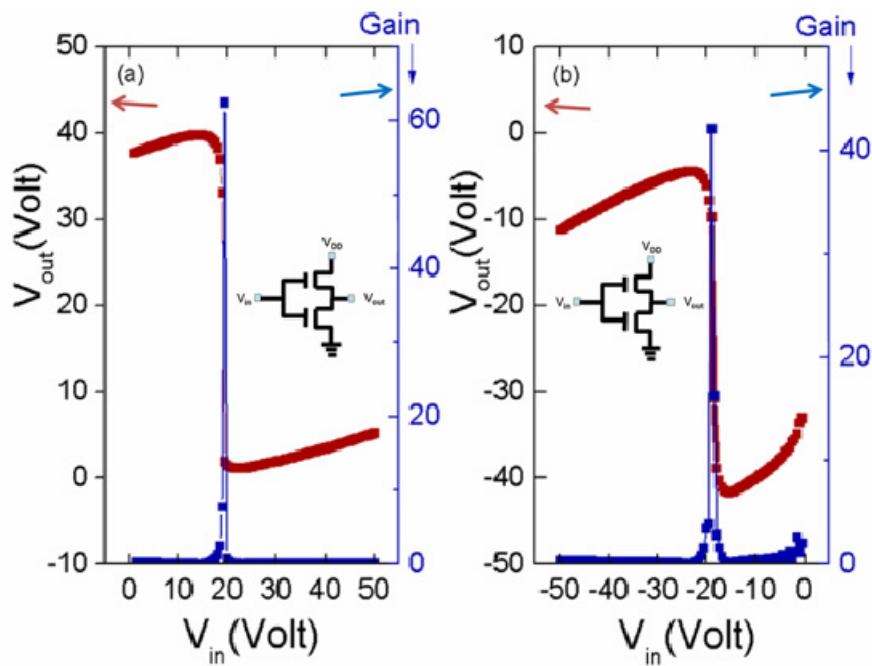


Fig. 8-5 Voltage transfer curve and their corresponding gains of ambipolar TFTs operated in the (a) first quadrant and (b) third quadrant

In conclusion, this work combines the pentacene and a-IGZO TFTs together, which have been studied in the previous chapter. Both n channel and p channel behaviors of these ambipolar TFTs were analyzed together with their corresponding

inverter circuits. We have to do further optimization regarding the TFT and inverter parameters. Overall, a-IGZO/pentacene exhibits an ambipolar behavior with high voltage gain value and qualifies themselves as promising candidates for the applications in AMFPDs.



Chapter 9

Conclusion and Future Work

9.1 Conclusion

We first aimed to improve the performance of pentacene TFTs. By blending TiO₂ nanoparticles, we successfully reduced the operating voltage and suppressed their photosensitivity. TiO₂ nanoparticles not only serve as high κ material to produce more field-effect carriers but also act as recombination centers between the energy gap of pentacene to eliminate the electron-hole pairs. Furthermore, we also made transparent and flexible OTFTs using colorless PVP polymer and transparent metal-oxide hole injection layer.

Additionally, we used different gate dielectric materials to show the potential applications of OTFTs such as the color-filtering function. We integrated color filter into gate dielectric layer and further improved by utilizing colored PMMA as gate insulator. This unique material can provide good insulating and color-filtering function.

We also studied the fundamental intrinsic properties of a-IGZO TFTs. We found that a-IGZO TFTs are stable under visible light illumination and electrical properties start to change when the photon energy is over 3 eV. Besides, oxygen vacancy donor-like states were first proposed in the simulation, and the results are well agreed with experimental data.

Finally, we got latest results regarding to combine pentacene/a-IGZO bi-layer as ambipolar TFTs. These ambipolar TFTs can be a CMOS-like inverter circuit. By using ambipolar TFTs, we can simplify the circuits and minimize the power

consumption comparing to use N-type TFTs as inverters. The contributions of this dissertation are: (1) We minimize several issues of pentacene based TFTs and demonstrate the functionality of OTFTs such as color-filtering and memorable. (2) In the leading group regarding to the a-IGZO TFTs related studies such as photosensitivity and simulation/modeling.

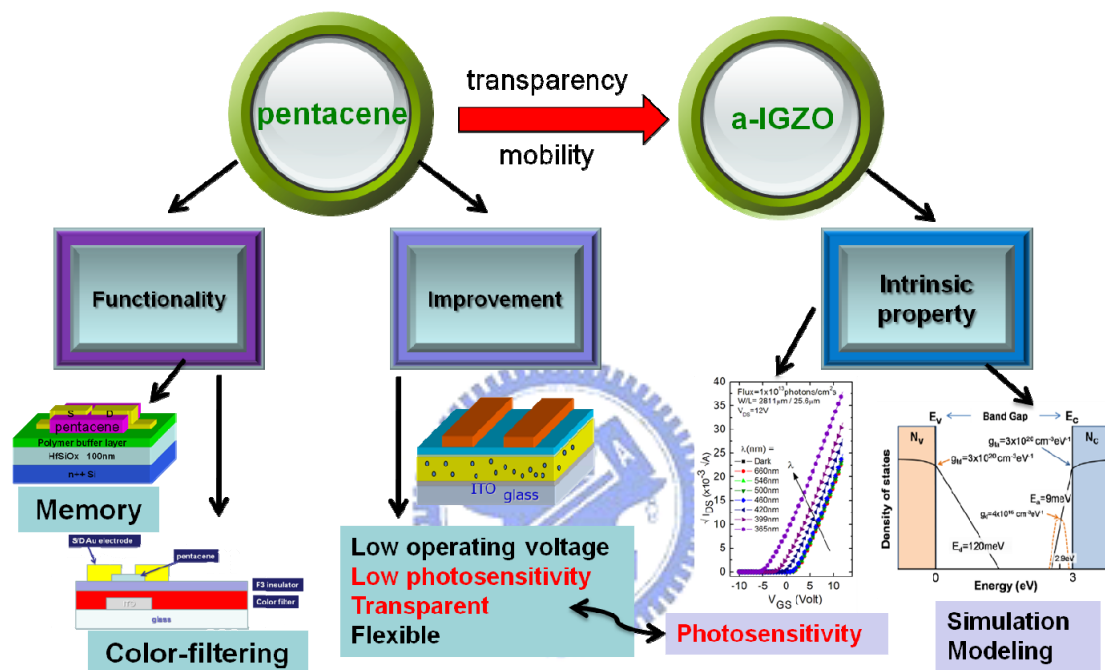


Fig. 9-1 Research projects in this study

9.1.1 Organic Thin-film transistors with polymeric nanocomposite dielectrics

High performance OTFTs incorporated with high dielectric nanoparticles in the dielectric layers have been demonstrated. The dielectric insulator consists of cross-linked PVP and TiO₂ nanoparticles. The dielectric constants values of different percentages TiO₂ blended into PVP agrees well with theoretical models. This proves the trustworthiness of our results. In order to obtain highly soluble TiO₂ nanoparticles in organic solutions, the surface of nanoparticles was modified with

organosiloxane. Moreover, the concern of higher leakage current, while using the high dielectric nanocomposite insulators, has been overcome by further applying another PoMS layer. As a result, we have demonstrated low-voltage OTFTs, which can be operated within 10 V. Table 8.1 illustrates some high κ gate insulators utilized in OTFTs. From the comparison, our study can offer a simpler way to make the high κ composite gate insulator by solution processes compared to ours by sputtering and anodization. Finally, we successfully made the OTFT on the flexible substrates with mobility $\sim 0.1 \text{ cm}^2/\text{Vs}$.

Table 9-1 Summary & comparison for high κ gate insulator in OTFTs

High κ OTFTs Comparison	SCIENCE 1999 Vol. 283, 822 IBM	Adv. Mater. 2005 Vol. 17, 192 U. of Sheffield (UK)	Org. Electron. 2006 Vol. 7, 435 NCTU
Active layer	pentacene	pentacene	pentacene
Insulator	BZT (BaZrTi)	TiO ₂ /PaMS	PVP/TiO ₂
Dielectric constant	16	23	10.5
Deposition method	Sputtering	Anodization	Solution
Mobility	0.32	0.8	0.4
On/off ratio	$\sim 10^5$	$\sim 10^4$	5×10^4
Operation voltage	10 volt	1 volt	10 volt
Process	Complex	Difficult	Easy

9.1.2 Organic thin-film transistors with reduced photosensitivity

Organic thin-film transistors with a minimal threshold voltage shift and a more stable photocurrent under illuminated conditions can be made by embedding TiO₂ nanoparticles into a polymer dielectric layer. While the studies of pentacene morphology using atomic force microscopy and X-ray diffraction have shown similar results before and after embedding the TiO₂ into the dielectric layer, we have found that the presence of TiO₂ nanoparticles is essential. The reduced

photosensitivity, be attributed to the recombination centers induced by the TiO₂ nanoparticles, can enhance substantially the recombination process of the electrons trapped in the channel.

Not only the photosensitivity respect to white illumination has been reduced, a high transpance has also been achieved simultaneously. MoO₂ was utilized as the hole injection layer, resulting in work function matching with pentacene when ITO was used as the source/drain electrodes. For the device with TiO₂ nanoparticles, the transmittance decreased slightly due to the light-scattering from the nanoparticles. However, the average transmittance reminded as high as 54%. Hence, the photosensitivity of pentacene based OTFTs was resolved effectively and could be used in active driving circuits without the noticeable V_{th} shift.

9.1.3 Color filtering functional organic thin-film transistors

We developed color filtering functional organic thin-film transistors exhibiting both high field-effect mobilities and color-filtering ability. The conventional colorant inks were utilized as the materials for the color filter/dielectric multifunction layers. In order to improve the electrical performance, a high dielectric polymeric insulator, PTFMA, was introduced to modify the surface of the dielectric layer. Further, the Commission Internationale de L'Eclairage chromaticity coordinates were (0.64, 0.34), (0.36, 0.54), and (0.14, 0.15) for red, green, and blue devices, respectively, covering 49.2% National Television Systems Committee (NTSC) standard. This work represents one potential application for multifunctional organic electronics.

Furthermore, we utilized colored PMMA as the materials for the color filter/dielectric multifunction layers of the TFTs. The main advantage of this method is the colorful layer is unique, no phase separation issue compared to the blending or

bi-layer structures. The colored TFTs showed the mobilities around $0.13 \text{ cm}^2/\text{Vs}$, threshold voltage -9.02 V , and sub-threshold swing 1.35 V/decade with color coordinate CIE1931 (0.409, 0.454). The electrical performance and film morphology is similar to traditional PMMA insulator device. Compared to traditional color filter on array method, our color PMMA (colorful insulator) shows an easy way and potentially material high utilization, as shown in Table 8.2. This work was successfully integrated gate insulator and color filter, which offered an ink-jet printing compatible process for cost-effective fabrication of display system.

Table 9-2 Summary & comparison for color-filtering OTFTs

Color filter integration Comparison	Traditional Color filter on array	APL 2008 Vol. 93, NCTU	IDMC 2007 Thu-P1-22 NCTU
Method	COA	CF in GI	Color PMMA
Color filter ink	○	○	×
IJP comparable	○	○	○
Integrated gate dielectric	×	○	○
Process	complicate	simple	simple
Cost	high	low	lowest

9.1.4 Photosensitivity of amorphous In-Ga-Zn-O thin-film transistors

To develop a-IGZO density-of-states model, intrinsic a-IGZO optical properties such as optical band gap and Urbach energy, and TFT characteristics under illumination were investigated. During the a-IGZO TFTs illumination with the wavelengths ranging from 460 to 660 nm, the off-state drain current only slightly increased while a large increase was observed for the wavelength below 400 nm.

Threshold voltage and subthreshold swing were also only slightly modified between 460 to 660 nm, while field-effect mobility was almost unchanged in the photon energy range investigated. The observed results are consistent with the a-IGZO optical energy band gap of about 3.05 eV. This study suggests that the a-IGZO TFTs are light sensitive above 3.0 eV and photogenerated electrons are more mobile than holes within device channel region. Table 9.3 shows our results, as compared to SONY's study [100].

Table 9-3 Summary & comparison for photosensitivity study for a-IGZO TFTs

Photosensitivity Study comparison	SID 2008 P.13 NCTU/U. of Mich.	AMFPD 2008 Sec. 7-2 SONY
Active layer	a-IGZO (PLD)	a-IGZO (sputtering)
Insulator	SiO ₂	SiO ₂
Mobility (cm ² /Vs)	8.2	20
On/off ratio	10 ⁹	10 ⁹
Wavelength	○	○
Intensity	○ (IDMC'08)	×
V _{th} shift mechanism	Hole trap	← same
Recover method	Anneal	← same

9.1.5 2-D Numerical simulation of RF sputter a-InGaZnO TFTs

We reported the latest results on two-dimensional (2-D) simulation of high performance amorphous In-Ga-Zn-O (a-IGZO) TFTs for flat panel displays. Our RF sputter a-IGZO TFT has following properties: field-effect mobility (μ_{eff})=12cm²/Vs, threshold voltage (V_{TH})=1.15V, sub-threshold swing (S)=0.13V/dec and on/off ratio over 10¹⁰. A density-of-states model is developed, to accurately simulate the

measured transistor properties. The donor-like oxygen vacancy states are also included to simulate the high temperature TFT behavior. The results show that RF sputter a-IGZO TFT has very sharp conduction band-tail slope distribution ($E_a=9\text{meV}$) and ohmic like source / drain contact which can be the physical origin of the high performance we observed. Table 9.4 is the summary and comparison for modeling and simulation of a-IGZO TFTs [100].

Table 9-4 Summary & comparison for modeling and simulation of a-IGZO TFTs

Simulation/modeling comparison	APL 2008 Vol. 92, 133503 NTU	AMFPD 2008 P.29 NCTU/U. of Mich.
Active layer	a-IGZO (PLD)	a-IGZO (sputtering)
Insulator	SiO ₂	SiO ₂
Mobility (cm ² /Vs)	7.84	12
On/off ratio	10 ⁹	10 ¹⁰
Software	Silvaco	Silvaco
Model	a-Si modified	a-Si modified + oxygen vacancy
Vth shift mechanism	Traditional	OV state proposed
Fitting	good	excellent

9.1.6 Ambipolar TFTs and CMOS-like inverter

We have fabricated ambipolar TFTs through a hybrid route by combining organic/oxide semiconductors. Both n channel and p channel behaviors of the ambipolar TFTs were analyzed together with their corresponding inverter circuits. Overall, a-IGZO/pentacene exhibits an ambipolar behavior with balanced field effect mobility and qualifies themselves as promising candidates for the applications in AMFPDs. Table 9.5 indicates that our latest resultst (the gain value of 62) are

improved comparing to similar studies from other groups [101,102].

Table 9-5 Summary & comparison for ambipolar TFTs and inverters

Inverter Comparison	APL 2008 Vol. 93, 033306 NCKU	APL 2008 Vol. 93, 213505 U. of Tokyo	2008 Submitted to SID09 NCTU
TFT type	Ambipolar	P-type + N-type	Ambipolar
Inverter	CMOS-like	CMOS	CMOS-like
P- type TFT	pentacene	pentacene	pentacene
N-type TFT	In ₂ O ₃	a-IGZO	a-IGZO
Gain (dV_{out}/dV_{in})	9	56	62
Operation quadrant	1+3	1	1+3
Process	Easy	Complex	Easy

9.2 Future Work

9.2.1 Pentacene based OTFTs

We proposed several methods to resolve some key issues of OTFTs such as high operating voltage and photosensitivity. Furthermore, we also demonstrated the functionality of OTFTs such as color-filtering. However, there are still some “trade-off” such as smaller on/off ratio and larger gate charge after introducing high κ insulators. As our future work, we shall find more suitable materials and fine tune the processes to get the balance behavior between on/off ratio and operation voltage. Furthermore, we have presented the possibilities of multi-functional dielectric materials for TFT applications. Based on our previous work, we would like to develop unique dielectric materials which should have several functions, such as high dielectric constant, coloring, wide-gamut, less-photosensitivity, and even polarization. Ink jet printing will be utilized to process these materials into TFT devices.

9.2.1 a-IGZO TFTs

a-IGZO TFTs in this dissertation were fabricated at University of Michigan, Ann Arbor during my extended internship. We are building up the processes at NCTU by using Self-aligned N⁺ region contact of a-IGZO TFTs as a platform to improve a-IGZO TFT performance. As widely known, higher oxygen vacancy makes a-IGZO film more conducting. We control the oxygen partial pressure during the sputtering of a-IGZO films. High oxygen partial pressure is processed first then low oxygen partial pressure is used to make an oxygen-vacancy-rich thin a-IGZO films. Following, source/drain metal is deposited then using wet dipping to etch non-use oxygen-vacancy-rich a-IGZO film. This oxygen-vacancy-rich region supposes to act as N⁺ electron rich area to form a good ohmic contact region. Finally, all TFTs will be made onto glass substrate to be transparent devices. The cross-sectional view and process flow are shown in Fig. 9-2.

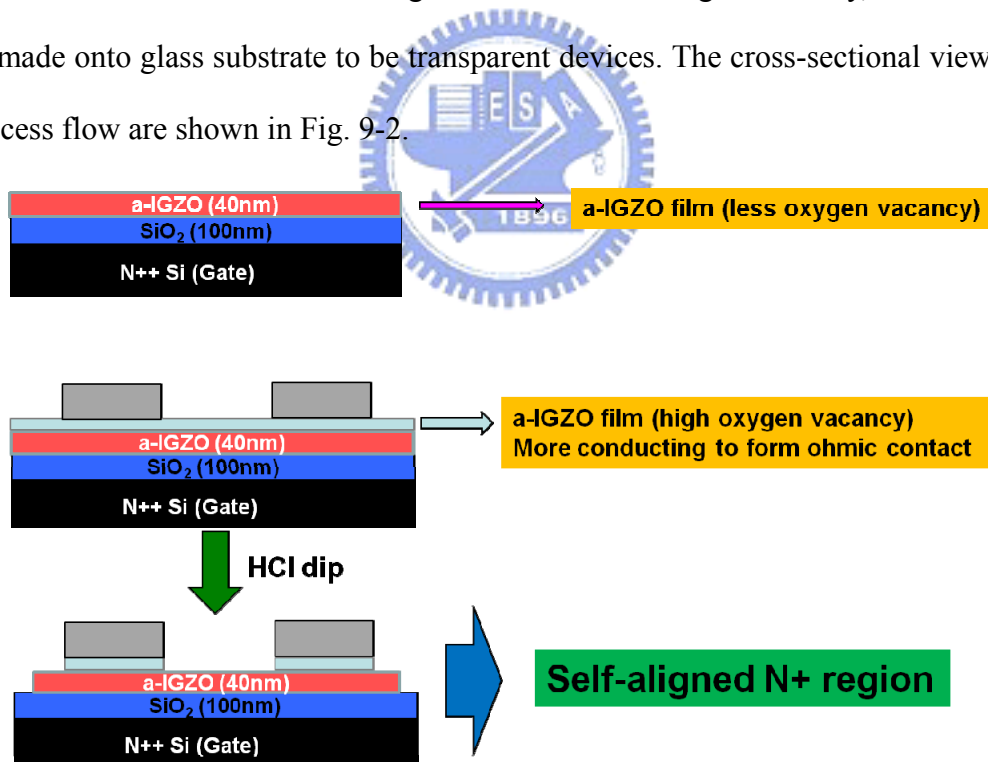


Fig. 9-2 Proposed self-aligned N⁺ region at contact area

Recently, gate driver on array technology is a hot topic for the cost reduction in TFT-LCDs. However, traditional a-Si:H TFTs still have some issues such as

instability and lower mobility. Based on our previous results, we will further study temperature coefficient and width/length effects by modelling the a-IGZO TFTs. The models will then be generated for a-IGZO based devices for gate driver circuits.

In addition, CMOS-like inverter circuits have been demonstrated by using air-stable channel materials pentacene and a-IGZO. Operating voltage, output frequencies, and gain values will be further studied and optimized. These ambipolar TFTs open a potential way to fabricate high performance logic devices with mechanical flexibility and good reliability in air condition.



References

- 1 J. P. Krusius, D. P. Seraphim, R. G. Greene, D. S. Skinner, and B. Yost, *Proc. of the IEEE*, **90**, no. 4, pp. 559-580, (2002).
- 2 J. K. Mohan, *SID Symposium Digest Tech Papers* 32, pp. 59-63 (2001).
- 3 Heeger A.J., *Synthetic Metals*, **125**, pp. 23-42 (2002).
- 4 MacDiarmid A.G., *Synthetic Metals*, **125**, pp. 11-22 (2002).
- 5 Dimitrakopoulos C.D. and Malenfant Patrick R.L., *Adv. Maert*, **14**, No. 2, pp. 99-117 16 (2002).
- 6 S. M. Cho, S. H. Han, J. H. Kim, and J. Jang, *Appl. Phys. Lett.* **88**, 071106 (2006)
- 7 M. J. Deen and M. H. Kazemeini, *Proc. IEEE* **93**, 1312 (2005).
- 8 Y. Y. Noh, D. Y. Kim, Y. Yoshida, K. Yase, B. J. Jung, E. H. Lim, and H. K. Shim, *Appl. Phys. Lett.* **86**, 043501(2005).
- 9 S. Ogawa, T. Naijo, Y. Kimura, H. Ishii, and M. Niwano, *Appl. Phys. Lett.* **86**, 252104 (2005).
- 10 I. Yagi, N. Hirai, M. Noda, A. Imaoka, Y. Miyamoto, N. Yoneya, K. Nomoto, J. Kasahara, A. Yumoto, and T. Urabe, *SID Symposium Digest Tech Papers* **38**, pp. 1753-1756 (2007)
- 11 N. F. Mott, E. A. Davis, *Electronic Processes in Non-Crystalline Materials*, Clarendon, 1979.
- 12 H. Hosono, *J. Non-Crystalline Solids* **352**, 851 (2006)
- 13 J. K. Jeong, J. H. Jeong, J. H. Choi, J. S. Im, S. H. Kim, H. W. Yang, K. N. Kang, K. S. Kim, T. K. Ahn, H.-J. Chung, M. Kim, B. S. Gu, J.-S. Park, Y.-G. Mo, H. D. Kim, and H. K. Chung, *SID Symposium Digest Tech Papers* **39**, pp. 1-4 (2008)

-
- 14 J. Zaumseil and H. Sirringhaus, *Chem. Rev.* **107**, 1296 (2007).
- 15 D. A. Neamen, *Electronic Circuit Analysis and Design*, 2nd ed. (McGraw-Hill, 2001).
- 16 T. Young, *Philos. Trans. R. Soc. London* **95**, 65 (1805).
- 17 Y.Y. Lin, D.J. Gundlach, S.F. Nelson, T.N. Jackson, *IEEE Trans. Electr. Dev.* **44** 1325 (1997).
- 18 H.E. Katz, Z. Bao, *J. Phys. Chem. B* **104** 671 (2000).
- 19 M. Shtein, J. Mapei, J.B. Benziger, S.R. Forrest, *Appl. Phys. Lett.* **81** 268 (2002).
- 20 P. Mach, S.J. Rodriguez, R. Nortrup, P. Wiltzius, J.A. Rogers, *Appl. Phys. Lett.* **78** 3592 (2001).
- 21 C.D. Sheraw, L. Zhou, J.R. Haug, D.J. Gundlach, T.N. Jackson, M.G. Kane, I.G. Hill, M.S. Hammond, J. Campi, B.K. Greening, J. Francl, J. West, *Appl. Phys. Lett.* **80** 1088 (2002).
- 22 T.W. Kelley, P.F. Baude, C. Gerlach, D.E. Ender, D. Muires, M.A. Haase, D.E. Vogel, S.D. Theiss, *Chem. Mater.* **16** 4413 (2004).
- 23 A. Facchetti, M.H. Yoon, T.J. Marks, *Adv. Mater.* **17** 1705 (2005).
- 24 H. Sirringhaus, *Adv. Mater.* **17** 2411 (2005).
- 25 C.D. Dimitrakopoulos, S. Purushothaman, J. Kymissis, A. Callegari, J.M. Shaw, *Science* **283** 822 (1999).
- 26 G. Velu, C. Legrand, O. Tharaud, A. Chapoton, D. Remiens, G. Horowitz, *Appl. Phys. Lett.* **79** 659 (2001).
- 27 F.C. Chen, C.W. Chu, J. He, Y. Yang, J.L. Lin, *Appl. Phys. Lett.* **85** 3295 (2004).
- 28 L.J. Berberich, M.E. Bell, *J. Appl. Phys.* **11** 681 (1940).
- 29 H. Klauk, M. Halik, U. Zschieschang, G. Schmid, W. Radlik, W. Weber, *J. Appl. Phys.* **92** 5259 (2002).
- 30 J. Veres, S. Ogier, G. Lloyd, *Chem. Mater.* **16** 4543 (2004).

-
- 31 N. E. Frost, P. B. McGrath, and C. W. Burns, *IEEE Int'l Symp. on Elect. Insulation, Montreal, Quebec, Canada*, (1996)
- 32 Y. Rao, J. Qu, and T. Marinis, *IEEE Trans. on Components and Packaging Tech.* **23**, No. 4, 680 (2000)
- 33 R.A.B. Devine, M.M. Ling, A.B. Mallik, M. Roberts, Z. Bao, *Appl. Phys. Lett.* **88** 151907 (2006).
- 34 M. Shtein, J. Mapel, J.B. Benziger, S.R. Forrest, *Appl. Phys. Lett.* **81** 268 (2002).
- 35 P. Mach, S.J. Rodriguez, R. Nortrup, P. Wiltzius, J.A. Rogers, *Appl. Phys. Lett.* **78** 3592 (2001).
- 36 A. Facchetti, M.H. Yoon, T.J. Marks, *Adv. Mater.* **17** 1705 (2005).
- 37 H. Siringhaus, *Adv. Mater.* **17** 2411 (2005).
- 38 A. Salleo, F. Endicott, R.A. Street, *Appl. Phys. Lett.* **86** 263505 (2005).
- 39 T. Jung, A. Dodabalapur, R. Wenz, Mohapatra, *Appl. Phys. Lett.* **87** 182109 (2005).
- 40 K.S. Narayan, N. Kumar, *Appl. Phys. Lett.* **79** 1891 (2001).
- 41 T.P. I Saragi, R. Pudzich, T. Fuhrmann, J. Salbeck, *Appl. Phys. Lett.* **84** 2334 (2004).
- 42 M.C. Hamilton, S. Martin, J. Kanicki, *IEEE Trans. Electr. Dev.* **51** 877 (2004).
- 43 S.M. Cho, S.H. Han, J.H. Kim, J. Jang, M.H. Oh, *Appl. Phys. Lett.* **88** 071106 (2006).
- 44 J. Lee, D.K. Hwang, J. -M. Choi, K. Lee, J.H. kim, S. Im, J.H. Park, E. Kim, *Appl. Phys. Lett.* **87** 023504 (2005).
- 45 T. Takenobu, T. Takahashi, T. Kanbara, K. Kanbara, K. Tsukagoshi, Y. Aoyagi, Y. Iwasa, *Appl. Phys. Lett.* **88** 033511 (2006).
- 46 F.C. Chen, C.S. Chuang, Y.S. Lin, L.J. Kung, T.S. Chen, H.P.D. Shieh, *Org.*

-
- Electr.* **7** 435 (2006).
- 47 S. Kobayashi, T. Nishikawa, T. Takenobu, S. Mori, T. Shimoda, T. Mitani, H. Shimotani, N. Yoshimoto, S. Ogawa, Y. Iwasa, *Nature Mater.* **3** 317 (2004).
- 48 K.P. Pernstich, S. Jaas, D. Oberhoff, C. Goldmann, D.J. Gundlach, B. Batlogg, A.N. Rashid, G. Schitter, *J. Appl. Phys.* **96** 6431 (2004).
- 49 E.J. Meijer, C. Tanase, P.W.M. Blom, E. Van Veenendaal, B. –H. Huisman, D.M. De Leeuw, T.M. Klapwijk, *Appl. Phys. Lett.* **80** 3838 (2002).
- 50 C.D. Dimitrakopoulos, P.R.L. Malenfant, *Adv. Mater.* **14** 99 (2002).
- 51 K. Nomura, H. Ohta, A. Takagi, T. Kamiya, M. Hirano, and H. Hosono, *Nature* **432** 488 (2004).
- 52 L. Wang, M. H. Yoon, G. Lu, Y. Yang, A. Facchetti, and T. J. Marks, *Nat. Mater.* **5** 893 (2006).
- 53 Q. Cao, Z. T. Zhu, M. G. Lemaitre, M. G. Xia, M. Shim, and J. A. Rogers: *Appl. Phys. Lett.* **88** 113511 (2006).
- 54 H. Ohta, T. Kambayashi, K. Nomura, M. Hirano, K. Ishikawa, H. Takezoe, and H. Hosono, *Adv. Mater.* **16** 312 (2004).
- 55 G. Horowitz, *J. Mater. Res.* **19** 1946 (2004).
- 56 D. K. Hwang, J. H. Park, J. Lee, J. M. Choi, J. H. Kim, E. Kim, and S. Im, *Electrochem. Solid-State Lett.* **8** G140 (2005).
- 57 C. S. Chuang, F. C. Chen, and H. P. D. Shieh, *Org. Electron.* **8** 767 (2007).
- 58 F. C. Chen, Y. S. Lin, T. H. Chen, and L. J. Kung, *Electrochem. Solid-State Lett.* **10** H186 (2007).
- 59 C. W. Chu, S. H. Li, and Y. Yang, *Appl. Phys. Lett.* **87** 193508 (2005).
- 60 C. S. Chuang, Y. S. Lin, L. J. Kung, D. S. Chen, F. C. Chen, and H. P. D. Shieh, *Proc. Int. Display Workshops*, pp.12-4 (2005).
- 61 M. Berggren, D. Nilsson, and N. D. Robinson, *Nat. Mater.* **6** 3 (2007).
- 62 *Organic Field-Effect Transistors*, edited by Z. Bao and J. Locklin Taylor and Francis, Boca Raton, (2007).
- 63 R. Rotzoll, S. Mohapatra, V. Olariu, R. Wenz, M. Grigas, K. Dimmler, O. Shchekin, and A. Dodabalapur, *Appl. Phys. Lett.* **88**, 123502 (2006).
- 64 L. Zhou, A. Wanga, S. C. Wu, J. Sun, S. Park, and T. N. Jackson, *Appl. Phys.*

-
- Lett.* **88**, 083502 (2006).
- 65 M. Shtein, J. Mapel, J. B. Benziger, and S. R. Forrest, *Appl. Phys. Lett.* **81**, 268 (2002).
- 66 P. Mach, S. J. Rodriguez, R. Nortrup, P. Wiltzius, and J. A. Rogers, *Appl. Phys. Lett.* **78**, 3592 (2001).
- 67 A. Facchetti, M. H. Yoon, and T. J. Marks, *Adv. Mater.* **17**, 1705 (2005).
- 68 D. Nilsson, N. Robinson, M. Berggren, and R. Forchheimer, *Adv. Mater.* **17**, 353 (2005).
- 69 W. Liu, K. Tang, Y. Guo, Y. Koike, and Y. Okamoto, *J. Fluorine Chem.* **123**, 147 (2003).
- 70 C. S. Chuang, S. T. Tsai, Y. S. Lin, F. C. Chen, and H. P. D. Shieh, *Jpn. J. Appl. Phys., Part 2* **46**, L1197 (2007).
- 71 S.-J. Wu, J.-A. Cheng, H.-M. P. Chen, Y.-R. Shin, H.-P. D. Shieh, P.-Y. Liu, Y.-C. Lo, H.-A. Li, W.-J. Hsieh, H.-C. Chiu, C.-H. Li, and K. Chou, *Proc. SID Symposium Digest Tech Papers* **39**, No. P66 (2008)
- 72 J. A. Cheng, C. P. Chang, C. H. Chen, and M. S. Lin, *J. Polym. Res.* **12**, 53 (2005).
- 73 H. Hosono, *J. Non-Cryst. Solids*, **198-200**, 165 (1996).
- 74 J. F. Wager, *Science*, **300**, 1245 (2003).
- 75 K. Nomura et al, "Amorphous oxide semiconductor: materials, carrier transport and TFT characteristics" *TAOS, Japan* (2006).
- 76 T. Li, J. Kanicki, W. Kong, and F. L. Terry, Jr., *J. Appl. Phys.*, **88**, 5764 (2000)
- 77 J. Kanicki, *Amorphous & Microcrystalline Semiconductor Devices, Volume II: Materials and Device Physics*, p.6, Boston: Artech House, (1992).
- 78 R.A. Street, *Hydrogenated Amorphous Silicon*, p.88, Cambridge: Cambridge University Press, (1991).
- 79 S. Sherman, S. Wagner, and R. A. Gottscho, *Appl. Phys. Lett.*, **69**, 3242 (1996)
- 80 M. Tani et al, "Progress in color filters for LCDs" *Proc. IDRC*, pp. 103–111 (1994).
- 81 J. Kanicki et al, "Optoelectronic properties of PLEDs on a plastic substrate" *J. SID*, **13/12**, 993-1002 (2005)
- 82 H. Yabuta, M. Sano, K. Abe, T. Aiba, T. Den, H. Kumomi, K. Nomura, T. Kamiya, and H. Hosono, *Appl. Phys. Lett.*, **89**, 112123-1 (2006).

-
- 83 T. Iwasaki, N. Itagaki, T. Den, H. Kumomi, K. Nomura, T. Kamiya, and H. Hosono, *Appl. Phys. Lett.*, **90**, 242114-1, (2007).
- 84 P. Jin-Seong, J. Jae Kyeong, M. Yeon-Gon, K. Hye Dong, and K. Sun, *Appl. Phys. Lett.*, **90**, 262106-1 (2007).
- 85 K. Nomura, A. Takagi, T. Kamiya, H. Ohta, M. Hirano, and H. Hosono, *Jpn. J. Appl. Phys., Part 1*, **45**, 4303 (2006).
- 86 A. Suresh, P. Wellenius, A. Dhawan, and J. Muth, *Appl. Phys. Lett.*, **90**, 123512-1 (2007).
- 87 M. Ofuji, K. Abe, H. Shimizu, N. Kaji, R. Hayashi, M. Sano, H. Kumomi, K. Nomura, T. Kamiya, and H. Hosono, *IEEE Electron Device Lett.*, **28**, 273-5 (2007).
- 88 J. Kanicki and S. Martin, "Hydrogenated Amorphous Silicon Thin-Film Transistors," in *Thin-Film Transistors*, C. R. Kagan and P. Andry, Eds. New York: Marcel Dekker, pp. 71-137 (2003).
- 89 R. Hayashi, M. Ofuji, N. Kaji, K. Takahashi, K. Abe, H. Yabuta, M. Sano, H. Kumomi, K. Nomura, T. Kamiya, M. Hirano, and H. Hosono, *J. of the SID*, **15**, 915 (2007).
- 90 A. Takagi, K. Nomura, H. Ohta, H. Yanagi, T. Kamiya, M. Hirano, and H. Hosono, *Thin Solid Films*, **486**, 38 (2005).
- 91 R. S. Muller, T. I. Kamins, and M. Chan, "Device Electronics for Integrated Circuits," 3rd ed New York: Wiley, pp.18 (2003).
- 92 C.-S. Chuang, T.-C. Fung, B. G. Mullins, K. Nomura, T. Kamiya, H.-P. D. Shieh, H. Hosono, and J. Kanicki, *SID Symposium Digest Tech Papers* **39**, pp. 1215 (2008).
- 93 A. Janotti and C. G. Van De Walle, *Appl. Phys. Lett.*, **87**, 122102 (2005).
- 94 T. Kamiya, H. Hiramatsu, K. Nomura, and H. Hosono, *J. of Electroceramics*, **17**, 267 (2006).
- 95 *ATLAS Device Simulation Software User's Manual*. Santa Clara, CA: Silvaco Inc., (2007).
- 96 S. J. Kang, Y. Yi, C. Y. Kim, K. Cho, J. H. Seo, M. Noh, K. Jeong, K.-H. Yoo, and C. N. Whang, *Appl. Phys. Lett.* **87**, 233502 (2005).
- 97 Shinuk Cho, Jonathan Yeun, Jin Young Kim, Kwanghee Lee, and Alan J. Heeger, *Appl. Phys. Lett.* **89**, 153505 (2006).

-
- 98 S. Hoshino, M. Yoshida, S. Uemura, T. Kodzasa, N. Takada, T. Kamata, and M. Muccini, *Appl. Phys. Lett.* **85**, 1613 (2004).
- 99 C. Rost, S. Karg, W. Riess, M. A. Loi, M. Murgia, and M. Muccini, *Appl. Phys. Lett.* **85**, 1613 (2004)
- 100 D. P. Gosain and T. Tanaka, *AMFPD 08 Digest*, 7-2 (2008).
- 101 Dhananjay, C. W. Ou, C. Y. Yang, M. C. Wu, and C. W. Chu, *Appl. Phys. Lett.* **93**, 033306 (2008).
- 102 J. H. Na, M. Kitamura, and Y. Arakawa, *Appl. Phys. Lett.* **93**, 213505 (2008).



Publication List

Journal Papers

1. **Chiao-Shun Chuang**, Jung-An Cheng, Yu-Jen Huang, Hsiao-Feng Chang, Fang-Chung Chen and Han-Ping D. Shieh, “Organic thin-film transistors with color filtering functional gate insulators” *Appl. Phys. Lett.*, **93**, 053305 (2008) (I.F.: 3.596)
2. **Chiao-Shun Chuang**, Fang-Chung Chen and Han-Ping D. Shieh, “Organic thin-film transistors with reduced – photosensitivity”, *Org. Electronics* **8**, 767 (2007). (I.F.: 3.879)
3. **Chiao-Shun Chuang**, Shu-Ting Tsai, Yung-Sheng Lin, Fang-Chung Chen and Han-Ping D. Shieh, “Photocurrent suppression of transparent organic thin film transistors”, *Jpn. J. Appl. Phys.*, **46** L1197 (2007) (I.F.: 1.247)
4. Fang-Chung Chen, **Chiao-Shun Chuang**, Yung-Sheng Lin, Li-Jen Kung, Dong-Sian Chen, and Han-Ping D. Shieh, “Low-voltage organic thin-film transistors with polymeric nanocomposite dielectrics”, *Org. Electronics* **7**, 435 (2006) (I.F.: 3.879)



International Conference Papers

a-IGZO TFTs

1. **Chiao-Shun Chuang**, Tze-Ching Fung, Barry G. Mullins, Kenji Nomura, Toshio Kamiya, Han-Ping D. Shieh, Hideo Hosono and Jerzy Kanicki, “Photosensitivity of Amorphous IGZO TFTs for Active-Matrix Flat-Panel Displays”, Society for Information Display 2008 (SID’08)
2. Tze-Ching Fung, **Chiao-Shun Chuang**, Charlene Chen, K Abe, H. Kumomi and Jerzy Kanicki, “2-D Numerical Simulation of High Performance Amorphous In-Ga-Zn-O TFTs”, AM-FPD 2008.
3. Tze-Ching Fung, **Chiao-Shun Chuang**, Barry G. Mullins, Kenji Nomura, Toshio Kamiya, Han-Ping D. Shieh, Hideo Hosono and Jerzy Kanicki, “Photofield-Effect in Amorphous InGaZnO TFTs”, IMID/IDMC 2008.

(Distinguished paper award)

Pentacene TFTs

4. **Chiao-Shun Chuang**, Han-Ping D. Shieh, Yang Yang, and Fang-Chung Chen “Numerical Prediction of Effective Dielectric Constant in Organic Thin-film Transistors with Nanocomposite Gate Insulator” International Display Manufacturing Conference & Exhibition, (IDMC) (2005).
5. **Chiao-Shun Chuang**, Yung-Sheng Lin, Li-Jen Kung, Dong-Sian Chen, Fang-Chung Chen, and Han-Ping D. Shieh “Organic Thin-Film Transistors based on Nanocomposite Gate Insulators for High-current Driving Applications” International Display Workshops (IDW) (2005).
6. **Chiao-Shun Chuang**, Shu-Ting Tsai, Fang-Chung Chen, and Han-Ping D. Shieh “Organic Thin-Film Transistors with reduced-photosensitivity” International Display Workshops (IDW) (2006).
7. **Chiao-Shun Chuang**, Shu-Ting Tsai, Yung-Sheng Lin, Fang-Chung Chen, and Han-Ping D. Shieh “Transparent OTFTs with Color-Filtering Functional Gate Insulators” Society for Information Display 2007 (SID’07)
8. Yu-Jen Huang, Hsiao-Fen Chang, Shu-Ting Tsai, **Chiao-Shun Chuang**, Jung-An Cheng, Fang-Chung Chen and Han-Ping D. Shieh “Color Filtering Functional Organic Thin-Film Transistors” International Display Manufacturing Conference & Exhibition, (IDMC) (2007)
9. Yan-Chu Tsai, Shu-Ting Tsai, **Chiao-Shun Chuang**, Jung-An Cheng, Fang-Chung Chen and Han-Ping D. Shieh “Organic Thin-Film Transistors with Novel Solution-Process Polymeric Gate Insulators” International Display Manufacturing Conference & Exhibition, (IDMC) (2007)

Domestic Conference Paper

1. Hsiao-Fen Chang, **Chiao-Shun Chuang**, and Fang-Chung Chen “Organic non-volatile memory devices with a polymer modification layer” 2008物理年會 (壁報論文獎優勝)

Patents

1. 薄膜電晶體、畫素結構及液晶顯示面板，莊喬舜、陳方中、謝漢萍（友達案號：AU0703009）(ROC Taiwan, USA Patent pending)
2. 有機半導體元件之接面結構及有機電晶體及其製造方法，陳方中、莊喬舜，中華民國專利第I260785號。

Vita

Name: Chiao-Shun (Patrick) Chuang 莊喬舜

Day of birth: September 8, 1974

Address: 高雄市苓雅區林南街10巷11號6F

E-mail: chiaoshun@ntu.edu.tw



● Education

- 2003/09 – 2009/01 **Ph.D., Institute of Electro-optical Engineering
National Chiao Tung University, Hsinchu,
Taiwan**
- 1997/09 – 1999/06 **Master, Department of Chemistry
National Taiwan University, Taipei, Taiwan**
- 1992/09 – 1997/06 **Bachelor, Department of Chemistry
National Taiwan University, Taipei, Taiwan**
- 2007/07 – 2008/01 **Visiting scholar, Dept. of EECS
University of Michigan, Ann Arbor, USA.**